



저작자표시-비영리-변경금지 2.0 대한민국

이용자는 아래의 조건을 따르는 경우에 한하여 자유롭게

- 이 저작물을 복제, 배포, 전송, 전시, 공연 및 방송할 수 있습니다.

다음과 같은 조건을 따라야 합니다:



저작자표시. 귀하는 원저작자를 표시하여야 합니다.



비영리. 귀하는 이 저작물을 영리 목적으로 이용할 수 없습니다.



변경금지. 귀하는 이 저작물을 개작, 변형 또는 가공할 수 없습니다.

- 귀하는, 이 저작물의 재이용이나 배포의 경우, 이 저작물에 적용된 이용허락조건을 명확하게 나타내어야 합니다.
- 저작권자로부터 별도의 허가를 받으면 이러한 조건들은 적용되지 않습니다.

저작권법에 따른 이용자의 권리는 위의 내용에 의하여 영향을 받지 않습니다.

이것은 [이용허락규약\(Legal Code\)](#)을 이해하기 쉽게 요약한 것입니다.

[Disclaimer](#)

공학박사 학위논문

**Synthesis of Two-dimensional  
Carbon-based Nanocomposites  
and Their Applications in  
Rechargeable Batteries**

2차원 탄소기반 나노복합체의 합성 및  
이차전지에의 응용

2016년 8월

서울대학교 융합과학기술대학원

융합과학부 나노융합전공

박 승 근



## **Abstract**

# **Synthesis of Two-dimensional Carbon-based Nanocomposites and Their Applications in Rechargeable Batteries**

Seung-Keun Park

Program in Nano Science and Technology

Graduate School of Convergence Science & Technology

Seoul National University

Over the past decade, graphene, the thinnest and most representative two-dimensional (2D) carbon material, has aroused high research interest because of its remarkable optical, electronic and mechanical properties. Meanwhile, as other representative 2D material, transition metal dichalcogenides derived from layered bulk crystals have also been intensively studied in recent years due to their unique properties and a

broad range of applications such as energy storage devices, catalysis, electronic, optoelectronics and so on. Especially, in energy storage system, these 2D nanomaterials have been considered promising building blocks for construction of advanced electrodes with high energy density and stability.

Nanocomposite material is a class of materials that are consisted of two or several components with at least one of them having a dimension in the nanoscale. The nanocomposite material possesses the advantages of its individual components, and at the same time may show new functions and properties for practical application, especially energy storage devices. Hybridizing nanomaterials with carbon is regarded as an effective way for enhancing the electrochemical performances due to the high conductivity, mechanical stability and surface area. However, currently, complicated and harsh synthetic processes are required to synthesize carbon-based nanocomposite, such as hydrothermal, solvothermal, and chemical vapor deposition (CVD) techniques; these are the main obstacles to mass producing these materials because these methods require expensive facilities, are time consuming, and are limited to small-sized reaction vessels. Especially, synthesizing 2D carbon-based nanocomposites remains challenging.

In my dissertation, I aim to describe 2D carbon-based nanocomposites, particularly centering on their preparation strategies and applications in rechargeable batteries (*i. e.* Li and Na ion batteries and lithium-sulfur batteries). Firstly, solventless and scalable strategy is developed for the synthesis of few-layer MoS<sub>2</sub> incorporated into hierarchical porous carbon (MHPC) nanosheet composites as anode materials for both Li- and Na-ion battery. An inexpensive oleylamine is introduced to not only serve as a surfactant and hinder the stacking of MoS<sub>2</sub> nanosheets but also to provide a conductive carbon, allowing large scale production. In addition, a SiO<sub>2</sub> template is adopted to direct the growth of both carbon and MoS<sub>2</sub> nanosheets, resulting in the formation of hierarchical porous structures with interconnected networks. Due to these unique features, the as-obtained MHPC shows substantial reversible capacity and very long cycling performance when used as an anode material for LIBs and SIBs, even at high current density. Indeed, this material delivers reversible capacities of 732 and 280 mA h g<sup>-1</sup> after 300 cycles at 1 A g<sup>-1</sup> in LIBs and SIBs, respectively. In addition, its Coulombic efficiency reached ~98 % after the 3<sup>rd</sup> cycle and exceeded 99 % after 100 cycles, indicating that efficient Li<sup>+</sup> insertion and extraction occur in the MHPC composites. The results suggest that these MHPC composites also have

tremendous potential for applications in other fields.

Secondly, monodisperse carbon nanocapsule ensemble-on-graphene nanosheet composites (MCNC/G) were prepared by a facile strategy, which involves mixing of iron-oleate and graphene, heat treatment, and finally, acid etching of iron oxide nanoparticles. The composites comprised highly uniform, hollow structured carbon nanocapsules with a diameter of about 20 nm that were densely deposited on the surface of the graphene nanosheets (the specific surface area =  $172.4 \text{ m}^2 \text{ g}^{-1}$  and pore volume =  $0.96 \text{ cm}^3 \text{ g}^{-1}$ ). In lithium-sulfur (Li-S) battery test, the MCNC/G-sulfur (MCNC/G-S) composite delivered a high specific capacity of  $524.7 \text{ mA h g}^{-1}$  after 100 cycles at 0.5 C-rate. In contrast, the capacity of graphene-sulfur (G-S) dropped significantly under the same conditions, even though the initial specific capacity ( $1337 \text{ mA h g}^{-1}$ ) was higher than that of MCNC/G-S ( $1262 \text{ mA h g}^{-1}$ ).

Finally, we report the successfully synthesis of honeycomb-like 2D mesoporous carbon nanosheet (OMCNS) by an etching of self-assembled iron oxide/carbon hybrid nanosheets as an advanced sulfur host for Li-S batteries. The obtained 2D nanosheets have close-packed uniform cubic mesopores of  $\sim 20 \text{ nm}$  side length, resembling honeycomb structure (the specific surface area =  $386.7 \text{ m}^2 \text{ g}^{-1}$  and pore volume = 1.05

cm<sup>3</sup> g<sup>-1</sup>). We loaded OMCNS with sulfur element simple melting infusion process (70 wt%) and evaluate the performance of the resulting OMCNS-sulfur composites as cathode material. the OMCNS-S electrode exhibits a reasonable cycling performance compared with G-S electrode, and it could maintain the specific capacity of 1237.7 mA h g<sup>-1</sup> at 1<sup>st</sup> cycle (0.1 C). After the galvanostatic rates were changed to 0.5 C, a specific capacity of 694.1 mA h g<sup>-1</sup> is obtained with the capacity retention of 548.6 mA h g<sup>-1</sup> at 0.5 C after 300 cycles. On the contrary, the G-S composite shows the fast capacity fading owing compared to OMCNS-S composite.

Such these 2D carbon-based nanocomposites enables the achievement of electrode materials with high capacity and long cyclability for high-performance rechargeable batteries. The results suggest that these nanocomposites also have tremendous potential for applications in other fields.

**Keywords: Two-dimensional materials, Carbon nanocomposites, Graphene, Transition metal dichalcogenides, Rechargeable batteries**

**Student Number: 2010-23944**

# Contents

## **Chapter 1. Introduction: Two-dimensional Nanomaterials for Rechargeable Batteries and Dissertation Overview**

1.1. Introduction.....	26
1.2. Classification of Two-dimensional Nanomaterials for Electrode in Rechargeable Batteries .....	31
1.2.1. Two-dimensional carbon nanomaterials.....	31
1.2.2. Two-dimensional inorganic nanomaterials.....	34
1.2.3. Two-dimensional nanocomposites .....	38
1.3. Preparation of Two-dimensional Nanomaterials for Electrode in Rechargeable Batteries .....	41
1.3.1. Mechanical exfoliation method .....	41
1.3.2. Chemical exfoliation method.....	41
1.3.3. Chemical vapor deposition .....	46
1.3.4. Wet chemical synthesis.....	48
1.3.4.1. Hydro/solvothermal synthesis .....	48
1.3.4.2. Soft colloidal templated synthesis .....	51

1.4. Applications of Two-dimensional Nanocomposites in Rechargeable Batteries .....	54
1.4.1. Lithium ion batteries.....	54
1.4.2. Sodium ion batteries.....	60
1.4.3. Lithium-sulfur batteries .....	65
1.5. Dissertation Overview .....	72
1.6. Reference .....	76

**Chapter 2. Synthesis of MoS<sub>2</sub>/Porous Carbon Nanosheet Nanocomposites for High-Performance Lithium and Sodium Ion Battery Anodes**

2.1. Introduction.....	87
2.2. Experimental Section.....	91
2.2.1. Chemicals .....	91
2.2.2. Characterization methods .....	91
2.2.3. Synthesis of few-layer MoS <sub>2</sub> /hierarchical porous carbon (MHPC) nanosheet hybrids.....	91
2.2.4. Electrochemical Characterization .....	92
2.3. Results and Discussion .....	98
2.4. Conclusion .....	133

2.5. References .....	135
-----------------------	-----

### **Chapter 3. Uniform Carbon Nanocapsule/Graphene Nanosheet Hybrids as Cathode Reservoirs for Lithium-Sulfur Batteries**

3.1. Introduction .....	141
3.2. Experimental Section .....	144
3.2.1. Chemicals .....	144
3.2.2. Characterization methods .....	144
3.2.3. Preparation of graphene .....	145
3.2.4. Preparation of carbon coated monodisperse iron oxide/graphene (IO@C/G) composite .....	145
3.2.5. Preparation of monodisperse carbon nanocapsule/G (MCNC/G) composite .....	146
3.2.6. Preparation of sulfur-loaded MCNC/G (MCNC/G-S) composite .....	146
3.2.7. Electrode preparation .....	146
3.2.8. Electrochemical characterization .....	147
3.3. Results and Discussion .....	151
3.4. Conclusion .....	168

3.5. References .....	169
-----------------------	-----

## **Chapter 4. Synthesis of Honeycomb-like Two-dimensional Mesoporous Carbon and Its Application in Lithium-Sulfur Batteries**

4.1. Introduction .....	174
4.2. Experimental Section .....	179
4.2.1. Chemicals .....	179
4.2.2. Characterization methods .....	179
4.2.3. Preparation of ordered mesoporous carbon nanosheets (OMCNS) .....	180
4.2.4. Preparation of OMCNS-S composites .....	180
4.2.5. Electrode preparation .....	180
4.2.6. Electrochemical characterization .....	181
4.3. Results and Discussion .....	185
4.4. Conclusion .....	206
4.5. References .....	207

<b>Chapter 5. Conclusion</b> .....	213
<b>Bibliography</b> .....	217
<b>국문 초록 (Abstract in Korean)</b> .....	230

## List of Figures

- Figure 1.1.** Classification of nanomaterials. (from Ref. 1. Feng *et al.*, *J. Mater. Chem.*, **2004**, 14, 469.) ..... 29
- Figure 1.2.** (a) surface and structural properties of 0D, 1D, 2D and 3D.  
(b) the features of 2D tree leaf in nature. (from Ref. 6. Liu *et al.*, *Adv. Mater.*, **2012**, 24, 4097.)..... 30
- Figure 1.3.** Various allotropes of graphitic carbon materials (graphene is the mother of all graphitic nanostructures). (from Ref. 10. Novoselov *et al.*, *Nat. Mater.*, **2007**, 6, 183.) ..... 33
- Figure 1.4.** Schematic illustration of different kinds of 2D nanomaterials.. (from Ref. 31. Zhang *et al.*, *ACS Nano*, **2015**, 9, 9451.).. 35
- Figure 1.5.** A schematic representation of a typical 2D TMDs (from Ref. 43. Ahluwalia *et al.*, *Eur. Phys. J. B*, **2012**, 85, 1.) ..... 36

**Figure 1.6.** (a) SEM image of Ag NPs deposited on GO. (b) TEM image of Au square sheets synthesized on GO. (c) TEM image of Pt/PdCu nanocubes on graphene sheets. (d) TEM image of  $\text{Co}_3\text{O}_4$  /graphene hybrid material. Inset: the corresponding SAED pattern. (e) TEM image of  $\text{TiO}_2/\text{MoS}_2$ /graphene hybrid. (f) TEM image of TiN/N-doped graphene hybrid (from Ref. 57. Zhang *et al.*, *Adv. Mater.* **2014**, 26, 2185)..... 40

**Figure 1.7.** (a) Optical micrograph of  $\text{MoS}_2$  films deposited on the  $\text{SiO}_2/\text{Si}$  substrate, (b) Atomic force microscopy (AFM) height image taken for the  $8 \times 8 \mu\text{m}^2$  area indicated by dotted lines in (a) and (c) Raman spectra of bulk and thin  $\text{MoS}_2$  films (from Ref. 65. Ryu *et al.*, *ACS Nano* **2010**, 4, 2695.) ..... 42

**Figure 1.8.** Schematic of fabrication processes of chemical exfoliated TMDs. (from Ref. 75. Loh *et al.*, *Nat. Commun.*, **2014**, 5, 2995.) ..... 45

<b>Figure 1.9.</b> Schematic of a common setup for chemical vapor deposition of graphene .....	47
<b>Figure 1.10.</b> (a) Schematic diagram of an autoclave for hydro/solvothermal reactions (b) Example of the bulk quantity of graphene product synthesized via solvothermal. (c) Schematic solvothermal synthesis of MoS <sub>2</sub> /G composites. (from Ref. 81, 82 Stride <i>et al.</i> , <i>Nat. Nanotechnol.</i> , <b>2009</b> , 4, 30, Dai <i>et al.</i> , <i>J. Am. Chem. Soc.</i> , <b>2011</b> , 133, 7296.) .....	50
<b>Figure 1.11.</b> 2D CuS nanosheets synthesized using soft colloidal templated synthesis. (from Ref. 85. Hyeon <i>et al.</i> , <i>Angew. Chem. Int. Ed.</i> , <b>2009</b> , 48, 6861.).....	52
<b>Figure 1.12.</b> Schematic illustration of the first LIBs (LiCoO <sub>2</sub> /Li <sup>+</sup> electrolyte/graphite) (from Ref. 93. Park <i>et al.</i> , <i>J. Am. Chem. Soc.</i> , <b>2013</b> , 135, 1167.) .....	56

**Figure 1.13.** Schematic illustration of active anode materials for the next generation of LIBs. Potential vs.  $\text{Li/Li}^+$  and the corresponding capacity density are shown. (from Ref. 87. Capiglia *et al.*, *J. Power Sources*, **2014**, 257, 421.)..... 58

**Figure 1.14.** Schematic illustration of SIBs (from Ref. 103. Komaba *et al.*, *J. Electrochem. Soc.*, **2015**, 162, A2538.) ..... 61

**Figure 1.15.** Theoretical gravimetric and volumetric energy densities of full cells with various reported anode materials for SIBs (from Ref. 104. Lee *et al.*, *Adv. Mater.*, **2014**, 26, 4139.). 64

**Figure 1.16.** Schematic diagram of a typical Li-S cell with its charge/discharge operations (from Ref. 107. Manthiram *et al.*, *Chem. Rev.*, **2014**, 114, 11751.)..... 66

**Figure 1.17.** Voltage profiles of a Li-S cell. (from Ref. 106. Tarascon *et al.*, *Nat. Mater.*, **2012**, 11, 19.)..... 70

<b>Figure 1.18.</b> (a) Illustration of the shuttle mechanism occurring in a Li-S cell, (b) Typical discharge plateaus of pristine sulfur cathodes with different resting times (from Ref. 107. Manthiram <i>et al.</i> , <i>Chem. Rev.</i> , <b>2014</b> , 114, 11751.) .....	71
<b>Figure 2.1.</b> Schematic Depicting the Synthesis Procedure of MHPC Composites .....	94
<b>Figure 2.2.</b> SEM and TEM images of MHPC composite before silica etching .....	95
<b>Figure 2.3.</b> SEM images of MoS <sub>2</sub> /C composites synthesized by using oleic acid as the precursors.....	96
<b>Figure 2.4.</b> Large scale synthesis of MHPC composites (using 1 ml of OA and 0.52 g of ATTU) .....	97
<b>Figure 2.5.</b> (a) XRD pattern, (b) TGA curve, (c, d) SEM images, and (e, f) TEM images of MHPC-0.1 composites.....	100

<b>Figure 2.6.</b> XRD pattern of MHPC-0.05, MHPC-0.2 and MoS <sub>2</sub> powder synthesized without OA .....	101
<b>Figure 2.7.</b> TGA curves of MHPC-0.05, MHPC-0.2, and MoS <sub>2</sub> /C composites .....	102
<b>Figure 2.8.</b> SEM images of (a, c) MHPC-0.05 and (b, d) MHPC-0.2 composites .....	103
<b>Figure 2.9.</b> SEM images of MoS <sub>2</sub> /C composites synthesized without SiO <sub>2</sub> template.....	106
<b>Figure 2.10.</b> TEM images of (a, c) MHPC-0.05 and (b, d) MHPC-0.2 composites.....	107
<b>Figure 2.11.</b> (a) A HR-TEM image, (b) SAED pattern, and (c) a TEM image and corresponding C, Mo, and S element mapping of MHPC-0.1. ....	108

**Figure 2.12.** (a, c) The N<sub>2</sub>-sorption isotherms of MHPC-0.05, 0.1, 0.2 and MoS<sub>2</sub>/C and (b, d) their pore size distribution curves..... 110

**Figure 2.13.** (a) XPS survey spectrum of MHPC-0.1 composite. High-resolution XPS spectra of (b) Mo 3d, (c) S 2p, and (d) C 1s of MHPC-0.1 composite..... 113

**Figure 2.14.** Electrochemical performance of MHPC-0.1 and MoS<sub>2</sub>/C used in LIBs. (a) CVs of MHPC-0.1 at a scanning rate of 0.2 mV s<sup>-1</sup>. (b) Galvanostatic discharge/charge profiles of MHPC-0.1 at 0.1 A g<sup>-1</sup>. (c) Cycling and (d) rate capability performance of MHPC-0.1, MoS<sub>2</sub>/C composites, and bare MoS<sub>2</sub> powder electrodes. (e) Long-term cycling performance at a current density of 1 A g<sup>-1</sup>. ..... 116

**Figure 2.15.** (a) Cyclic voltammograms of bare MoS<sub>2</sub> at a scanning rate of 0.2 mV s<sup>-1</sup>. (b) Galvanostatic discharge/charge profiles of bare MoS<sub>2</sub> at 0.1 A g<sup>-1</sup> ..... 117

<b>Figure 2.16.</b> (a) SEM, (b) TEM, (c, d) HR-TEM images and FFT pattern (inset) of the cycled MHPC-0.1 electrode in LIBs test.....	121
<b>Figure 2.17.</b> Electrochemical performance of MHPC-0.05, 0.1 and 0.2 for LIBs (a) Long-term cycling performance at a current density of 1 A g <sup>-1</sup> and (b) rate capability.....	125
<b>Figure 2.18.</b> Electrochemical impedance spectra of MHPC-0.1 and bare MoS <sub>2</sub> electrodes in LIBs (a) before cycling and (b) after 50 cycling .....	126
<b>Figure 2.19.</b> Electrochemical performance of MHPC-0.1 used in SIBs. (a) CVs at a scanning rate of 0.2 mV s <sup>-1</sup> . (b) Galvanostatic discharge/charge profiles at 0.1 A g <sup>-1</sup> . (c) Cycling and (d) rate capability performance of the electrodes. (e) Long-term cycling performance at a current density of 1 A g <sup>-1</sup> .....	128
<b>Figure 3.1.</b> Schematic illustration of preparation of the MCNC/G and MCNC/G-S composites.....	148
<b>Figure 3.2.</b> SEM images of (a, b) bare graphene nanosheets and (c, d) G-	

S composite .....	149
<b>Figure 3.3.</b> (a, b) SEM images and (c, d) TEM images of IO@C/G composites .....	150
<b>Figure 3.4.</b> Large scale synthesis of MCNC/G composites (using 0.14 g of graphene) .....	151
<b>Figure 3.5.</b> SEM images of (a) MCNC/G and (b) MCNC/G-S. TEM images of (c) MCNC/G and (d) MCNC/G-S. (e) Dark field image and the corresponding C and S element mapping of MCNC/G-S.....	153
<b>Figure 3.6.</b> (a) XRD patterns of IO@C/G, MCNC/G, and MCNC/G-S. (b) Raman spectra of MCNC/G and bare graphene; (c) Nitrogen adsorption-desorption isotherms, and (d) Pore-size distributions of MCNC/G and MCNC/G-S.....	156
<b>Figure 3.7.</b> Pictures in (a, b) show that powder of MCNC/G was not	

	attracted by a magnet after acid etching of IO@C/G .....	154
<b>Figure 3.8.</b>	TGA curves of MCNC/G-S and G-S .....	158
<b>Figure 3.9.</b>	(a, c) The N <sub>2</sub> -sorption isotherms and (b, d) the pore size distribution curves of bare graphene nanosheets and IO@C/G, respectively .....	159
<b>Figure 3.10.</b>	(a and b) Galvanostatic discharge/charge profiles of the MCNC/G-S and G-S composite at 0.1 C. (c and d) Cyclic voltammograms of the MCNC/G-S and G-S composite at a scanning rate of 0.1 mV s <sup>-1</sup> . (e) Cycling and (f) rate capability performance of the electrodes of the MCNC/G-S and G-S composite, respectively .....	163
<b>Figure 4.1.</b>	Schematic illustration of preparation of the OMCNS and OMCNS-S composites .....	182
<b>Figure 4.2.</b>	SEM images of IO-C NS .....	183
<b>Figure 4.3.</b>	Large scale synthesis of OMCNS .....	184

<b>Figure 4.4.</b> SEM images of (a, b) OMCNS (inset: a photo image of honeycomb) and (c, d) OMCNS-S composites .....	186
<b>Figure 4.5.</b> SEM images of (a, b) bare graphene nanosheets and (c, d) G-S composite (sulfur content: 70 wt%) .....	188
<b>Figure 4.6.</b> TEM images of (a, b) OMCNS and (c) OMCNS-S. (d, e) A dark field image and the corresponding S and C element mapping of OMCNS-S composite.....	189
<b>Figure 4.7.</b> (a) The XRD pattern of the IO-C NS, OMCNS and OMCNS-S. (b) A TGA curve of the OMCNS-S. and G-S.....	191
<b>Figure 4.8.</b> (a) Nitrogen adsorption-desorption isotherms of the OMCNS, OMCNS-S and IO-C NS composites (inset: pore-size distributions) and (b) Raman spectra of OMCNS and bare graphene.....	193
<b>Figure 4.9.</b> (a, c) Charge-discharge curves of OMCNS-S and G-S	

composites, obtained using a current density of 0.1C. (b, d) Cyclic voltammetry (CV) profiles of OMCNS-S and G-S composites obtained at a scanning rate of 0.05 mV s<sup>-1</sup>. . 196

**Figure 4.10** Galvanostatic charge-discharge curves of (a) OMCNS-S and (b) G-S electrodes at 10<sup>th</sup>, 50<sup>th</sup>, 100<sup>th</sup>, 200<sup>th</sup>, and 300<sup>th</sup> cycles at a current density of 0.5C (c) Cycle performance at current densities of 0.1C and 0.5C. (d) Charge-discharge curves in 300<sup>th</sup> cycle at a current density of 0.5C, and (e) Rate capability at various current densities (0.1C, 0.2C, 0.5C, 1C, and 2C) of OMCNS-S and G-S composites ..... 199

**Figure 4.11** Electrochemical impedance spectra of OMCNS-S and G-S electrodes (a) before cycling and (b) after 100 cycling. SEM images of (c) OMCNS-S and (d) G-S electrodes after 100 cycles at 0.5 C..... 203

## List of Tables

- Table 1.1.** Comparison of the typical synthetic methods for 2D nanomaterials..... 53
- Table 2.1.** Atomic and mass concentration of Mo, S and C of MHPC-0.1 from high resolution XPS peak integration ..... 114
- Table 2.2.** Comparison of the electrochemical performance of some related composite materials for LIBs in the literature .... 122
- Table 2.3.** Comparison of the electrochemical performance of some related composite materials for SIBs in the literature .... 129

# **Chapter 1. Introduction: Two-dimensional Nanomaterials for Rechargeable Batteries and Dissertation Overview**

## **1.1. Introduction**

The energy crisis in the 21<sup>st</sup> century has been for some time one of the most significant current issues faced by researchers. To alleviate or save energy problems, an increasing interest is energy storage devices with high-performance such as long-term stability, high energy and power densities. Among them, rechargeable batteries have attracted tremendous attention due to their high energy density, however, they have performance limitations in their capacity decay, relatively long charging-discharging time and consequently lower power densities.

Since early 1990s, nanomaterials with dimensions less than 100 nm have attracted great attention from scientists in various fields because of their excellent mechanical, chemical, biological, electronic, optical properties that are often considerably different from their corresponding bulk counterparts. These unique characteristics strongly depend on the

size, composition, atomic structure, interfaces and, defects [1].

These nanomaterials offer many advantages in energy storage applications. Energy storage is highly related to physical interaction and/or chemical reaction at the interface or surface, therefore the surface energy, specific surface area, and surface chemistry play a very critical role. The smaller size of nanomaterials may also provide more favorable charge transfer, mass, and heat, as well as alleviate dimensional changes attributed to chemical reactions and phase transitions [2].

Nanomaterials can be classified in zero-dimensional (0D) as nanospheres, one-dimensional (1D) as nanowires, two-dimensional (2D) as nanosheets or nanoplates, or three-dimensional (3D) as metallic colloids (**Figure 1.1**). Different structures exhibit their unique performances based on structural properties and surface respectively (**Figure 1.2a**). 0D structures have the minimum surface area and exhibit superior thermal stability. 1D structures offer the opportunity to fabricate micro-devices. 2D structures often possess specific facets and large exposed surfaces. Most of 3D structures have the performance of secondary structures.

Among them, 2D structured nanomaterials have been intensively investigated in various field such as optoelectronics, catalysis, energy

storage devices and so on [3-6]. Natural leaves as representative 2D structured materials have endured about billion years' evolution (**Figure 1.2b**). It is commonly acknowledged that the 2D shaped-leaves have more active sites than 0D and 1D nanomaterials. In addition, the leaf-like structure has some excellent properties including large surface area, shorten pathway, and small weight, which interestingly, accord with exactly to the needs for rechargeable batteries, suggesting that 2D structured nanomaterials are ideal electrode materials to achieve fast charging-discharging time, cycle stability and high energy density. Furthermore, these 2D nanomaterials have been considered promising building blocks for construction of advanced electrodes.

In this chapter, I would like to introduce classification and preparation of 2D nanomaterials for electrode in rechargeable batteries. In following section, applications of 2D nanomaterials in rechargeable batteries (*i.e.* lithium ion batteries, sodium ion batteries, and lithium-sulfur batteries) are described.

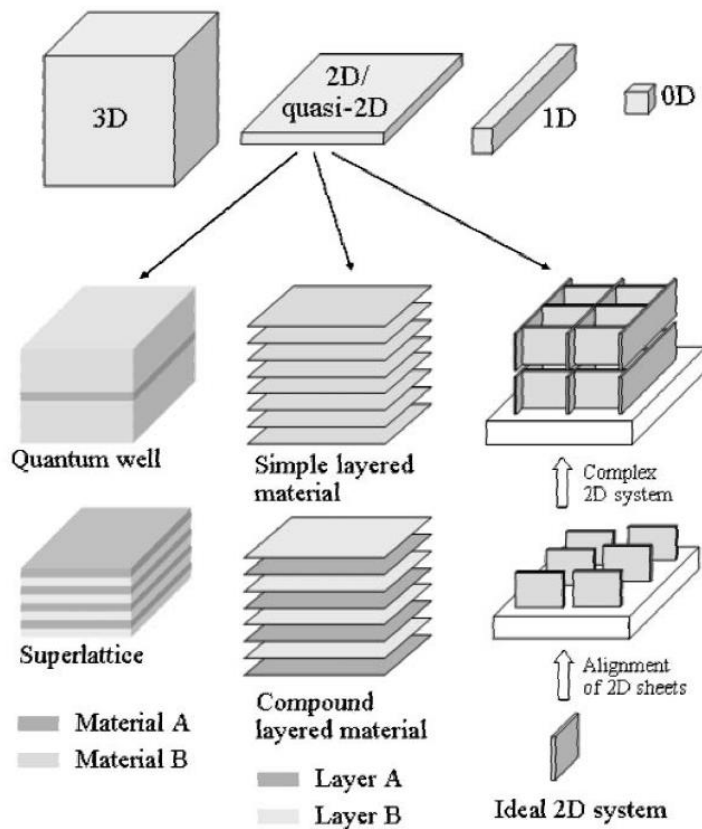


**Figure 1.1.** Classification of nanomaterials. (from Ref. 1. Feng *et al.*, *J. Mater. Chem.*, **2004**, 14, 469)

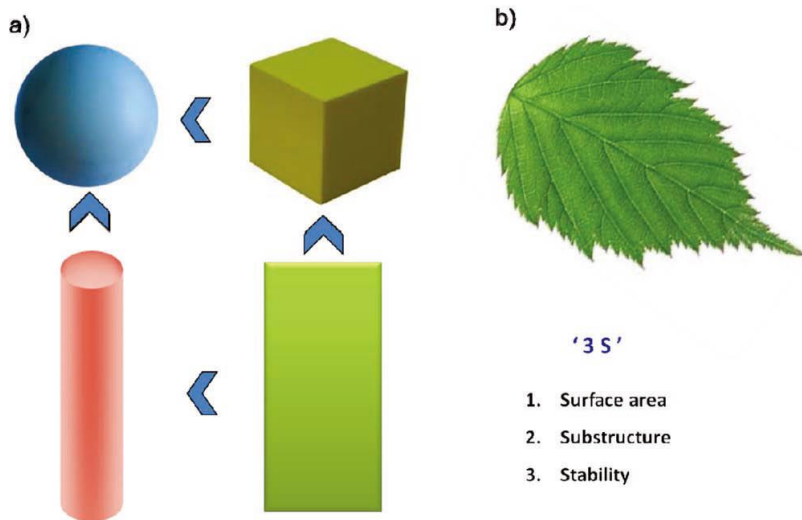


**Figure 1.2.** (a) surface and structural properties of 0D, 1D, 2D and 3D. (b) the features of 2D tree leaf in nature. (from Ref. 6. Liu *et al.*, *Adv. Mater.*, **2012**, 24, 4097.)

## **1.2. Classification of Two-dimensional Nanomaterials for Electrode in Rechargeable Batteries**

### **1.2.1. Two-dimensional carbon nanomaterials**

Graphene was originally defined as a 2D monolayer of  $sp^2$  bonded carbon, however, graphene-related materials consisting of chemical or structural derivatives of graphene are commonly called “graphene” by the research field. These materials include few-layer graphene and chemically reduced graphene oxide (G) [7-9].

Over the last decade, the graphene has aroused much research interest due to its exceptional specific surface area (theoretical value:  $2630 \text{ m}^2 \text{ g}^{-1}$ ), great electronic conductivity, mechanical stability and optical properties [10-13]. It is a basic component of other allotropes including carbon nanotubes, graphite, and fullerenes (**Figure 1.3**). These unique properties make it very promising electrode material for rechargeable batteries, supercapacitors, sensors, and nanoelectronic [14-19].

In current rechargeable battery technology, graphite or hard carbon is widely used as a commercial anode material due to its low cost and safety [20-23]. However, due to its tightly stacked structure, these materials exhibits a limited capacity and poor rate performance; graphite or hard

carbon therefore cannot meet the high energy and power density demands. In contrast, the graphene provides better electrochemical performance than the existing materials in rechargeable batteries, which show great promise for high performance electrode materials. However, problems to be overcome still remain. In particular, complete utilization of the potential of graphene is very difficult because graphene nanosheets tend to restack during application and preparation processes, leading to a rapid capacity loss [24, 25]. To solve this problem, the hybrid electrodes consisting of graphene and other materials have been proposed [26-28]. Especially, combining with metal-based materials as spacer have shown enhanced electrochemical performance [27, 29, 30].

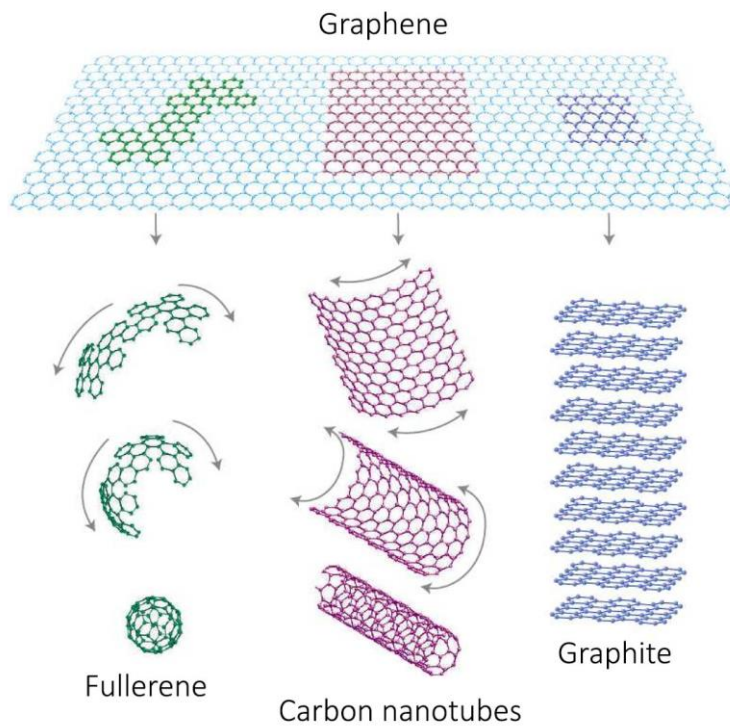


**Figure 1.3.** Various allotropes of graphitic carbon materials (graphene is the mother of all graphitic nanostructures). (from Ref. 10. Novoselov *et al.*, *Nat. Mater.*, **2007**, 6, 183.)

### 1.2.2. Two-dimensional inorganic nanomaterials

The unexpected physical, electronic and optical properties of graphene have inspired researchers to explore other 2D nanomaterials [31], as new building block for electrodes, that have similar layered structure characteristics but versatile properties, such as transition metal dichalcogenides (TMDs, e.g. MoS<sub>2</sub>, MoSe<sub>2</sub>, WS<sub>2</sub>, TiS<sub>2</sub>, etc) [32-35], hexagonal boron nitride (h-BN) [36, 37], graphitic carbon nitride (g-C<sub>3</sub>N<sub>4</sub>) [38], layered double hydroxides (LDHs) [39], and layered metal oxides [40] (**Figure 1.4**).

Among them, TMDs have received significant attention recently due to their superior magnetic [41], electronic [42] properties, and naturally abundant. TMDs consist of hexagonal layers of metal atoms (M = Mo, W, Nb, Re, V, Ta) sandwiched between two layers of chalcogen atoms (X = S, Se, Te) with an MX<sub>2</sub> stoichiometry as shown in **Figure 1.5** [43]. Graphene is normally chemically inert and can only be made active by functionalization with desired molecules, while TMDs show versatile physicochemical properties due to their unique structure and compositions, which are closely related to electrochemical performance [44, 45]. For these reasons, various TMDs have been intensively studied as electrode materials for rechargeable batteries [46-48].

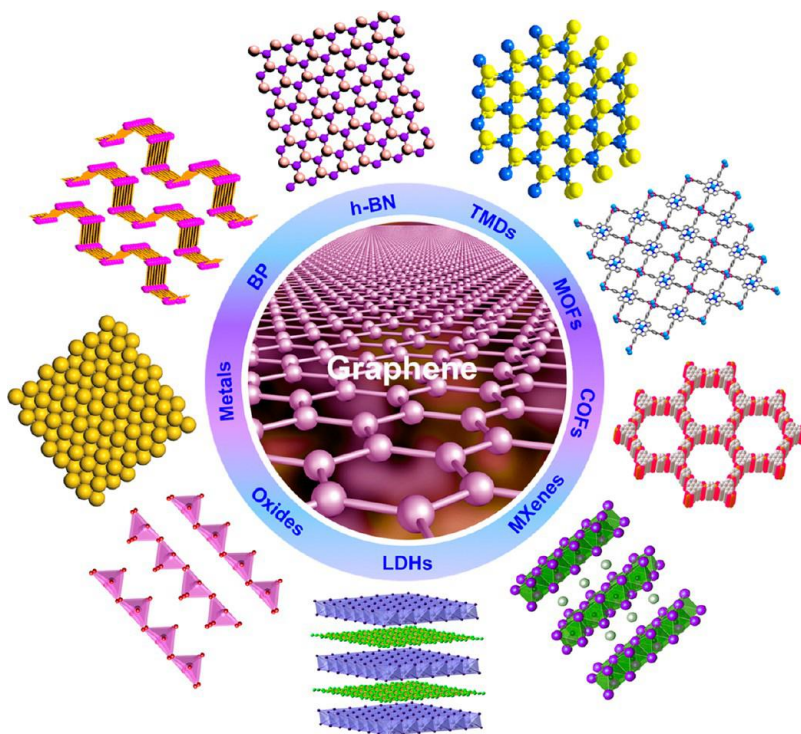


**Figure 1.4.** Schematic illustration of different kinds of 2D nanomaterials.

(from Ref. 31. Zhang *et al.*, *ACS Nano*, **2015**, 9, 9451.)

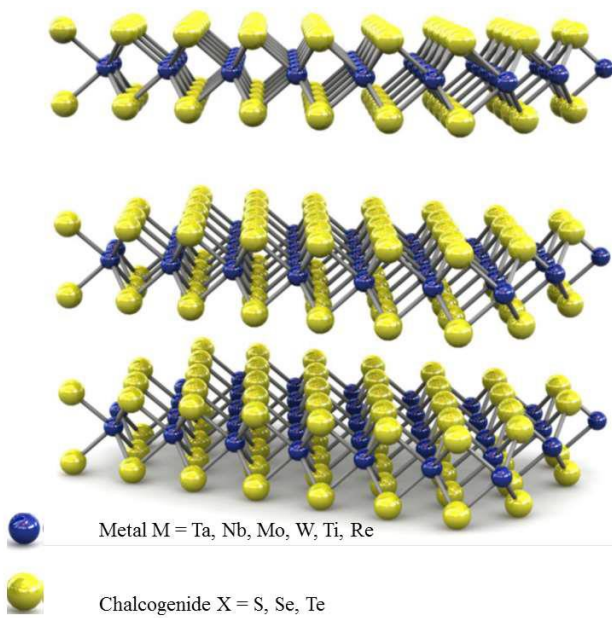


**Figure 1.5.** A schematic representation of a typical 2D TMDs. (from Ref. 43. Ahluwalia *et al.*, *Eur. Phys. J. B*, **2012**, 85, 1.)

Despite those predominant features, the practical application of TMDs as electrode materials are yet to be realized due to their low intrinsic electric conductivity and large volume changes during reactions, leading to dramatic electrode pulverization and electrical contact loss, thus resulting in poor cycle ability and rate performance [49, 50]. To overcome this problems, various strategies have been proposed to enhance the electrical conductivity and structural integrity of TMD-based electrode materials, such as coupling TMDs with electrically conductive carbon or polymer [51-53].

### 1.2.3. Two-dimensional hybrid materials

Hybrid material is a class of materials that are consisted of two or several components with at least one of them having a dimension in the nanoscale. A hybrid material possesses the advantages of its individual components, and at the same time may show new functions and properties for practical application, especially energy storage devices [26, 54-56].

Hybridizing nanomaterials with graphene is regarded as an effective way for enhancing the electrochemical performances due to the high conductivity, mechanical stability and surface area (**Figure 1.6**) [57, 58]. Indeed, graphene-based hybrid electrodes have already shown high capacity value, cycling stability, and excellent rate capability in rechargeable battery systems [59-61]. Inspired by the successful preparation of graphene-based hybrid materials, other 2D inorganic nanomaterials have also been considered promising building blocks for fabrication of advanced electrodes for realizing the improved properties. Generally, there are three types of hybrid electrodes based on 2D nanomaterials: i) controlled growth of other materials on 2D nanomaterials as synthetic templates [62], ii) assembly and/or growth of 2D nanomaterials on 1D and 3D templating structures to generate

hierarchically porous structures [63], iii) formation of heterostructures by stacking or assembly different kinds of 2D materials to artificially make van der Waals layered crystals [64].

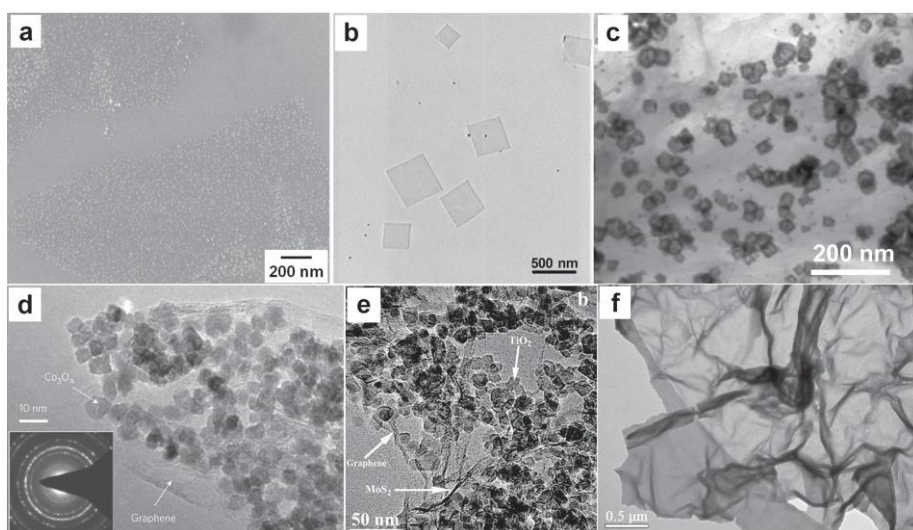


**Figure 1.6.** (a) SEM image of Ag NPs deposited on GO. (b) TEM image of Au square sheets synthesized on GO. (c) TEM image of Pt/PdCu nanocubes on graphene sheets. (d) TEM image of Co<sub>3</sub>O<sub>4</sub> /graphene hybrid material. Inset: the corresponding SAED pattern. (e) TEM image of TiO<sub>2</sub>/MoS<sub>2</sub>/graphene hybrid. (f) TEM image of TiN/N-doped graphene hybrid. (from Ref. 57. Zhang *et al.*, *Adv. Mater.* **2014**, 26, 2185.)

## **1.3. Preparation of Two-dimensional Nanomaterials for Electrode in Rechargeable Batteries**

### **1.3.1. Mechanical exfoliation method**

Mechanical exfoliation method was first used for the preparation of monolayer 2D nanosheets using the scotch tape technique. This method utilizes a piece of scotch tape to draw a thin film. After repeated peeling from bulk film, it is finally stamped onto a SiO<sub>2</sub>/Si substrate and then the tape is carefully removed (**Figure 1.7**) [65]. During the early phase of nanosheets preparation, significant amount of work has been done [66-68]. The obtained 2D nanomaterials exhibit single-and few layered structures with high quality, but the method is labour intensive and slow, thus it is utilized for only study of the fundamental properties of 2D nanomaterials rather than used in commercial applications.

### **1.3.2 Chemical exfoliation method**

Chemical exfoliation method is one of the commonly used approaches in research field, which is to exfoliate or intercalate the 2D nanomaterials by using suitable chemical reagents such as surfactants and strong acids.

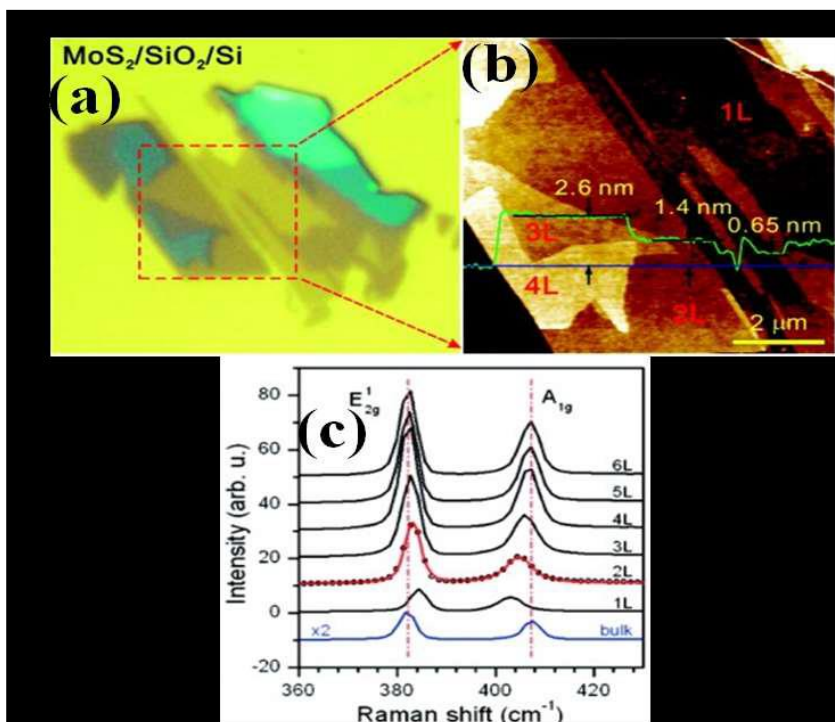


**Figure 1.7.** (a) Optical micrograph of MoS<sub>2</sub> films deposited on the SiO<sub>2</sub>/Si substrate, (b) Atomic force microscopy (AFM) height image taken for the 8x8 μm<sup>2</sup> area indicated by dotted lines in (a) and (c) Raman spectra of bulk and thin MoS<sub>2</sub> films. (from Ref. 65. Ryu *et al.*, *ACS Nano* **2010**, 4, 2695.)

In case of graphene, exfoliation of graphite by an oxidation technique followed by chemical reduction has been considered for low cost and large-scale production of graphene, called ‘Hummers methods’ [69, 70]. In this method, graphite oxide (GO) has been synthesized via strong oxidation of graphite using concentrated acids and strong oxidants. Due to the presence of oxygen containing groups, the GO has hydrophilic property which helps better dispersion in polar solvents than bare graphene. The GO can be converted to reduced GO (G) by chemical reduction, however, the obtained product often suffers from irreversible agglomeration or poor dispersion in water.

As for 2D inorganic nanomaterials, many groups have reported that the exfoliation process can be achieved by sonication of the bulk in various liquid phases such as *N*-methylpyrrolidone, dimethylformamide, or a mixture of ethanol and water [71, 72]. These liquid phases can not only exfoliate 2D nanomaterials but also stabilize the nanosheets to some given extent due to their effect on the surface energy. Especially, TMDs can be intercalated with lithium in organolithium compounds to give the reduced  $\text{Li}_x$ -TMDs phase with expanded lattice, this can be easily exfoliated in a next step into single-and few-layer nanosheets by ultrasonic-assisted process [73, 74]. However, long reaction time is

commonly required when *n*-butyl lithium is used as agent. To overcome this problem, Loh group has proposed the use of metal naphthalenide adducts for intercalation-exfoliation of TMDs and obtained high yield of micron-sized monolayer sheet (**Figure 1.8**) [75].

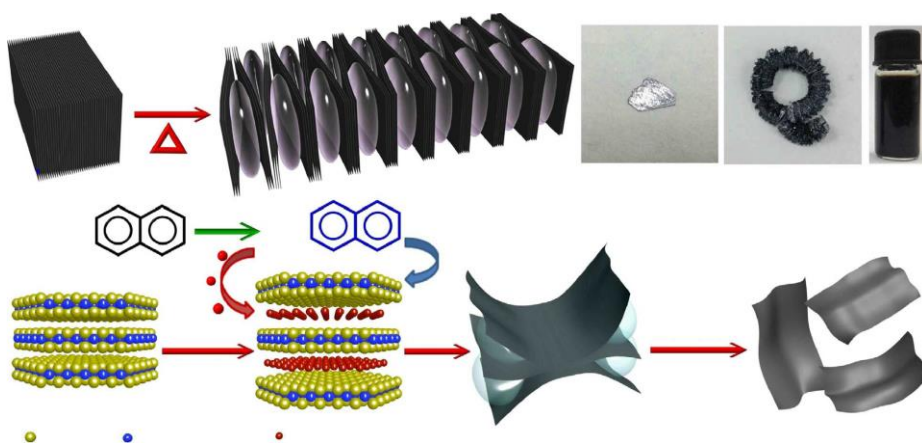


**Figure 1.8.** Schematic of fabrication processes of chemical exfoliated TMDs. (from Ref. 75. Loh *et al.*, *Nat. Commun.*, **2014**, 5, 2995.)

### 1.3.3. Chemical vapor deposition

Due to the violent nature of the chemical exfoliation, the original structure of 2D nanomaterials becomes deformed. Furthermore, the harsh process remains many defects and unnecessary functional groups on the 2D nanomaterials, which results in properties degradation such as low electrical conductivity and weak mechanical strength. However, large-area 2D nanomaterials with high quality mono or several-layer structures can be synthesized by using the chemical vapor deposition (CVD) method. Compared with the chemical exfoliation, the CVD method is more efficient in growing 2D nanomaterials films on specific substrate, with controllable thickness and high quality [76, 77]. Furthermore, the formation of the large-area 2D nanomaterial films by CVD is compatible with the current electronic fabrication processes, making this a promising candidate for building block. **Figure 1.9** demonstrates a schematic of an experimental setup CVD. It basically consists of a horizontal or vertical tube furnace for high temperature heating, a quartz vacuum chamber, a vacuum and pressure control system for the growth condition adjustment, and several mass flow controllers (MFC) to provide precursor and reactant gases with a necessary flow rate.

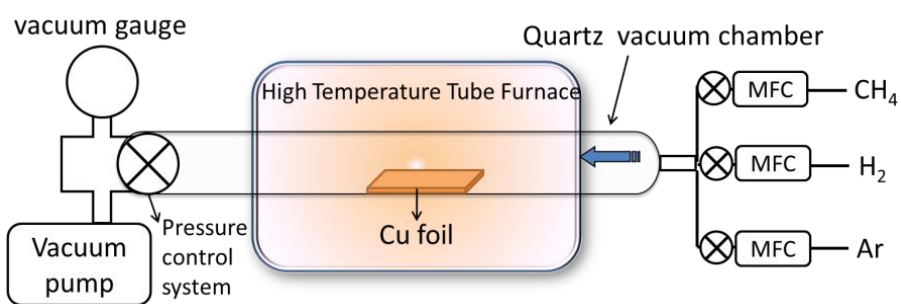


**Figure 1.9.** Schematic of a common setup for chemical vapor deposition of graphene.

### **1.3.4 Wet chemical synthesis**

Bottom-up wet chemical synthesis is the direct synthesis in the solution phase assisted with surfactants or polymers. It provides a potentially powerful alternative to exfoliation routes for synthesizing 2D nanomaterials, which can produce greater yield than other methods. Parameters that are well-known to control nanoparticle size, uniformity, and shape, including prudent choice of surface stabilizing ligands and reaction conditions, may also be applicable to 2D nanomaterials. To systemically design, an understanding of the properties of individual 2D nanomaterials is essential. In this section, we focus on three main wet-chemical synthesis methods including hydro/solvothermal synthesis and soft colloidal templated synthesis.

#### **1.3.4.1 Hydro/solvothermal synthesis**

Hydro/solvothermal synthesis is typical method that has been widely used for synthesis of 2D nanomaterials [78-80]. This method is carried out in a stainless steel autoclave to achieve high temperature and pressure, which facilitates producing nanomaterials with high quality and crystallinity (**Figure 1.10a**). As a typical example, Stride and co-workers demonstrated the gram-scale production of graphene via solvothermal

synthesis. In the method, the common laboratory reagents ethanol and sodium are reacted to give an intermediate solid that is then pyrolyzed to graphene sheets [81]. In addition, Dai group have developed a selective solvothermal synthesis of MoS<sub>2</sub> nanoparticles on G sheets using dimethylformamide as solvent. The selective growth of GO is attributed to the interactions between Mo precursors and functional groups on GO in a suitable condition [82].

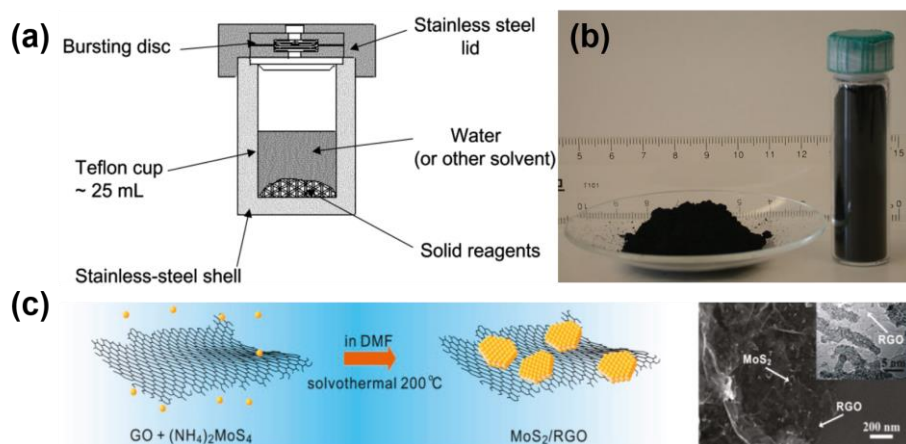


**Figure 1.10.** (a) Schematic diagram of an autoclave for hydro/solvothermal reactions (b) Example of the bulk quantity of graphene product synthesized via solvothermal. (c) Schematic solvothermal synthesis of MoS<sub>2</sub>/G composites. (from Ref. 81, 82 Stride *et al.*, *Nat. Nanotechnol.*, **2009**, 4, 30, Dai *et al.*, *J. Am. Chem. Soc.*, **2011**, 133, 7296.)

#### 1.3.4.2 Soft colloidal templated synthesis

Generally, soft colloidal templated synthesis represents a type of oil phase-based method to synthesize of 2D inorganic nanomaterials [83, 84], where the long-chain surfactant such as oleylamine and/or oleic acid are used as the soft colloidal templates for directing the crystal growth. The soft colloidal templated synthesis has been employed for synthesis of ultrathin 2D inorganic nanocrystals, especially for semiconductors [85, 86]. In 2009, Hyeon and co-workers used this method to synthesize ultrathin CdSe nanosheets. In the synthesis, the intermediate complexes consisted of 2D arrays of CdCl<sub>2</sub> and alkyl amine or/and oleic acid were obtained, in which the alkyl amine or/and oleic acid acted as the soft colloidal template (**Figure 1.11**) [85].

Despite their many advantages, the wet chemical synthesis of 2D nanomaterials is still in its infancy. The major synthetic challenges include i) careful control over metal oxidation states, ii) achieving high yield and purity, and iii) availability and selection of appropriate precursors. The comparison of above methods for synthesis of 2D nanomaterials is summarized in **Table 1.1**.

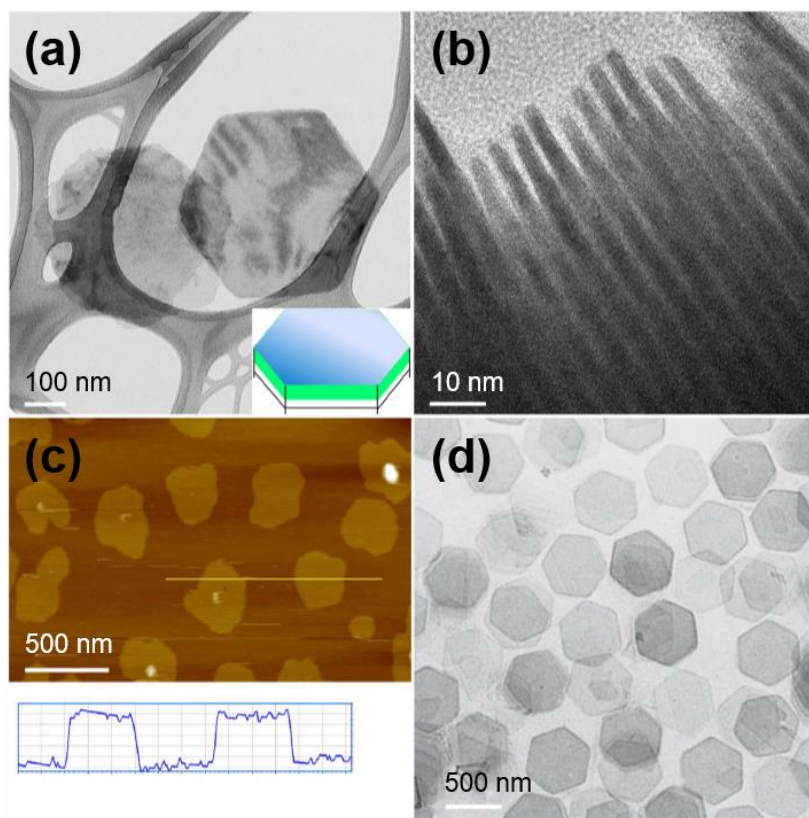


**Figure 1.11.** 2D CuS nanosheets synthesized using soft colloidal templated synthesis. (from Ref. 85. Hyeon *et al.*, *Angew. Chem. Int. Ed.*, **2009**, 48, 6861.)

**Table 1.1.** comparison of the typical synthetic methods for 2D nanomaterials.

Method	Brief description of the method	Advantage	Disadvantage
Mechanical exfoliation	Adhesive Scotch tape is used to peel layered bulk crystals. The peeled flakes are then deposit on a target substrate to get single- or few-layer sheets	High quality, large lateral size, few defects, simplicity	Low yield, non-massive production
Chemical exfoliation	Direct sonication of layered bulk crystals in solvents or in presence of surfactants or polymers	Solution processibility, massive production, low cost, simplicity	Low yield of single layers, uncontrollable layer number, relatively small lateral size
Chemical vapor deposition	One or more volatile precursors react and/or decompose on the exposed substrate surface to produce 2D crystals at high temperature and high vacuum	High quality, large lateral size, controllable thickness, few defects	High temperature, high vacuum, relatively complicated experiments, high cost
Wet chemical synthesis	Direct synthesis in the solution phase assisted with surfactants or polymers	Solution processibility, high yield, massive production	Surfactants required, hard to obtain uniform single-layer nanosheets

## **1.4. Applications of Two-dimensional Nanomaterials in Rechargeable Batteries**

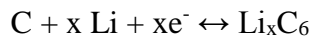
### **1.4.1. Lithium ion batteries**

Currently, the research community is engaging in much efforts to achieve effective energy storage strategies that are the key for exploring alternative energy and thus for the replacement of conventional fossil fuels and energy sources [87]. In this regard, Li-ion batteries (LIBs) play an important role due to their high volumetric and gravimetric energy, high power density, low self-discharge property and long cycle life [88, 89]. In addition, they have proved to be the most efficient energy storage systems for a wide range of portable devices [90, 91]. However, the application of LIBs in hybrid electric vehicles (HEV) and plug in hybrid electric vehicles (PHEV) demands from two to five times more energy density than the current LIB technology can offer ( $150 \text{ wh kg}^{-1}$ ) [92]. The increase of the energy density of LIBs can be achieved by developing high capacity anode and cathode electrode materials. In this sense, notable research is still under progress to enhance the performance of LIBs by using hybrid-based materials.

As shown in **Figure 1.12** [93], the present LIBs consist of the cathode

side (transition metals oxide or phosphates), anode side (graphite), polymer separator and electrolyte containing lithium salts in alkyl organic carbonates. The polymer separator prevents the direct electrical contact between cathode and anode and, at the same time, it allows the diffusion of  $\text{Li}^+$  from cathode to anode during the charging and the reverse discharging process. The detailed electrochemical reactions during the charge/discharge are the following:

Anode:



Cathode



Active materials should satisfy the requirements of good ionic and electrical conductivity, high reversible capacity, long cycle life, high rate of  $\text{Li}^+$  diffusion into active material, low cost and eco-compatibility. Graphite is definitely the most used anode owing to its low cost, good

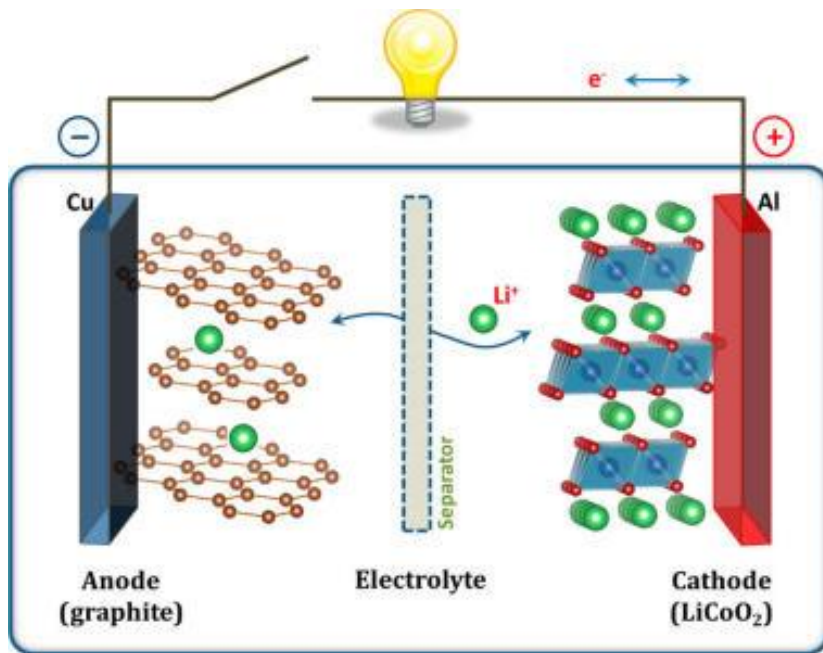


**Figure 1.12.** Schematic illustration of the first LIBs (LiCoO<sub>2</sub>/Li<sup>+</sup> electrolyte/graphite). (from Ref. 93. Park *et al.*, *J. Am. Chem. Soc.*, **2013**, 135, 1167.)

cycle life and low working potential vs.  $\text{Li}^+$ . However, graphite allows the intercalation of only one lithium ion with six carbon atoms, with a resulting stoichiometry of  $\text{LiC}_6$  and thus an equivalent reversible capacity of  $372 \text{ mA h g}^{-1}$ . Furthermore, it shows poor power density due to low diffusion rate into carbon materials ( $10^{-9}$  and  $10^{-7} \text{ cm}^2 \text{ s}^{-1}$ ) [94]. Therefore, the path leading to LIBs with improved energy and power density has, as major challenge, the selection of suitable anode materials that can provide high reversible capacity and easy diffusion of  $\text{Li}^+$  into the anode, along with good cycle life and free from safety concerns (**Figure 1.13**) [87].

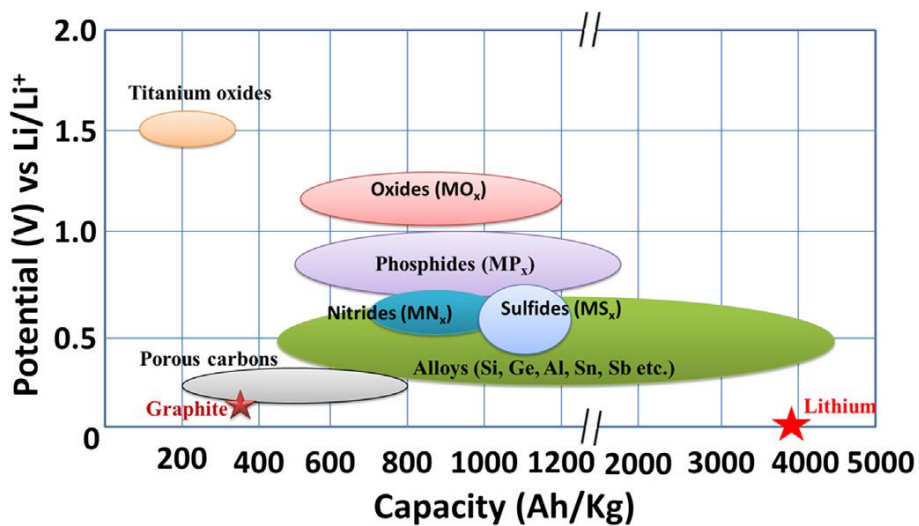


**Figure 1.13.** Schematic illustration of active anode materials for the next generation of LIBs. Potential vs. Li/Li<sup>+</sup> and the corresponding capacity density are shown. (from Ref. 87. Capiglia *et al.*, *J. Power Sources*, **2014**, 257, 421.)

Many attempts have been done in the investigation of a lot of materials for high performances and high capacity anode in LIBs. A short list must include: carbon nanotubes, carbon nanofibers, graphene, porous carbon, silicon and transition metal oxides [95-97]. Furthermore, TMDs, phosphides and nitrides might be also considered for anodes candidates [98, 99]. However, high volume expansion, poor electron transport, capacity fading, and low Coulombic efficiency as well, are the main obstacles that have to be overcome before they can be applied to practical devices. In this sense, promising results and a bright prospect is offered by nanostructuring the above listed materials. Nano-size and tailored morphology represent the key factor capable of leading these innovative materials from being theoretically relevant to a valuable technological breakthrough.

### 1.4.2. Sodium ion batteries

Owing to their excellent electrochemical performance, LIBs have been considered as a power source in HEV and mobile electronic devices such as lap-top computers and mobile phones. However, the current technology for LIBs is not expected to be able to satisfy the demands for power sources in future energy storage applications. Furthermore, lithium resources are relatively expensive and too geographically constrained [100]. Correspondingly, new rechargeable battery systems such as sodium ion, magnesium, metal-air and metal-sulfur batteries are being considered as promising alternatives to replace LIBs. Among them, sodium ion batteries (SIBs) have attracted much attention due to the low cost of sodium and better safety compared to sodium-metal batteries [101, 102]. Thanks to their low cost, the main potential application of SIBs is considered to be large-scale energy storage systems (ESS).

Battery system components and electric storage mechanisms of SIBs are basically similar as LIBs except ion carriers (**Figure 1.14**) [103]. SIB is composed of two electrodes of sodium insertion materials for positive and negative electrodes and they are electrically blocked by a separator, which are soaked with organic electrolyte containing a Na salt. As sodium is the second-lightest and –smallest metal next to lithium,

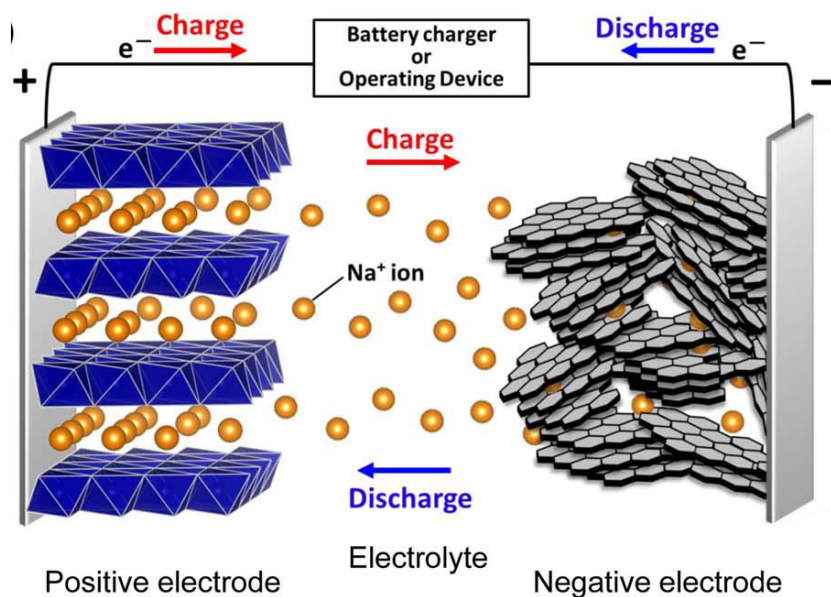


**Figure 1.14.** Schematic illustration of SIBs. (from Ref. 103. Komaba *et al.*, *J. Electrochem. Soc.*, **2015**, 162, A2538.)

the sacrifice in performance is expected to be minimized when electrochemical  $\text{Na}^+$  insertion/de-insertion is same as that of Li-system. Furthermore, a Cu current collector for an anode is able to be replaced with much cheaper aluminum because sodium metal does not react with Al, which is ultimately advantageous of SIBs.

Despite their many advantages, the atomic weight and standard potential of sodium are critical challenging issues to be considered. In addition, most electrode materials that have been introduced for SIBs show similar or somewhat lower redox potential and specific capacities than those for LIBs, resulting in lower energy density for the SIBs. Therefore, it is important to develop new electrode materials with high energy densities for SIBs to reduce the cost per energy unit.

The energy density can be improved by i) using electrode materials with high specific capacities, ii) using anode materials with low redox potentials, and iii) using cathode materials with high redox potentials. However, most cathode materials store sodium ions by intercalation, which indicates that the number of storage sites is limited, suggesting that it will be difficult to quite increase the specific capacity of the cathode materials. The use of cathode materials with high redox potentials is also limited due to electrolyte decomposition at high

potentials. Therefore, the feasible strategy is developing anode materials with appropriately low redox potential ranges and high specific capacities to improve the energy density of SIBs so that they can successfully replace Li-ion batteries. **Figure 1.15** shows the specific and volumetric energy densities of full cells with various reported anode materials [104]. This reveals that a similar energy density to those of commercialized Li-ion batteries (150–200 Wh kg<sup>-1</sup>, 400–650 Wh L<sup>-1</sup>) can be achieved by using only high-capacity anode materials such as alloy material, metal oxides, metal sulfides and phosphorus-based materials for SIBs.

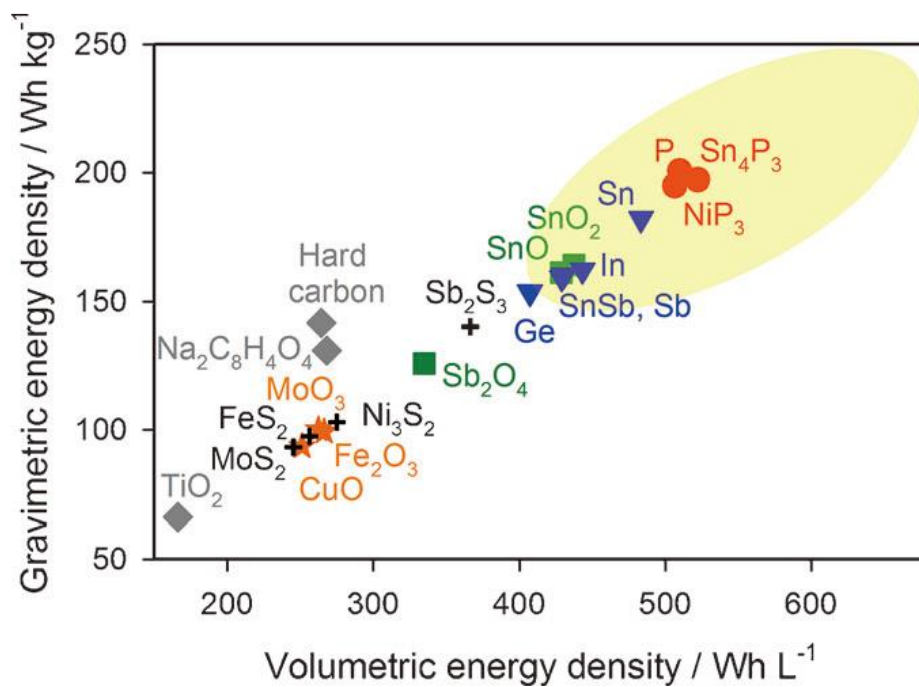


**Figure 1.15.** Theoretical gravimetric and volumetric energy densities of full cells with various reported anode materials for SIBs. (from Ref. 104. Lee *et al.*, *Adv. Mater.*, **2014**, 26, 4139.)

### 1.4.3. Lithium-sulfur batteries

As mentioned above section, the present LIBs can not satisfy the energy demands for commercialization of HEV and PHEV. Therefore, alternative electrode materials that provide higher capacities need to be developed. To overcome the limitations of compound electrodes with insertion mechanism, materials that undergo conversion reactions while accommodating more ions and electrons are becoming a promising candidate, but are highly challenging. In this sense, Li-O<sub>2</sub> and Li-S batteries with high energy are being intensively pursued [105, 106].

Sulfur, one of the most abundant elements, provides a high theoretical capacity of 1672 mA h g<sup>-1</sup>, which is an order of magnitude higher than those of the traditional cathode materials. The high capacity value is based on the conversion reaction of sulfur to form lithium sulfide (Li<sub>2</sub>S) by reversibly incorporating two electrons per sulfur atom compared to one or less than one electron per transition-metal ion in insertion-oxide cathodes.

A Li-S cell is an energy storage device through which electrical energy can be stored in sulfur electrode. A schematic of the typical Li-S cell system and its operation is depicted in **Figure 1.16** [107]. A conventional Li-S cell consists of a Li metal anode, a sulfur composite cathode, and

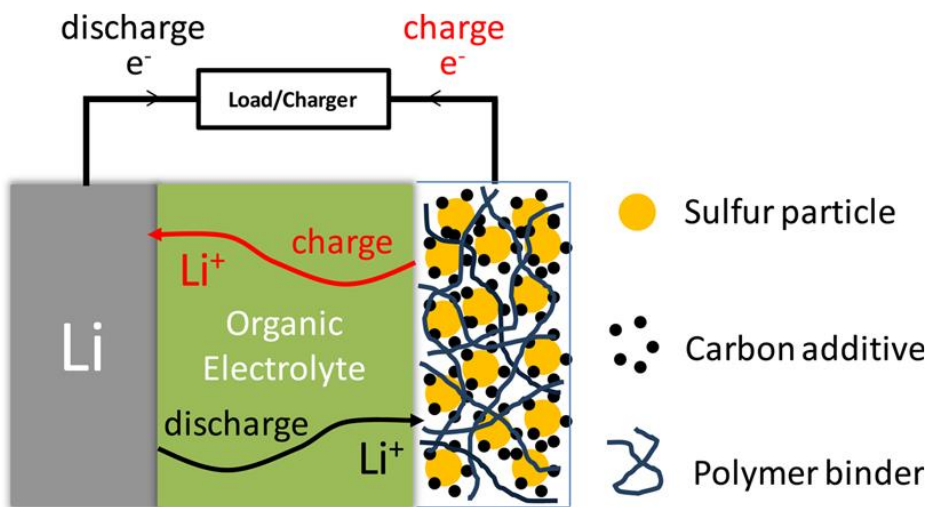


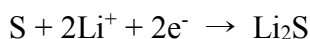
**Figure 1.16.** Schematic diagram of a typical Li-S cell with its charge/discharge operations. (from Ref. 107. Manthiram *et al.*, *Chem. Rev.*, **2014**, 114, 11751.)

an organic electrolyte. The reaction mechanism occurring during discharge are given below, and the backward reactions will occur during charge.

Negative electrode: anodic reaction (loss of electrons)



Positive electrode: cathodic reaction (gaining electrons)



Overall cell reaction (discharge)



Based on above reactions, the Li-S cell delivers a theoretical capacity of 1167 mA h g<sup>-1</sup>. The discharge reaction has a cell voltage of 2.15 V.

Sulfur atoms show a strong tendency to catenation, generating homocyclic rings or long homo-atomic chains of various sizes [106]. Cyclo-S<sub>8</sub>, crystallizing at 25 °C as orthorhombic α-S<sub>8</sub>, is the most stable sulfur allotrope at room temperature. During discharge process, cyclo-S<sub>8</sub> is reduced and the ring opens, resulting in the formation of high-order Li<sub>2</sub>S<sub>x</sub>

( $6 < x \leq 8$ ). As the discharge continues, lower order  $\text{Li}_2\text{S}_x$  ( $2 < x \leq 6$ ) are newly formed with the incorporation of additional lithium. In voltage profiles of a Li-S cell, there are two distinct discharge plateaus at 2.3 and 2.1 V with ether-based liquid electrolytes, which attributed to the conversions of  $\text{S}_8$  to  $\text{Li}_2\text{S}_4$  and  $\text{Li}_2\text{S}_4$  to  $\text{Li}_2\text{S}$ , respectively. As shown in **Figure 1.17**,  $\text{Li}_2\text{S}$  is formed at the end of discharge. During the following charge process, the  $\text{Li}_2\text{S}$  is converted to  $\text{S}_8$  via the formation of the intermediate lithium polysulfides, leading to a reversible cycle [108].

Despite its high theoretical capacity, there are critical challenges facing the Li-S technology. First, the high electrical resistance of sulfur ( $\sim 10^{-30}$  S  $\text{cm}^{-1}$ ) and lithium polysulfides formed during cycling along with their morphological and structural changes are tremendous challenges, resulting in unstable electrochemical contact within sulfur cathodes. Furthermore, the conversion of sulfur to lithium sulfide involves morphological and structural changes as well as deposition of reactive and species repetitive dissolution, which tend to passivate both the electrodes, leading to a severe increase in impedance. These issues lead to a low utilization of the active sulfur material, low system efficiency and poor cycle life. Unfortunately, Li-S batteries have also serious self-discharge behavior due to the dissolution of polysulfides even in the

resting state (**Figure 1. 18**) [107].

To overcome these problems, various strategies have been proposed. i) sulfur coating with conductive polymer, ii) sulfur-impregnation into porous carbon materials and iii) sulfur-metal oxide/chalcogenide composites. Especially, the sulfur/porous carbon composites have been intensively studied due to high conductivity, mechanical strength and confine effect of porous carbon materials [26, 109-111].

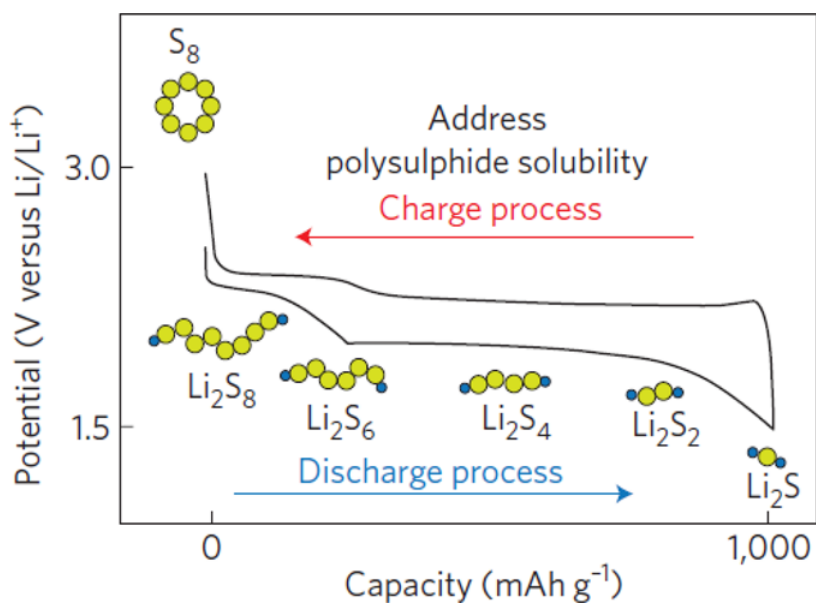


**Figure 1.17.** Voltage profiles of a Li-S cell. (from Ref. 106. Tarascon *et al.*, *Nat. Mater.*, **2012**, 11, 19.)

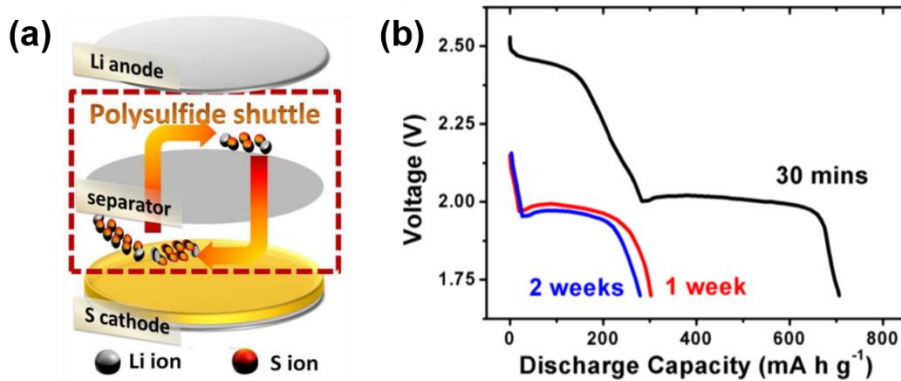


**Figure 1.18.** (a) Illustration of the shuttle mechanism occurring in a Li-S cell, (b) Typical discharge plateaus of pristine sulfur cathodes with different resting times. (from Ref. 107. Manthiram *et al.*, *Chem. Rev.*, **2014**, 114, 11751.)

## 1.5. Dissertation Overview

Two-dimensional (2D) carbon-based nanocomposites has aroused hugh research interest because of their remarkable optical, electronic and mechanical properties. Especially, in energy storage system, these 2D composites have been considered promising building blocks for construction of advanced electrodes with high energy density and stability.

In my dissertation, I aim to describe 2D carbon-based nanocomposites, particularly centering on their preparation strategies and applications in rechargeable batteries (*i. e.* Li and Na ion batteries and lithium-sulfur batteries). Firstly, solventless and scalable strategy is developed for the synthesis of few-layer MoS<sub>2</sub> incorporated into hierarchical porous carbon (MHPC) nanosheet composites as anode materials for both Li- and Na-ion battery. An inexpensive oleylamine is introduced to not only serve as a surfactant and hinder the stacking of MoS<sub>2</sub> nanosheets but also to provide a conductive carbon, allowing large scale production. In addition, a SiO<sub>2</sub> template is adopted to direct the growth of both carbon and MoS<sub>2</sub> nanosheets, resulting in the formation of hierarchical porous structures with interconnected networks. Due to these unique features, the as-obtained MHPC shows substantial reversible capacity and very

long cycling performance when used as an anode material for LIBs and SIBs, even at high current density. Indeed, this material delivers reversible capacities of 732 and 280 mA h g<sup>-1</sup> after 300 cycles at 1 A g<sup>-1</sup> in LIBs and SIBs, respectively. In addition, its Coulombic efficiency reached ~98 % after the 3<sup>rd</sup> cycle and exceeded 99 % after 100 cycles, indicating that efficient Li<sup>+</sup> insertion and extraction occur in the MHPC composites. The results suggest that these MHPC composites also have tremendous potential for applications in other fields.

Secondly, monodisperse carbon nanocapsule ensemble-on-graphene nanosheet composites (MCNC/G) were prepared by a facile strategy, which involves mixing of iron-oleate and graphene, heat treatment, and finally, acid etching of iron oxide nanoparticles. The composites comprised highly uniform, hollow structured carbon nanocapsules with a diameter of about 20 nm that were densely deposited on the surface of the graphene nanosheets (the specific surface area = 172.4 m<sup>2</sup> g<sup>-1</sup> and pore volume = 0.96 cm<sup>3</sup> g<sup>-1</sup>). In lithium-sulfur (Li-S) battery test, the MCNC/G-sulfur (MCNC/G-S) composite delivered a high specific capacity of 524.7 mA h g<sup>-1</sup> after 100 cycles at 0.5 C-rate. In contrast, the capacity of graphene-sulfur (G-S) dropped significantly under the same

conditions, even though the initial specific capacity ( $1337 \text{ mA h g}^{-1}$ ) was higher than that of MCNC/G-S ( $1262 \text{ mA h g}^{-1}$ ).

Finally, we report the successfully synthesis of honeycomb-like 2D mesoporous carbon nanosheet (OMCNS) by an etching of self-assembled iron oxide/carbon hybrid nanosheets as an advanced sulfur host for Li-S batteries. The obtained 2D nanosheets have close-packed uniform cubic mesopores of  $\sim 20 \text{ nm}$  side length, resembling honeycomb structure (the specific surface area =  $386.7 \text{ m}^2 \text{ g}^{-1}$  and pore volume =  $1.05 \text{ cm}^3 \text{ g}^{-1}$ ). We loaded OMCNS with sulfur element simple melting infusion process (70 wt%) and evaluate the performance of the resulting OMCNS-sulfur composites as cathode material. the OMCNS-S electrode exhibits a reasonable cycling performance compared with G-S electrode, and it could maintain the specific capacity of  $1237.7 \text{ mA h g}^{-1}$  at 1<sup>st</sup> cycle (0.1 C). After the galvanostatic rates were changed to 0.5 C, a specific capacity of  $694.1 \text{ mA h g}^{-1}$  is obtained with the capacity retention of  $652.6 \text{ mA h g}^{-1}$  at 0.5 C after 100 cycles. On the contrary, the G-S composite shows the fast capacity fading owing compared to OMCNS-S composite

Such these 2D carbon-based nanocomposites enables the achievement of electrode materials with high capacity and long cyclability for high-

performance rechargeable batteries. The results suggest that these nanocomposites also have tremendous potential for applications in other fields.

## 1.6. References

- [1] Y. H. Wu, B. J. Yang, B. Y. Zong, H. Sun, Z. X. Shen and Y. P. Feng, *J. Mater. Chem.*, **2004**, 14, 469.
- [2] Q. F. Zhang, E. Uchaker, S. L. Candelaria and G. Z. Cao, *Chem. Soc. Rev.*, **2013**, 42, 3127.
- [3] B. Cho, J. Yoon, S. K. Lim, A. R. Kim, S. Y. Choi, D. H. Kim, K. H. Lee, B. H. Lee, H. C. Ko and M. G. Hahm, *Sensors-Basel*, **2015**, 15, 24903.
- [4] S. Bai and Y. J. Xiong, *Sci. Adv. Mater.*, **2015**, 7, 2168.
- [5] X. T. Luo, W. Xin, C. H. Yang, D. Yao, Y. Liu, H. Zhang, K. Zhang and B. Yang, *Small*, **2015**, 11, 3583.
- [6] J. H. Liu and X. W. Liu, *Adv. Mater.*, **2012**, 24, 4097.
- [7] U. Yaqoob, A. S. M. I. Uddin and G. S. Chung, *Sensor. Actuat.. B-Chem.*, **2016**, 229, 355.
- [8] H. D. Liu, Y. L. Wang, L. Shi, R. P. Xu, L. H. Huang and S. Z. Tan, *Desalin. Water. Treat.*, **2016**, 57, 13263.
- [9] X. J. Men, H. B. Chen, K. W. Chang, X. F. Fang, C. F. Wu, W. P. Qin and S. Y. Yin, *Appl. Catal. B-Environ.*, **2016**, 187, 367.
- [10] A. K. Geim and K. S. Novoselov, *Nat. Mater.*, **2007**, 6, 183.
- [11] S. Bera, M. Pal, A. Naskar and S. Jana, *J. Alloy Compd.*, **2016**, 669,

177.

- [12] W. W. Cai, W. Z. Liu, J. L. Han and A. J. Wang, *Biosens. Bioelectron.*, **2016**, 80, 118.
- [13] W. J. Su, H. C. Chang, Y. T. Shih, Y. P. Wang, H. P. Hsu, Y. S. Huang and K. Y. Lee, *J. Alloy Compd.*, **2016**, 671, 276.
- [14] Q. Yang, J. Wu, K. Huang, M. Lei, W. J. Wang, S. S. Tang, P. J. Lu, Y. K. Lu and J. Liu, *J. Alloy Compd.*, **2016**, 667, 29.
- [15] H. H. Zhu, Y. L. Cao, J. Z. Zhang, W. L. Zhang, Y. H. Xu, J. X. Guo, W. R. Yang and J. Q. Liu, *J. Mater. Sci.*, **2016**, 51, 3675.
- [16] V. Thirumal, A. Pandurangan, D. Jayakumar and R. Ilangoan, *J. Mater. Sci.*, **2016**, 27, 3410.
- [17] X. Yu, Y. Kang and H. S. Park, *Carbon*, **2016**, 101, 49.
- [18] B. H. Xie, C. Yang, Z. X. Zhang, P. C. Zou, Z. Y. Lin, G. Q. Shi, Q. H. Yang, F. Y. Kang and C. P. Wong, *ACS Nano*, **2015**, 9, 5636.
- [19] H. N. Arnold, C. D. Cress, J. J. McMorrow, S. W. Schmucker, V. K. Sangwan, L. Jaber-Ansari, R. Kumar, K. P. Puntambekar, K. A. Luck, T. J. Marks and M. C. Hersam, *ACS Appl. Mater. Interfaces*, **2016**, 8, 5058.
- [20] Z. X. Sun, G. J. Wang, T. W. Cai, H. J. Ying and W. Q. Han, *Electrochim. Acta*, **2016**, 191, 299.

- [21] W. J. Li, C. Han, S. L. Chou, J. Z. Wang, Z. Li, Y. M. Kang, H. K. Liu and S. X. Dou, *Chem.-Eur. J.*, **2016**, 22, 590.
- [22] L. H. Yin, Y. X. Wang, C. C. Han, Y. M. Kang, X. Ma, H. Xie and M. B. Wu, *J. Power Sources*, **2016**, 305, 156.
- [23] G. Hasegawa, K. Kanamori, N. Kannari, J. Ozaki, K. Nakanishi and T. Abe, *ChemElectroChem*, **2015**, 2, 1917.
- [24] S. H. Choi, Y. N. Ko, J. K. Lee and Y. C. Kang, *Adv. Funct. Mater.*, **2015**, 25, 1780.
- [25] Y. C. Jiao, D. D. Han, L. M. Liu, L. Ji, G. N. Guo, J. H. Hu, D. Yang and A. G. Dong, *Angew. Chem. Int. Ed.*, **2015**, 54, 5727.
- [26] J. Q. Huang, Z. L. Xu, S. Abouali, M. A. Garakani and J. K. Kim, *Carbon*, **2016**, 99, 624.
- [27] W. N. Yan, X. C. Cao, J. H. Tian, C. Jin, K. Ke and R. Z. Yang, *Carbon*, **2016**, 99, 195.
- [28] M. S. Wang, M. Lei, Z. Q. Wang, X. Zhao, J. Xu, W. Yang, Y. Huang and X. Li, *J. Power Sources*, **2016**, 309, 238.
- [29] X. W. Wang, L. D. Zhang, Z. H. Zhang, A. S. Yu and P. Y. Wu, *Phys. Chem. Chem. Phys.*, **2016**, 18, 3893.
- [30] X. Y. Yu, L. Yu and X. W. Lou, *Adv. Energy Mater.*, **2016**, 6.
- [31] H. Zhang, *ACS Nano*, **2015**, 9, 9451.

- [32] X. Y. Chia, A. Y. S. Eng, A. Ambrosi, S. M. Tan and M. Pumera, *Chem. Rev.*, **2015**, 115, 11941.
- [33] Y. Z. Guo, D. M. Liu and J. Robertsont, *ACS Appl. Mater. Interfaces*, **2015**, 7, 25709.
- [34] A. S. Pawbake, M. S. Pawar, S. R. Jadkar and D. J. Late, *Nanoscale*, **2016**, 8, 3008.
- [35] R. T. Lv, H. Terrones, A. L. Elias, N. Perea-Lopez, H. R. Gutierrez, E. Cruz-Silva, L. P. Rajukumar, M. S. Dresselhaus and M. Terrones, *Nano Today*, **2015**, 10, 559.
- [36] X. K. Chen, Z. X. Xie, W. X. Zhou, L. M. Tang and K. Q. Chen, *Carbon*, **2016**, 100, 492.
- [37] H. Tokoyama, H. Yamakado and K. Ohno, *Chem. Lett.*, **2016**, 45, 333.
- [38] D. H. Lan, H. T. Wang, L. Chen, C. T. Au and S. F. Yin, *Carbon*, **2016**, 100, 81.
- [39] R. K. Zhang, H. L. An, Z. H. Li, M. F. Shao, J. B. Han and M. Wei, *Chem. Eng. J.*, **2016**, 289, 85.
- [40] H. Gwon, S. W. Kim, Y. U. Park, J. Hong, G. Ceder, S. Jeon and K. Kang, *Inorg. Chem.*, **2015**, 54, 2081.
- [41] M. Zhang, Z. J. Huang, X. Wang, H. Y. Zhang, T. H. Li, Z. L. Wu,

- Y. H. Luo and W. Cao, *Sci. Rep.*, **2016**, 6.
- [42] Y. Zhang, Y. Q. Yu, L. F. Mi, H. Wang, Z. F. Zhu, Q. Y. Wu, Y. G. Zhang and Y. Jiang, *Small*, **2016**, 12, 1062.
- [43] A. Kumar and P. K. Ahluwalia, *Eur. Phys. J. B*, **2012**, 85.
- [44] S. K. Balasingam, J. S. Lee and Y. Jun, *Dalton. Trans.*, **2015**, 44, 15491.
- [45] M. W. Xu, F. L. Yi, Y. B. Niu, J. L. Xie, J. K. Hou, S. G. Liu, W. H. Hu, Y. T. Li and C. M. Li, *J. Mater. Chem. A*, **2015**, 3, 9932.
- [46] Z. A. Zhang, X. Yang and Y. Fu, *RSC Adv.*, **2016**, 6, 12726.
- [47] W. Qin, T. Q. Chen, L. K. Pan, L. Y. Niu, B. W. Hu, D. S. Li, J. L. Li and Z. Sun, *Electrochim. Acta*, **2015**, 153, 55.
- [48] W. Y. Fang, H. B. Zhao, Y. P. Xie, J. H. Fang, J. Q. Xu and Z. W. Chen, *ACS Appl. Mater. Interfaces*, **2015**, 7, 13044.
- [49] T. Stephenson, Z. Li, B. Olsen and D. Mitlin, *Energy Environ. Sci.*, **2014**, 7, 209.
- [50] L. Y. Zhou, S. C. Yan, L. J. Pan, X. R. Wang, Y. Q. Wang and Y. Shi, *Nano Res.*, **2016**, 9, 857.
- [51] F. Y. Xiong, Z. Y. Cai, L. B. Qu, P. F. Zhang, Z. F. Yuan, O. K. Asare, W. W. Xu, C. Lin and L. Q. Mai, *ACS Appl. Mater. Interfaces*, **2015**, 7, 12625.

- [52] Y. Liu, M. Q. Zhu and D. Chen, *J. Mater. Chem. A*, **2015**, 3, 11857.
- [53] R. J. Chen, T. Zhao, W. P. Wu, F. Wu, L. Li, J. Qian, R. Xu, H. M. Wu, H. M. Albishri, A. S. Al-Bogami, D. Abd El-Hady, J. Lu and K. Amine, *Nano Lett.*, **2014**, 14, 5899.
- [54] N. Lingappan and D. J. Kang, *Electrochim. Acta*, **2016**, 193, 128.
- [55] W. Xiao, Y. H. Zhang, L. L. Tian, H. D. Liu, B. T. Liu and Y. Pu, *J. Alloy Compd.*, **2016**, 665, 21.
- [56] D. M. Kang, Q. L. Liu, R. Si, J. J. Gu, W. Zhang and D. Zhang, *Carbon*, **2016**, 99, 138.
- [57] X. Huang, C. L. Tan, Z. Y. Yin and H. Zhang, *Adv. Mater.*, **2014**, 26, 2185.
- [58] M. Ko, S. Chae, S. Jeong, P. Oh and J. Cho, *ACS Nano*, **2014**, 8, 8591.
- [59] M. Srivastava, J. Singh, T. Kuila, R. K. Layek, N. H. Kim and J. H. Lee, *Nanoscale*, **2015**, 7, 4820.
- [60] B. T. Zhang, G. L. Cui, K. J. Zhang, L. X. Zhang, P. X. Han and S. M. Dong, *Electrochim. Acta*, **2014**, 150, 15.
- [61] L. Y. Hu, X. S. Zhu, Y. C. Du, Y. F. Li, X. S. Zhou and J. C. Bao, *Chem. Mater.*, **2015**, 27, 8138.
- [62] X. Huang, S. Z. Li, Y. Z. Huang, S. X. Wu, X. Z. Zhou, S. Z. Li, C.

- L. Gan, F. Boey, C. A. Mirkin and H. Zhang, *Nat. Commun.*, **2011**, 2.
- [63] W. X. Guo, F. Zhang, C. J. Lin and Z. L. Wang, *Adv. Mater.*, **2012**, 24, 4761.
- [64] S. J. Haigh, A. Gholinia, R. Jalil, S. Romani, L. Britnell, D. C. Elias, K. S. Novoselov, L. A. Ponomarenko, A. K. Geim and R. Gorbachev, *Nat. Mater.*, **2012**, 11, 764.
- [65] C. Lee, H. Yan, L. E. Brus, T. F. Heinz, J. Hone and S. Ryu, *ACS Nano*, **2010**, 4, 2695.
- [66] J. Stadler, T. Schmid and R. Zenobi, *ACS Nano*, **2011**, 5, 8442.
- [67] A. Abherve, S. Manas-Valero, M. Clemente-Leon and E. Coronado, *Chem. Sci.*, **2015**, 6, 4665.
- [68] L. Ciric, A. Sienkiewicz, B. Nafradi, M. Mionic, A. Magrez and L. Forro, *Phys. Status Solidi B*, **2009**, 246, 2558.
- [69] J. Chen, B. W. Yao, C. Li and G. Q. Shi, *Carbon*, **2013**, 64, 225.
- [70] J. Chen, Y. R. Li, L. Huang, C. Li and G. Q. Shi, *Carbon*, **2015**, 81, 826.
- [71] H. B. Feng, Z. B. Hu and X. F. Liu, *Chem. Commun.*, **2015**, 51, 10961.
- [72] K. Funaki, K. Tezuka and Y. J. Shan, *Phys. Status Solidi A*, **2014**,

211, 901.

- [73] L. H. Yuwen, H. Yu, X. R. Yang, J. J. Zhou, Q. Zhang, Y. Q. Zhang, Z. M. Luo, S. Su and L. H. Wang, *Chem. Commun.*, **2016**, 52, 529.
- [74] G. L. Frey, K. J. Reynolds, R. H. Friend, H. Cohen and Y. Feldman, *J. Am. Chem. Soc.*, **2003**, 125, 5998.
- [75] J. Zheng, H. Zhang, S. H. Dong, Y. P. Liu, C. T. Nai, H. S. Shin, H. Y. Jeong, B. Liu and K. P. Loh, *Nat. Commun.*, **2014**, 5.
- [76] K. Lee and J. Ye, *Carbon*, **2016**, 100, 441.
- [77] S. S. Roy, R. M. Jacobberger, C. H. Wan and M. S. Arnold, *Carbon*, **2016**, 100, 1.
- [78] X. H. Zhang, M. Q. Xue, X. H. Yang, G. S. Luo and F. Yang, *Micro Nano Lett.*, **2015**, 10, 339.
- [79] L. C. Wang, L. Y. Chen, T. Luo, K. Bao and Y. T. Qian, *Solid State Commun.*, **2006**, 138, 72.
- [80] X. Zhang, Q. W. Zhang, Y. F. Sun, P. Y. Zhang, X. Gao, W. Zhang and J. X. Guo, *Electrochim. Acta*, **2016**, 189, 224.
- [81] M. Choucair, P. Thordarson and J. A. Stride, *Nat. Nanotechnol.*, **2009**, 4, 30.
- [82] Y. G. Li, H. L. Wang, L. M. Xie, Y. Y. Liang, G. S. Hong and H. J. Dai, *J. Am. Chem. Soc.*, **2011**, 133, 7296.

- [83] S. Ithurria, M. D. Tessier, B. Mahler, R. P. S. M. Lobo, B. Dubertret and A. Efros, *Nat. Mater.*, **2011**, 10, 936.
- [84] S. Ithurria and B. Dubertret, *J. Am. Chem. Soc.*, **2008**, 130, 16504.
- [85] J. S. Son, X. D. Wen, J. Joo, J. Chae, S. I. Baek, K. Park, J. H. Kim, K. An, J. H. Yu, S. G. Kwon, S. H. Choi, Z. W. Wang, Y. W. Kim, Y. Kuk, R. Hoffmann and T. Hyeon, *Angew. Chem. Int. Ed.*, **2009**, 48, 6861.
- [86] Y. P. Du, Z. Y. Yin, J. X. Zhu, X. Huang, X. J. Wu, Z. Y. Zeng, Q. Y. Yan and H. Zhang, *Nat. Commun.*, **2012**, 3.
- [87] S. Goriparti, E. Miele, F. De Angelis, E. Di Fabrizio, R. P. Zaccaria and C. Capiglia, *J. Power Sources*, **2014**, 257, 421.
- [88] R. Marom, S. F. Amalraj, N. Leifer, D. Jacob and D. Aurbach, *J. Mater. Chem.*, **2011**, 21, 9938.
- [89] M. Armand and J. M. Tarascon, *Nature*, **2008**, 451, 652.
- [90] M. Winter and R. J. Brodd, *Chem. Rev.*, **2004**, 104, 4245.
- [91] F. Y. Cheng, J. Liang, Z. L. Tao and J. Chen, *Adv. Mater.*, **2011**, 23, 1695.
- [92] M. M. Thackeray, C. Wolverton and E. D. Isaacs, *Energy Environ. Sci.*, **2012**, 5, 7854.
- [93] J. B. Goodenough and K. S. Park, *J. Am. Chem. Soc.*, **2013**, 135,

1167.

- [94] K. Persson, V. A. Sethuraman, L. J. Hardwick, Y. Hinuma, Y. S. Meng, A. van der Ven, V. Srinivasan, R. Kostecki and G. Ceder, *J. Phys. Chem. Lett.*, **2010**, 1, 1176.
- [95] B. J. Landi, M. J. Ganter, C. D. Cress, R. A. DiLeo and R. P. Raffaele, *Energy Environ. Sci.*, **2009**, 2, 638.
- [96] C. Kim, K. S. Yang, M. Kojima, K. Yoshida, Y. J. Kim, Y. A. Kim and M. Endo, *Adv. Funct. Mater.*, **2006**, 16, 2393.
- [97] J. Jiang, Y. Y. Li, J. P. Liu, X. T. Huang, C. Z. Yuan and X. W. Lou, *Adv. Mater.*, **2012**, 24, 5166.
- [98] C. H. Lai, M. Y. Lu and L. J. Chen, *J. Mater. Chem.*, **2012**, 22, 19.
- [99] L. W. Ji, Z. Lin, M. Alcoutlabi and X. W. Zhang, *Energy Environ. Sci.*, **2011**, 4, 2682.
- [100] H. D. Yoo, I. Shterenberg, Y. Gofer, G. Gershinsky, N. Pour and D. Aurbach, *Energy Environ. Sci.*, **2013**, 6, 2265.
- [101] S. W. Kim, D. H. Seo, X. H. Ma, G. Ceder and K. Kang, *Adv. Energy Mater.*, **2012**, 2, 710.
- [102] S. Y. Hong, Y. Kim, Y. Park, A. Choi, N. S. Choi and K. T. Lee, *Energy Environ. Sci.*, **2013**, 6, 2067.
- [103] K. Kubota and S. Komaba, *J. Electrochem. Soc.*, **2015**, 162, A2538.

- [104] Y. Kim, Y. Kim, A. Choi, S. Woo, D. Mok, N. S. Choi, Y. S. Jung, J. H. Ryu, S. M. Oh and K. T. Lee, *Adv. Mater.*, **2014**, 26, 4139.
- [105] D. Peramunage and S. Licht, *Science*, **1993**, 261, 1029.
- [106] P. G. Bruce, S. A. Freunberger, L. J. Hardwick and J. M. Tarascon, *Nat. Mater.*, **2012**, 11, 19.
- [107] A. Manthiram, Y. Z. Fu, S. H. Chung, C. X. Zu and Y. S. Su, *Chem. Rev.*, **2014**, 114, 11751.
- [108] Y. V. Mikhaylik and J. R. Akridge, *J. Electrochem. Soc.*, **2004**, 151, A1969.
- [109] H. M. Kim, J. Y. Hwang, A. Manthiram and Y. K. Sun, *ACS Appl. Mater. Interfaces*, **2016**, 8, 983.
- [110] S. K. Liu, Y. J. Li, X. B. Hong, J. Xu, C. M. Zheng and K. Xie, *Electrochim. Acta*, **2016**, 188, 516.
- [111] X. Li, Q. Sun, J. Liu, B. W. Xiao, R. Y. Li and X. L. Sun, *J. Power Sources*, **2016**, 302, 174.

# **Chapter 2. Synthesis of MoS<sub>2</sub>/Porous Carbon Nanosheet Nanocomposites for High-Performance Lithium and Sodium Ion Battery Anodes**

## **2.1. Introduction**

Rechargeable Li-ion batteries (LIBs), which have the advantages of excellent properties, such as high energy density, design flexibility, and long cycle life, are considered to be a dominant power source for transportation, consumer electronics, and energy-storage devices [1, 2]. In contrast, Na-ion batteries (SIBs) are seen as promising options for large-scale commercial energy-storage systems (such as grid storage) because of the abundant reserves and even distribution of this element worldwide [3, 4]. However, in current technologies, the energy densities and rate capabilities of both LIBs and SIBs are insufficient to completely satisfy social needs. To fundamentally solve these problems, it is

necessary to develop advanced electrode materials with higher stability and capacity than those that are currently used. Furthermore, exploring electrode materials capable of storing both  $\text{Li}^+$  and  $\text{Na}^+$  would be of great importance.

$\text{MoS}_2$ , which features a layered structure resembling that of graphite, is a promising anode material in both LIBs and SIBs because its specific capacity is higher than that of commercial carbonaceous materials [5-12]. However, because of its high surface energy and interlayer van der Waals forces, [13] two-dimensional (2D) nanosheets inevitably restack during the cycling process, causing a rapid capacity decrease and poor rate performance [14-16]. This behavior is especially important for  $\text{Na}^+$  storage because Na atoms are larger than Li atoms. To overcome these issues, various strategies have been proposed to enhance the structural stability of  $\text{MoS}_2$ -based anodes. One effective strategy is to assemble the  $\text{MoS}_2$  nanosheets into a three-dimensional (3D) porous structure able to retain the large surface area and offer more active sites for ion intercalation [17-22]. For example, Yang's group reported 3D radially oriented  $\text{MoS}_2$  nanospheres constructed by few-layered 2D  $\text{MoS}_2$  nanosheets, which exhibited high specific capacity and excellent rate capability when used as anode materials for LIBs [20].

Another strategy is to expand the interlayer distance between the MoS<sub>2</sub> nanosheets by introducing carbon buffer layers or using surfactants or physicochemical methods [23-27]. This strategy can provide sufficient open channels for fast ion intercalation and inhibit the aggregation of the 2D nanosheets. It has been reported that the carbon layers between MoS<sub>2</sub> nanosheets provide not only the electrode's electric conductivity but also buffer spaces to accommodate the volume changes during the cycling process. However, currently, complicated and harsh synthetic processes are required to achieve the above strategies, such as hydrothermal, solvothermal, and chemical vapor deposition (CVD) techniques; these are the main obstacles to mass producing these materials because these methods require expensive facilities, are time consuming, and are limited to small-sized reaction vessels [28-31]. Furthermore, synthesizing MoS<sub>2</sub>/carbon nanocomposites with both expanded interlayer distances and 3D porous structures remains challenging.

In this work, we demonstrate an effective and simple solventless method to synthesize few-layer MoS<sub>2</sub> incorporated into hierarchical porous carbon (MHPC) nanosheets in which MoS<sub>2</sub> nanosheets are very uniformly distributed over the porous carbon sheets. In this synthesis strategy, oleylamine plays important roles as not only a carbon precursor

to provide the electrical pathway but also as a surfactant to prevent the restacking of MoS<sub>2</sub> nanosheets via complex formation with [MoS<sub>4</sub>]<sup>2-</sup>. In addition, silica templates provide an “inverse opal structured substrate” to direct the growth of a hierarchical porous structured nanosheets network. As a result, the as-prepared few-layer MoS<sub>2</sub>/carbon nanosheets have open structures, which facilitate the efficient diffusion and transport of ions and electrons throughout the electrode and also provide sufficient void space to buffer the volume changes of MoS<sub>2</sub> during cycling. Furthermore, the expanded interlayer distance of the MoS<sub>2</sub> nanosheets benefits fast ion intercalation and provides structural stability, leading to long-term cyclability. As expected, these novel structured nanosheets exhibit outstanding cycling performance and rate capability for both LIBs and SIBs. In addition, this synthetic method may be suitable for mass production.

## **2.2. Experimental Section**

### **2.2.1. Chemicals**

Ammonium tetra thiomolybdate (ATTM, > 99.97 %), oleylamine (OA, technical grade, 70 %) were purchased from Aldrich Chemical Co. Sodium hydroxide (bead, > 98 %) was purchased from Samchun. Silicon(IV) oxide, (powder, 0.5 micron, 99.9 %) was purchased from Alfa Aesar.

### **2.2.2. Characterization methods**

The morphologies of all samples were observed by FE-SEM (Hitachi S-4800). The TEM images were obtained using a TEM instrument (JEOL JEM-2010). XPS analyses were performed using an AXIS-His spectrometer with a monochromatic Al K $\alpha$  source. A Mettler Toledo TGA/DSC 1 model was used for TGA. Crystal phases were identified using an XRD instrument (D8-advance) equipped with a Cu K $\alpha$  source operating at 40 mA and 40 kV with a scan range of 5–80°. N<sub>2</sub>-sorption measurements were performed on a BELSORP-mini II.

### **2.2.3. Synthesis of few-layer MoS<sub>2</sub>/hierarchical porous carbon (MHPC) nanosheet hybrids**

The MHPC composites were prepared using a solventless process. Typically, 0.1 g of ATTM was solventlessly mixed with 0.2 ml OA by

using a mortar and pestle until completely combined. Then, the obtained red precursor mixture was combined with 0.15 g of commercial SiO<sub>2</sub> nanoparticles using a mortar and pestle. After mixing thoroughly, the mixture was transferred to an alumina boat for thermal processing at 800 °C for 2 h under a N<sub>2</sub>/H<sub>2</sub> (5 %) atmosphere. Finally, the resulting black powder was dispersed in aqueous NaOH at 90 °C for 6 h to remove the silica. The composite was collected by filtration with deionized (DI) water and ethanol. The content of MoS<sub>2</sub> nanosheets in the composites was particularly easily tunable by adjusting the amount of ATTM. In this study, three different amounts (0.05, 0.1, and 0.2 g) were tested, and the composites were named MHPC-0.05, MHPC-0.1, and MHPC-0.2 for convenience. For the control experiment, MoS<sub>2</sub>/C composites were prepared using the same procedure without SiO<sub>2</sub> nanoparticles (OA: 0.2 mL, ATTM: 0.1 g). In addition, MoS<sub>2</sub> nanoparticles were synthesized using only ATTM.

#### **2.2.4. Electrochemical Characterization**

To evaluate the electrochemical performance of the samples, a slurry composed of 70 wt% active materials, 15 wt% Super-P, and 15 wt% polyvinylidene fluoride (PVDF) in *n*-methyl-2-pyrrolidone (NMP) was applied on a Cu foil. After vacuum drying, 2016-type coin cells were

fabricated in an Ar-filled glove box. Li metal or Na metal was used as the reference and counter electrodes, and the electrolyte was 1.0-M LiPF<sub>6</sub> in a 1:1 v/v mixture of diethyl carbonate (DEC) and ethylene carbonate (EC) or NaClO<sub>4</sub> in a 1:1:1 v/v mixture of EC, DEC, and poly carbonate (PC) for LIBs and SIBs, respectively. Charge/discharge tests were performed on a WBCS3000s cyler (WonATech, Korea) using a voltage window of 0.01–3.0 V vs. Li/Li<sup>+</sup> or 0.01–2.9 V vs. Na/Na<sup>+</sup>. Electrochemical impedance spectroscopy (EIS) was conducted in the range of 100 kHz to 10 mHz with an AC amplitude of 5 mV on CHI 660e model.

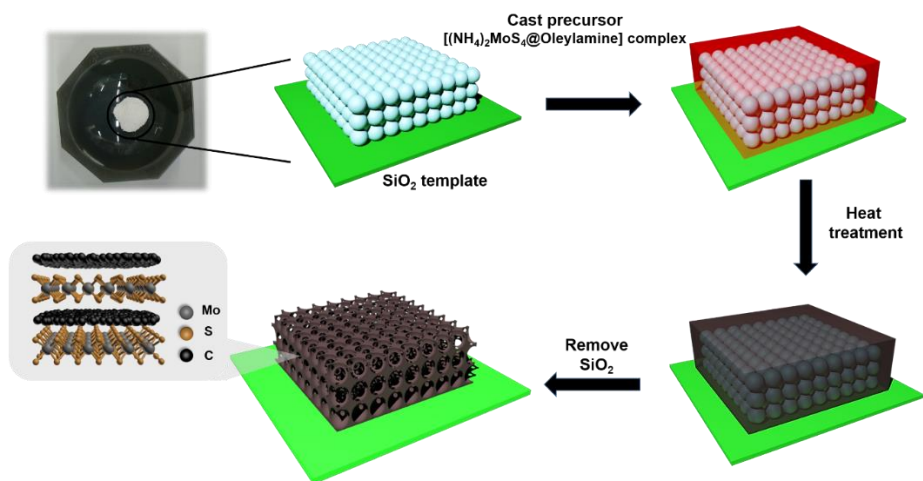


**Figure 2.1.** Schematic Depicting the Synthesis Procedure of MHPC Composites.

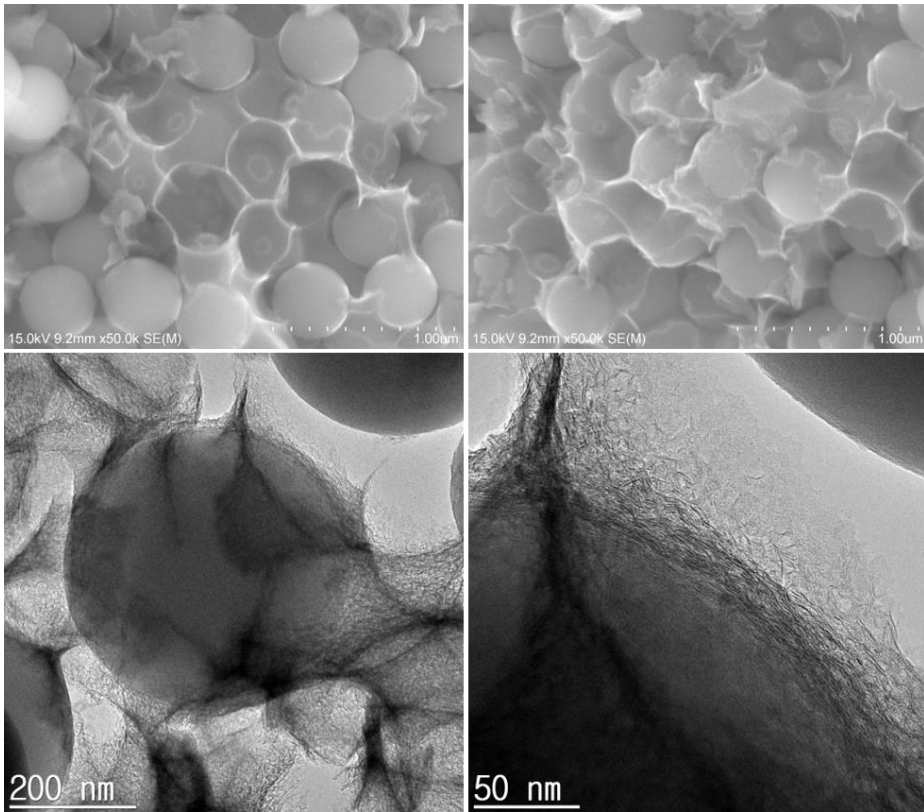


**Figure 2.2.** SEM and TEM images of MHPC composite before silica etching

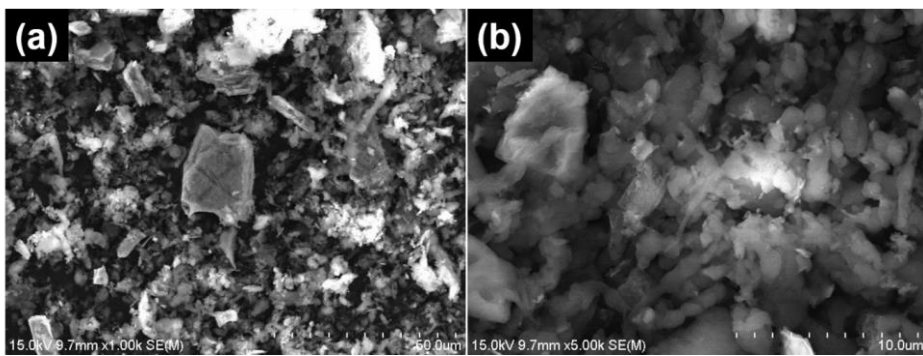


**Figure 2.3.** (a) Low- and (b) high-magnification SEM images of MoS<sub>2</sub>/C composites synthesized by using oleic acid as the precursors.



**Figure 2.4.** Large scale synthesis of MHPC composites (using 1 ml of OA and 0.52 g of ATTU)

### 2.3. Results and Discussion

The route used to prepare the MHPC composites is illustrated in **Figure 2.1**. In the first step, the as-prepared SiO<sub>2</sub> nanoparticles were mixed with ammonium tetrathiomolybdate (ATTM)/OA precursor in a mortar. The MoS<sub>2</sub> content was easily tunable by adjusting the amount of ATTM. In this experiment, three different amounts (0.05, 0.1, and 0.2 g) were tested, and the composites were named MHPC-0.05, MHPC-0.1, and MHPC-0.2, respectively, for convenience. Then, the resulting sticky mixture was heated for 2 h under a N<sub>2</sub>/H<sub>2</sub> (5 %) atmosphere. During the thermal processing, OA was converted into conductive carbon, which firmly deposited on the SiO<sub>2</sub> template, and the in situ formation of few-layer MoS<sub>2</sub> nanosheets from ATTM occurred inside the forming carbon (**Figure 2.2**). To understand the roles of the OA additive, an experiment was designed and performed in which we substitute oleic acid with a carboxylic acid end group for OA under the same conditions as those used for the preparation of MHPC composites. Interestingly, we were able to obtain irregularly shaped microparticles without 2D nanosheet structures, suggesting that the ATTM/oleic acid precursor cannot form complexes (**Figure 2.3**). According to a previous report, this is because

the negatively charged tetrahedral  $[\text{MoS}_4]^{2-}$  in ATTMM can electrostatically interact with only positively charged (amine-terminated) additives [32]. As a result, the  $\text{MoS}_2$  sheets are covered by a protective coating of OA that effectively suppresses aggregation and stacking phenomena, thus ensuring more active sites. Finally, the MHPC composites were obtained after removing the  $\text{SiO}_2$  nanoparticles. Importantly, the above thermal processing was carried out using solid-phase foam without any solvents, which makes this in situ synthesis approach very inexpensive, easily controllable, and suitable for the mass production of  $\text{MoS}_2$ -based composites. Indeed, using only 1 mL of OA and 0.52 g of ATTMM yielded 0.43 g of the MHPC (**Figure 2.4**). Furthermore, because the OA-ATTMM precursor exists in the liquid phase, it can be easily mixed with templates of various shapes, implying that the morphology of the resulting  $\text{MoS}_2/\text{C}$  composites can be readily controlled.

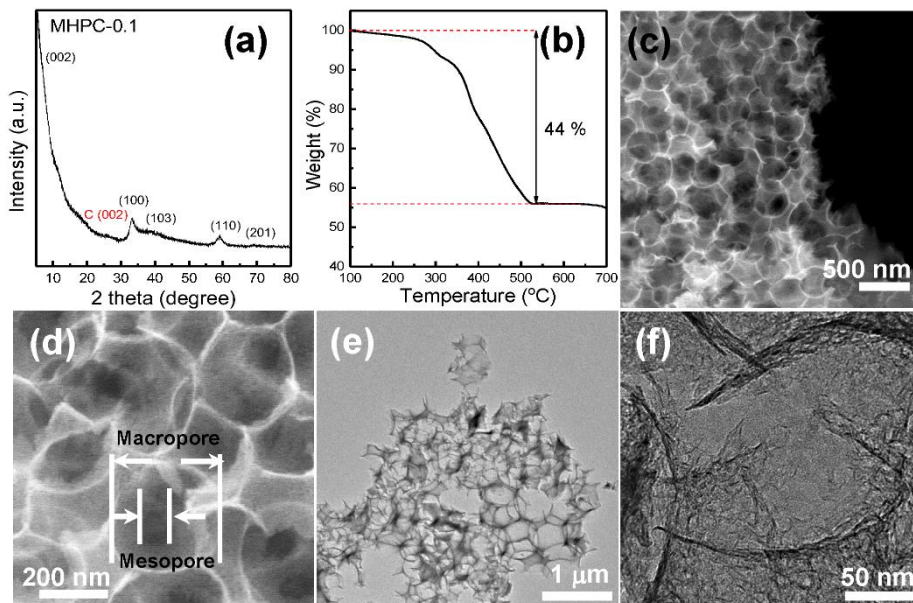


**Figure 2.5.** (a) XRD pattern, (b) TGA curve, (c, d) SEM images, and (e, f) TEM images of MHPC-0.1 composites.

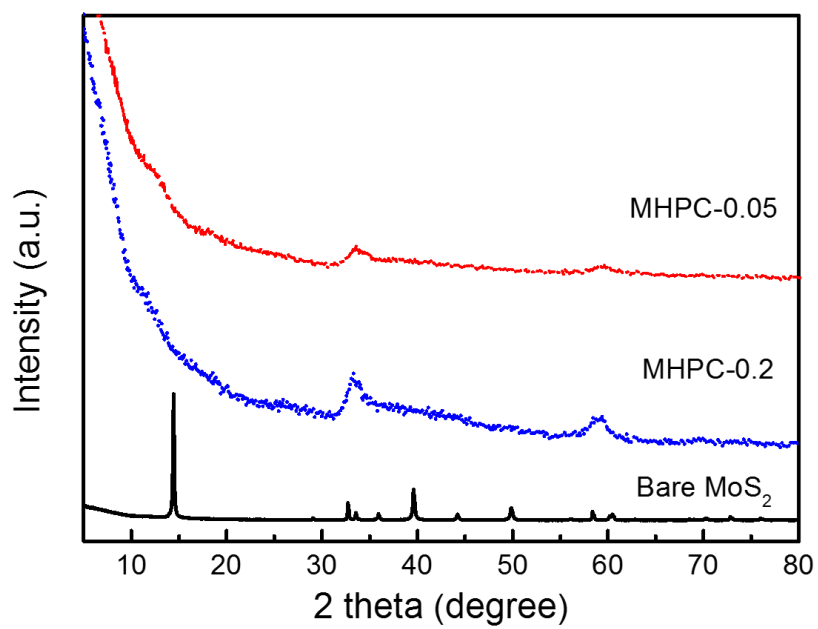


**Figure 2.6.** XRD pattern of MHPC-0.05, MHPC-0.2 and MoS<sub>2</sub> powder synthesized without OA.

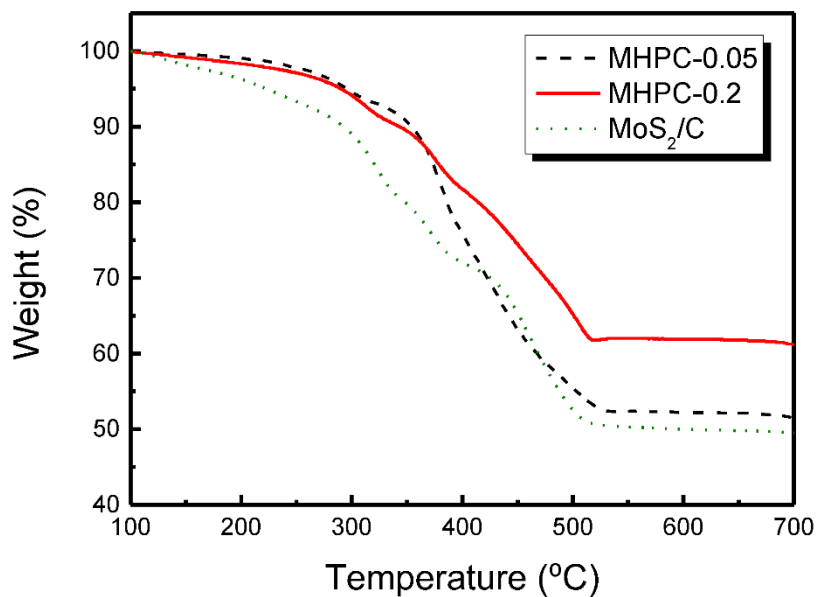


**Figure 2.7.** TGA curves of MHPC-0.05, MHPC-0.2, and MoS<sub>2</sub>/C composites

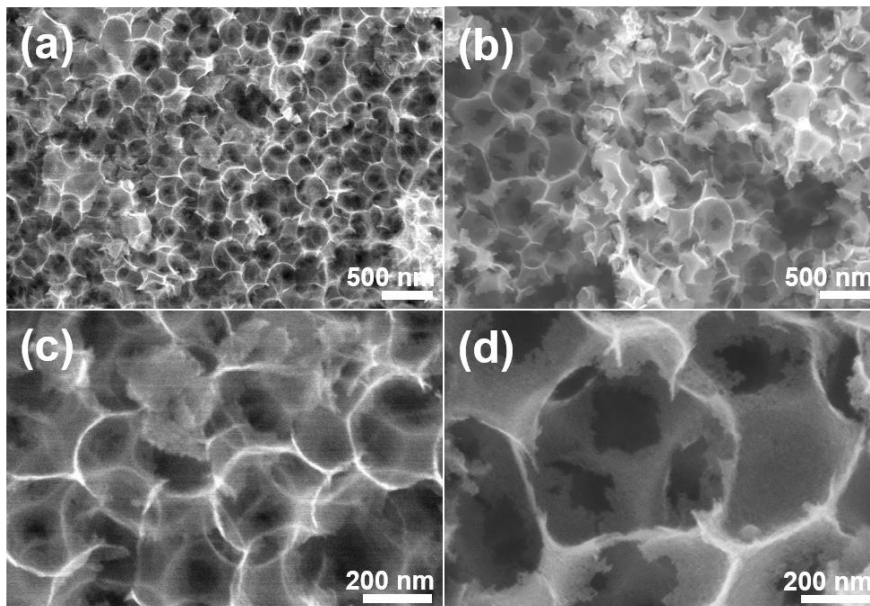


**Figure 2.8.** SEM images of (a, c) MHPC-0.05 and (b, d) MHPC-0.2 composites

**Figure 2.5a** shows the X-ray diffraction (XRD) pattern of MHPC-0.1 composites. Except for the weak diffraction peak at  $25^\circ$  that is attributed to the carbon phase, all of the identified peaks agree well with previous reports, indicating the phase purity of the  $\text{MoS}_2$  nanosheets in the MHPC composites [33, 34]. Compared to the XRD pattern of bare  $\text{MoS}_2$  powder, all the broad peaks indicate that the crystallites are at the nanoscale (**Figure 2.6**). In particular, the diffraction peak of the (002) plane at approximately  $14^\circ$ , which is assigned to the ordered stacking of  $\text{MoS}_2$  sheets, is barely observable, implying that the MHPC-0.1 composites contain few-layered  $\text{MoS}_2$  nanosheets [35, 36]. This interesting phenomenon may be attributed to the involvement of OA during the synthetic process. According to previous reports, these few-stacked  $\text{MoS}_2$  nanosheets can decrease the diffusion paths for ion transfer, leading to fast rate performance [21, 37-39]. In addition, MHPC-0.05 and 0.2 also show very weak peaks at  $14^\circ$ , suggesting that even a small amount of OA is sufficient to inhibit the restacking of  $\text{MoS}_2$  nanosheets. From the thermogravimetric analysis (TGA) curve of MHPC-0.1, we were able to estimate that the  $\text{MoS}_2$  content is approximately 62.3 %, assuming that the final product after measurement was pure  $\text{MoO}_3$  (**Figure 2.5b**). The carbon contents in MHPC-0.05 and MHPC-0.2 with

different ATTM amounts were approximately 41.1 and 32.6 wt%, respectively, which suggests that the carbon content can be determined by the amount of precursors (**Figure 2.7**).

**Figures 2.5c and d** show the field emission scanning electron microscopy (FE-SEM) images of a MHPC-0.1 nanocomposite. The analyzed sample has a highly interconnected 3D structure with macro- and mesopores, and the exposed edges of the network walls exhibit clear corrugation and low contrast, indicating that these ultrathin ( $< 4$  nm) sheets have great mechanical flexibility. In contrast, MHPC-0.2 shows slightly thicker sheets and less-developed pore structure and size (**Figure 2.8**). These morphological differences are caused by the presence of excess ATTM and the resulting high viscosity. Meanwhile, the MoS<sub>2</sub>/C composites synthesized without SiO<sub>2</sub> nanoparticles contain agglomerated microparticles, indicating that the SiO<sub>2</sub> precursor ratio is a critical factor for the synthesis of MoS<sub>2</sub>/carbon nanocomposites with well-developed porous structures (**Figure 2.9**). Examining the transmission electron microscopy (TEM) images of MHPC-0.1 in detail provide additional confirmation of the existence of an interconnected 3D network, but in MHPC-0.2, some agglomerates were found (red circles in **Figure 2.10b**), as in the SEM images.

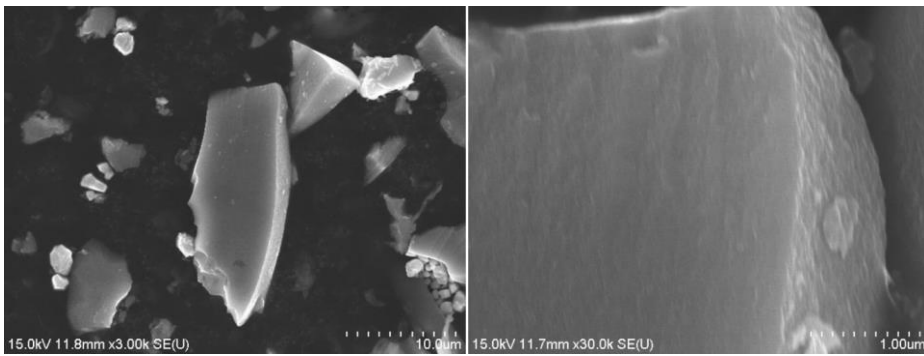


**Figure 2.9.** SEM images of MoS<sub>2</sub>/C composites synthesized without SiO<sub>2</sub> template.

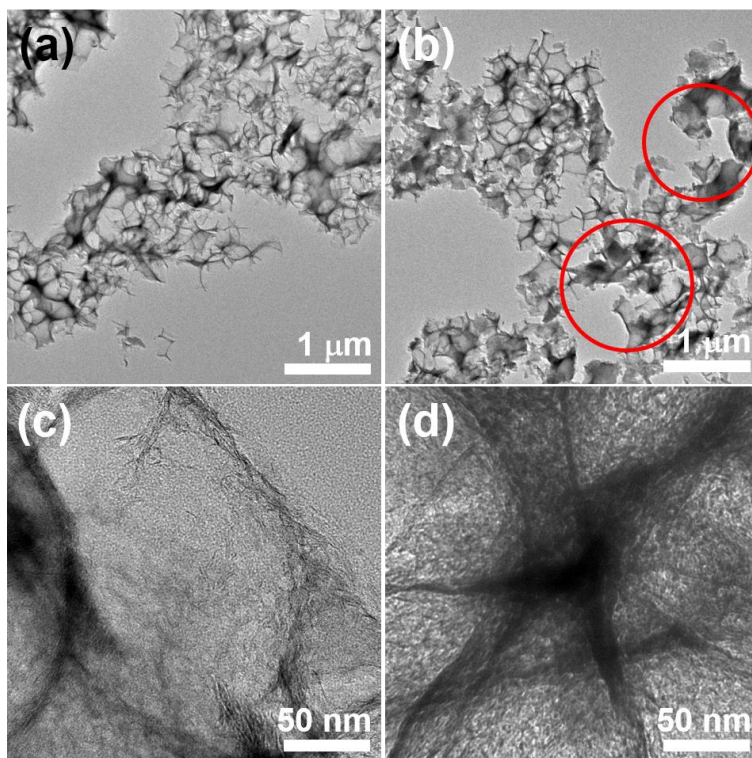


**Figure 2.10.** TEM images of (a, c) MHPC-0.05 and (b, d) MHPC-0.2 composites.

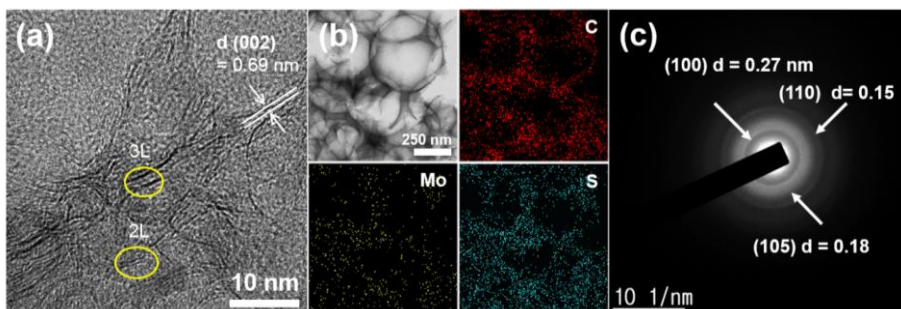


**Figure 2.11.** (a) A HR-TEM image, (b) SAED pattern, and (c) a TEM image and corresponding C, Mo, and S element mapping of MHPC-0.1.

The detailed microstructures of the MHPC nanocomposites were further characterized by high-resolution transmission electron microscopy (HR-TEM), selected-area electron diffraction (SAED), and elemental mapping (**Figure 2.11**). In the HR-TEM image in **Figure 2.11a**, we can observe the stacking and distribution of the MoS<sub>2</sub> nanosheets, which are distributed along the carbon network walls. This result provides an additional evidence that the ATTM precursor can form complexes with OA. Correspondingly, the stacked MoS<sub>2</sub> nanosheets are difficult to identify in all samples (**Figures 2.10c and d**). Energy-dispersive X-ray spectroscopy (EDX) scanning elemental mapping of Mo, S, and C elements also verified the formation of MoS<sub>2</sub> nanosheets inside the 3D carbon network (**Figure 2.11b**). This intimate contact between carbon and MoS<sub>2</sub> nanosheets not only effectively hinders the restacking and aggregation of MoS<sub>2</sub> nanosheets and improve the material's cycling stability but also substantially promotes fast ion and electron transport across the interface and enhances the rate capacity [40-43]. The circle mode in the SAED pattern further confirms the presence of polycrystalline MoS<sub>2</sub> (**Figure 2.11c**).

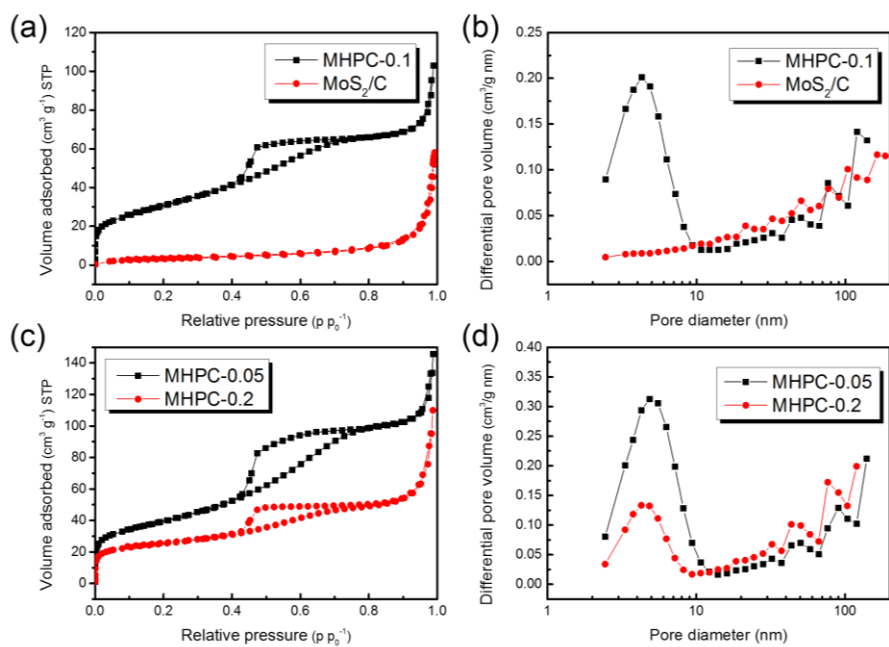


**Figure 2.12.** (a, c) The N<sub>2</sub>-sorption isotherms of MHPC-0.05, 0.1, 0.2 and MoS<sub>2</sub>/C and (b, d) their pore size distribution curves.

The Brunauer-Emmett-Teller (BET) specific surface areas and pore structures of the MHPC and MoS<sub>2</sub>/C composites were characterized by N<sub>2</sub>-sorption measurements (**Figure 2.12**). Unlike the MoS<sub>2</sub>/C composite, all the MHPC products show typical IV isotherm graphs, indicating the existence of mesoporous structures [44-45]. These pore structures are in good agreement with the SEM and TEM images. The specific surface area and pore volume of the MoS<sub>2</sub>/C composite were significantly increased by the use of SiO<sub>2</sub> nanoparticles as templates: from 12.7 to 109.7 m<sup>2</sup> g<sup>-1</sup> and from 0.082 to 0.19 cm<sup>3</sup> g<sup>-1</sup>, respectively (for MHPC-0.1). Therefore, the template is clearly an important determinant for the specific surface area and pore volume. Additionally, the surface area and pore volume tend to decrease as the amount of ATTM precursor is increased because of high MoS<sub>2</sub> mass loading (MHPC-0.05: 138.6 9 m<sup>2</sup> g<sup>-1</sup> and 0.23 cm<sup>3</sup> g<sup>-1</sup>; MHPC-0.2: 90.9 m<sup>2</sup> g<sup>-1</sup> and 0.17 cm<sup>3</sup> g<sup>-1</sup>).

The pore sizes of the MHPC composites were investigated using Barrett-Joyner-Halenda (BJH) pore size distribution data (**Figure 2.12b and d**). Interestingly, in the MoS<sub>2</sub>/C composites, most of the pores exceeded 20 nm, whereas the BJH plot of the MHPC-0.1 sample shows two important regions located below 10 nm and above 100 nm. This is clear evidence that the MHPC composites have a hierarchical porous

structure consisting of meso- and macropores. Clearly, the macropores were formed by removing the SiO<sub>2</sub> nanoparticle template, whereas the mesopores in the MHPC composites may be attributed to the release of gas during the thermal processing.

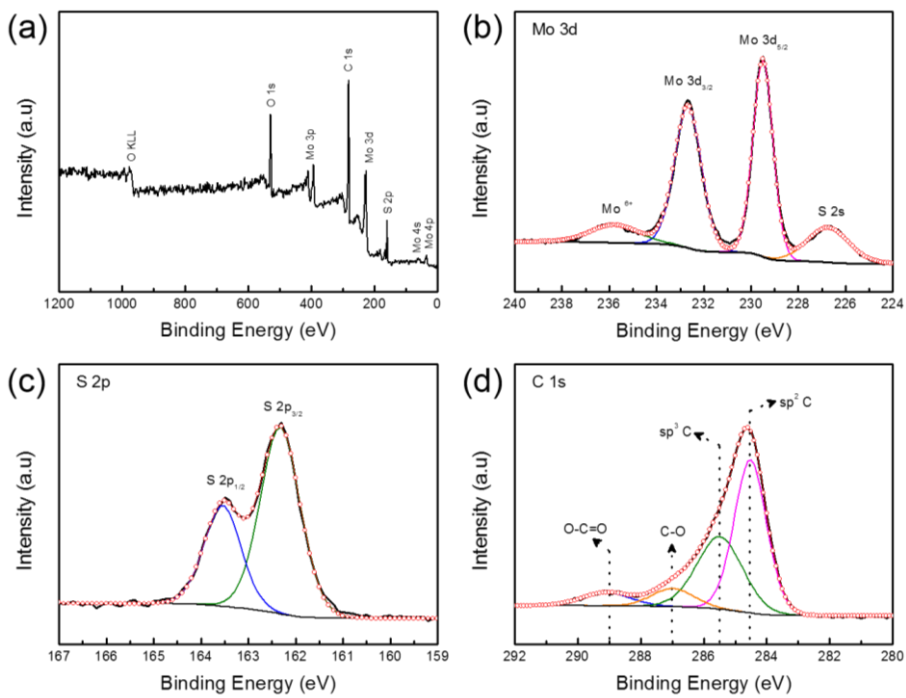


**Figure 2.13.** (a) XPS survey spectrum of MHPC-0.1 composite. High-resolution XPS spectra of (b) Mo 3d, (c) S 2p, and (d) C 1s of MHPC-0.1 composite.

**Table 2.1.** Atomic and mass concentration of Mo, S and C of MHPC-0.1 from high resolution XPS peak integration.

<b>Peak</b>	<b>Position BE (eV)</b>	<b>FWHM (eV)</b>	<b>Atomic Mass</b>	<b>Atomic Conc %</b>	<b>Mass Conc %</b>
S 2p	166.5	1.879	32.065	12.06	19.67
Mo 3d	227.3	0.929	95.922	6.23	30.40
C 1s	282.4	1.646	12.011	81.71	49.93

To further investigate the chemical information and surface electronic states of MHPC composites, X-ray photoelectron spectroscopy (XPS) was conducted (**Figure 2.13**). As shown in Figure 5a, the survey XPS spectrum shows the presence of Mo, S, O, and C elements in the MHPC composites, which is consistent with the EDX data. In the high-resolution XPS spectra of Mo 3d, two peaks are observed at 229.5 and 232.7 eV, which are assigned to Mo 3d<sub>5/2</sub> and Mo 3d<sub>3/2</sub>, respectively (**Figure 2.13b**). These values are known to correspond to Mo<sup>4+</sup> in MoS<sub>2</sub>. Additionally, the XPS peak at 235.8 eV is ascribed to Mo<sup>6+</sup> 3d<sub>5/2</sub> of MoO<sub>3</sub>, which may have been produced via partial surface oxidation in air [46, 47]. Furthermore, the small peak at 226.7 eV corresponds to the S 2s species of MoS<sub>2</sub> [48]. **Figure 2.13c** shows the high-resolution S 2p spectrum, which contains S 2p<sub>3/2</sub> and S 2p<sub>1/2</sub> peaks at 162.3 and 163.5 eV, respectively. These results are characteristic of S<sup>2-</sup> in MoS<sub>2</sub>. The deconvoluted C 1s spectra of the MHPC-0.1 composite show four different peaks centered at 284.5, 2885.5, 287.0, and 289.0 eV, which are attributed to sp<sup>2</sup> C, sp<sup>3</sup> C, C-O, and O-C=O groups, respectively (**Figure 2.13d**). The sp<sup>3</sup>/sp<sup>2</sup> concentration ratio (0.67) shows that the carbon in the composites consists of a partial amorphous phase and a dominant graphitic phase.

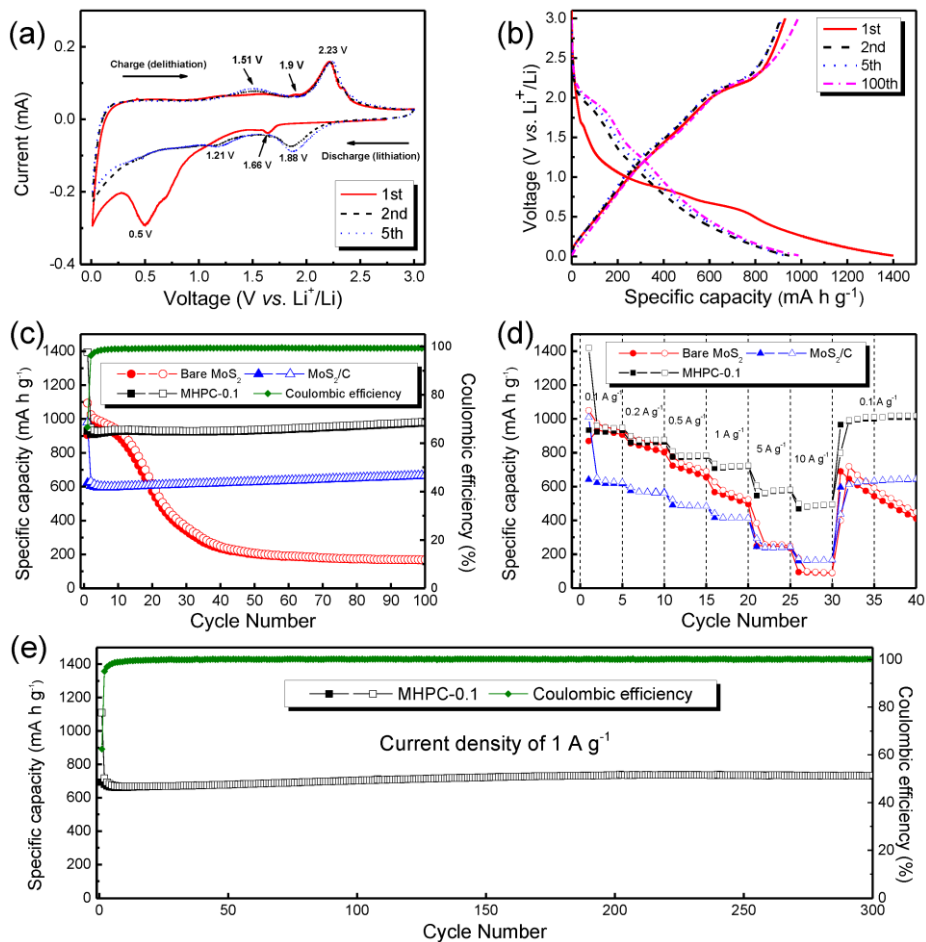


**Figure 2.14.** Electrochemical performance of MHPC-0.1 and MoS<sub>2</sub>/C used in LIBs. (a) CVs of MHPC-0.1 at a scanning rate of 0.2 mV s<sup>-1</sup>. (b) Galvanostatic discharge/charge profiles of MHPC-0.1 at 0.1 A g<sup>-1</sup>. (c) Cycling and (d) rate capability performance of MHPC-0.1, MoS<sub>2</sub>/C composites, and bare MoS<sub>2</sub> powder electrodes. (e) Long-term cycling performance at a current density of 1 A g<sup>-1</sup>.

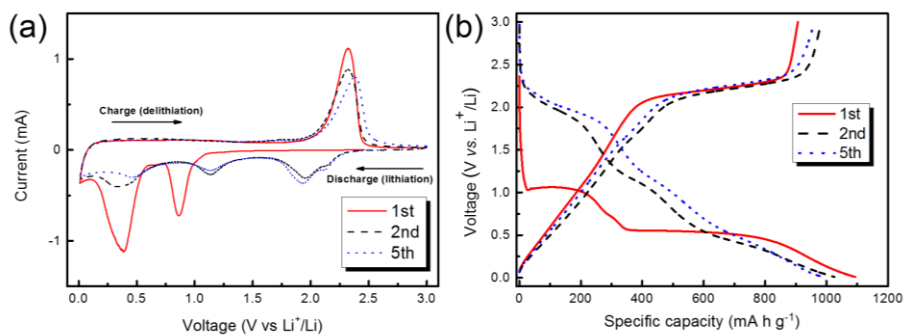


**Figure 2.15.** (a) Cyclic voltammograms of bare MoS<sub>2</sub> at a scanning rate of 0.2 mV s<sup>-1</sup>. (b) Galvanostatic discharge/charge profiles of bare MoS<sub>2</sub> at 0.1 A g<sup>-1</sup>.

The electrochemical properties of bare MoS<sub>2</sub>, MoS<sub>2</sub>/C, and MHPC-0.1 for use in LIBs were evaluated according to the results shown in **Figure 2.14**. **Figure 2.14a** shows the cyclic voltammograms (CVs) of the first, second, and fifth cycles of the MHPC-0.1 electrode in the potential range of 0.01–3 V vs Li<sup>+</sup>/Li. As previously reported, a dominant cathodic peak appears at 0.5 V only in the first cycle; this peak is associated with the reaction between Li<sub>x</sub>MoS<sub>2</sub> and Li<sup>+</sup>, which leads to the formation of metallic Mo nanoparticles and Li<sub>2</sub>S [6, 9]. From the second cycle on, two new reduction peaks at 1.88 V and 1.21 V emerge, which can be ascribed to the multi-step Li<sup>+</sup>-insertion mechanism [49]. Upon charging, the two main peaks that appear at 1.51 V and 2.23 V correspond to the oxidation of Li<sub>2</sub>S to S and Li<sup>+</sup>; they exhibit no significant variation, even after the fifth cycle, indicating the favorable reversibility of the MHPC electrodes. Furthermore, the weak oxidation peak at 1.9 V and reduction peak at 1.66 V (**Figure 2.15a**), which were not apparent in the CVs of the bare MoS<sub>2</sub> electrode, can be ascribed to reversible Li storage on the hierarchical porous carbon nanosheets. This suggests that both the few-layered MoS<sub>2</sub> and the 3D carbon nanosheets can store Li<sup>+</sup> during the charge/discharge process.

**Figure 2.13b** shows the charge/discharge voltage profiles of MHPC-0.1 for the first, second, fifth, and tenth cycles at a current density of 0.1 A g<sup>-1</sup>. Compared to that of bare MoS<sub>2</sub>, the profiles of MHPC-0.1 exhibit poor voltage plateaus, which is in good agreement with its CVs (**Figure 2.14b**). This result is caused by the combined effects of hierarchical porous carbon and few-layered MoS<sub>2</sub> nanosheets. In the first cycle, the MHPC-0.1 electrode delivers a discharge capacity of 1400 mA h g<sup>-1</sup> and a charge specific capacity of 925 mA h g<sup>-1</sup>, indicating a Coulombic efficiency of 66 %. The irreversible capacity loss is mainly caused by electrolyte decomposition and the formation of a solid-electrolyte interface (SEI) [50, 51]. However, in the subsequent cycles, both charge-discharge profiles remained nearly constant, implying excellent stability of MHPC-0.1 electrode.

The cycle behaviors of bare MoS<sub>2</sub>, MoS<sub>2</sub>/C, and MHPC-0.1 at a current density of 0.1 A g<sup>-1</sup> are shown in **Figure 2.14c**, together with their Coulombic efficiencies. MHPC-0.1 delivered reversible specific discharge capacities of 947 and 983 mA h g<sup>-1</sup> at the 2<sup>nd</sup> cycle and after 100 cycles, respectively, confirming that this material's specific capacity increases with cycling. This phenomenon could be attributed to the formation of a gel-like polymeric layer and the electrochemical

activation of the composites [52]. In addition, its Coulombic efficiency reached ~98 % after the 3<sup>rd</sup> cycle and exceeded 99 % after 100 cycles, indicating that efficient Li<sup>+</sup> insertion and extraction occur in the MHPC composites. The MoS<sub>2</sub>/C composite exhibited good cycling stability but had a relatively low capacity of only ~ 668 mA h g<sup>-1</sup> after 100 cycles because of its low surface area and dense micro-structure. In contrast, the bare MoS<sub>2</sub> electrode showed continuous and rapid capacity decay during cycling. Indeed, after 100 cycles, the bare MoS<sub>2</sub> electrode delivered only 168 mA g h<sup>-1</sup>.

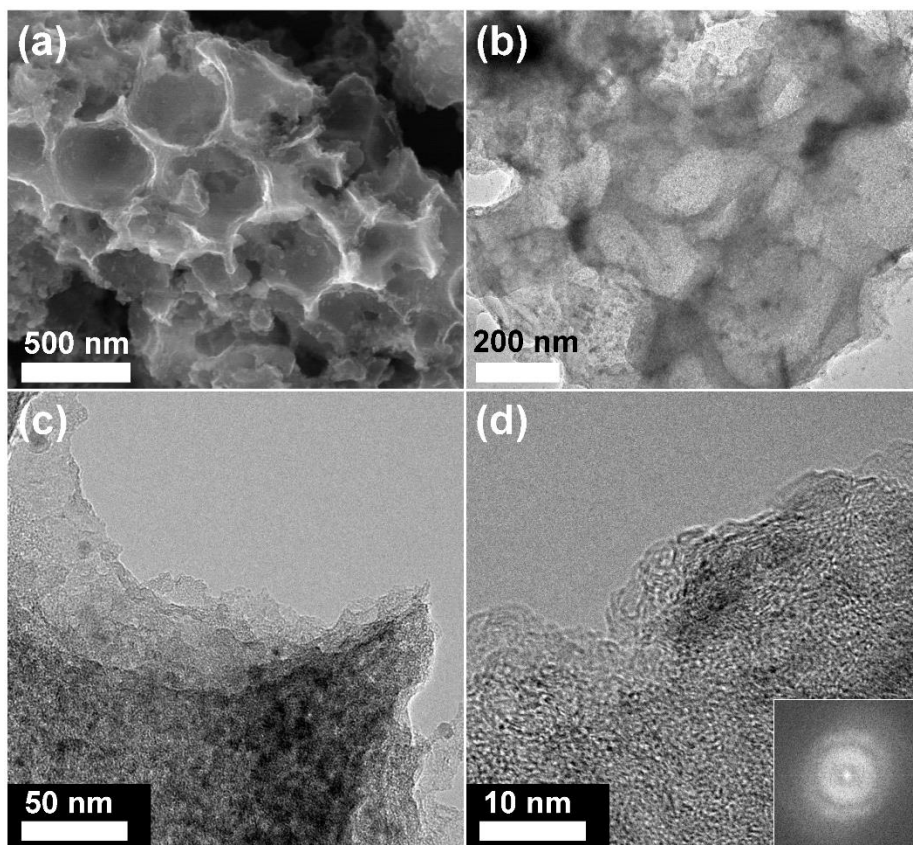


**Figure 2.16.** (a) SEM, (b) TEM, (c, d) HR-TEM images and FFT pattern (inset) of the cycled MHPC-0.1 electrode in LIBs test

**Table 2.2.** Comparison of the electrochemical performance of some related composite materials for LIBs in the literature

Sample	Specific discharge capacity	Current density	Voltage windows	Reference
<b>MHPC</b>	<b>496 mA h g<sup>-1</sup></b>	<b>10 A g<sup>-1</sup></b>	<b>0.01-3.0 V</b>	<b>Our work</b>
MoS <sub>2</sub> /Carbon nanosheets	280 mA h g <sup>-1</sup>	10 A g <sup>-1</sup>	0.005-3.0V	[40]
3D radially oriented MoS <sub>2</sub> nanospheres	354 mA h g <sup>-1</sup>	2 A g <sup>-1</sup>	0.01-3.0 V	[20]
CMK-3/MoS <sub>2</sub> composites	380 mA h g <sup>-1</sup>	1 A g <sup>-1</sup>	0.005-3.0 V	[52]
3D hierarchical MoS <sub>2</sub> /C	511 mA h g <sup>-1</sup>	1 A g <sup>-1</sup>	0.005-3.0 V	[44]
MoS <sub>2</sub> nanocages	680 mA h g <sup>-1</sup>	1 A g <sup>-1</sup>	0.005-3.0 V	[19]

To investigate the rate capabilities of MoS<sub>2</sub>/C, bare MoS<sub>2</sub>, and MHPC electrodes, we conducted electrochemical testing at varying current densities (**Figure 2.14d**). As the current densities increased from 0.1 to 0.2, 0.5, 1, 5, and 10 A g<sup>-1</sup>, the MHPC-0.1 electrode exhibited discharge capacities of 948, 864, 786, 725, 579, and 496 mA h g<sup>-1</sup>, respectively. Importantly, these capacities are much higher than those of the MoS<sub>2</sub>/C and bare MoS<sub>2</sub> electrodes and are also superior or comparable to those reported for previous MoS<sub>2</sub>-based composites (as shown in **Table 2.2**). Notably, when the current density decreased to 0.1 A g<sup>-1</sup>, the discharge capacity of the MHPC-0.1 electrode rose to 1020 mA h g<sup>-1</sup>, suggesting that the Li-storage performance of the MHPC composites is not degraded by high current density. Inspired by this material's excellent cycle stability and rate capability, the long-term cycling performance of the MHPC-0.1 electrode was also confirmed at a high current of 1 A g<sup>-1</sup> for 300 cycles (**Figure 2.14e**). Very surprisingly, this electrode delivered a specific discharge capacity of 732 mA h g<sup>-1</sup> after 300 charge/discharge cycles, confirming that it has high-rate cycling capability over the long term. According to the cycling curve, this capacity increase primarily occurs during the initial 200 cycles; subsequently, the capacity remains stable at a value of ~ 730 mA h g<sup>-1</sup>. Furthermore, the Coulombic

efficiency during long-term cycling remains near 100 %. Meanwhile, as shown in **Figure 2.16**, the porous structures of the electrodes are unbroken even after 300 cycles at a current density of  $1 \text{ A g}^{-1}$ , indicating the excellent stability of the HPMC composite electrodes because of their highly flexible and robust properties.

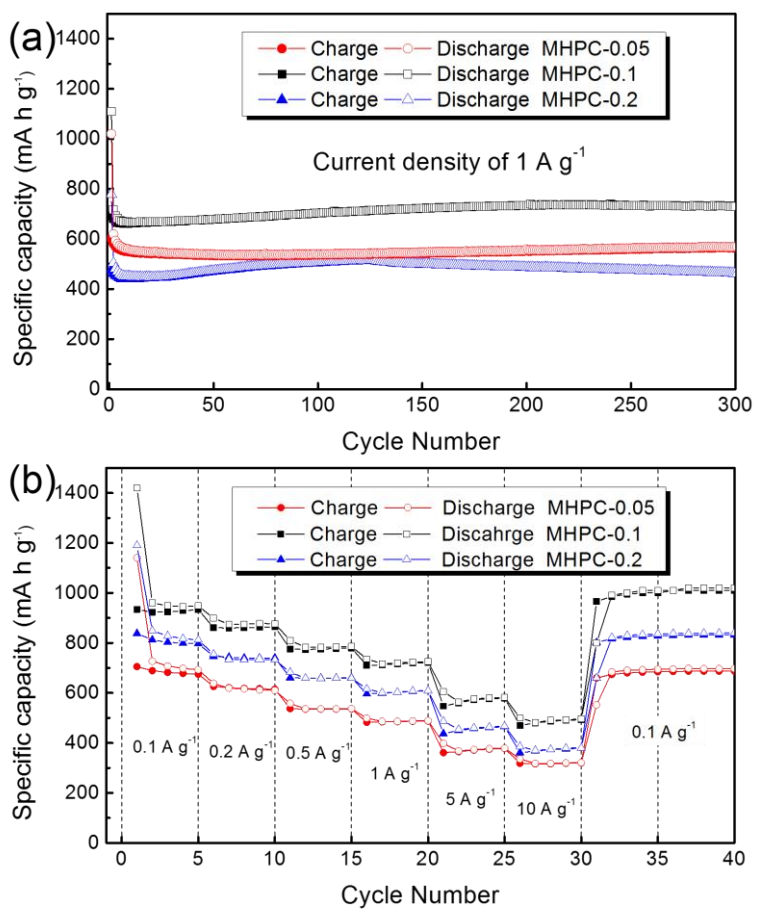


**Figure 2.17.** Electrochemical performance of MHPC-0.05, 0.1 and 0.2 for LIBs (a) Long-term cycling performance at a current density of  $1 \text{ A g}^{-1}$  and (b) rate capability.

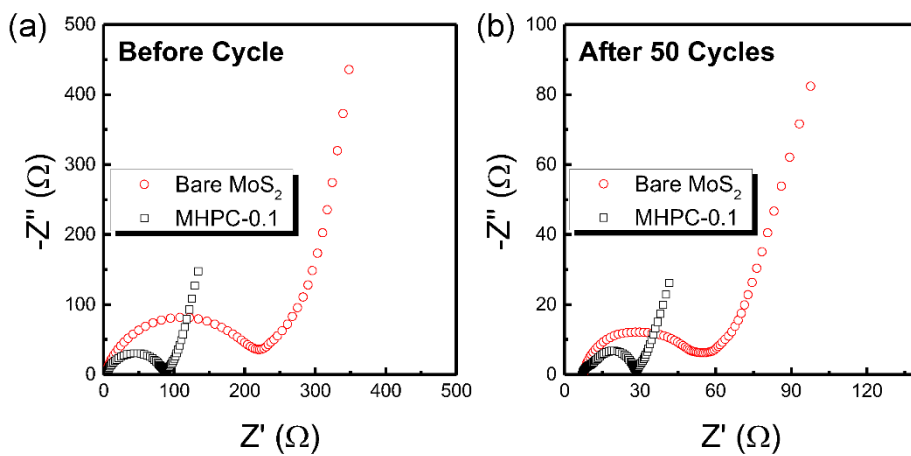


**Figure 2.18.** Electrochemical impedance spectra of MHPC-0.1 and bare MoS<sub>2</sub> electrodes in LIBs (a) before cycling and (b) after 50 cycling.

To further study the effect of the initial ATTM/OA ratio on the electrochemical performance, MHPC-0.05 and 0.2 were evaluated at a current density of  $1 \text{ A g}^{-1}$  for 300 cycles (**Figure 2.17a**). The MHPC-0.05 electrode exhibited good cycling stability but a low capacity of  $568 \text{ mA h g}^{-1}$  after 300 cycles. This result may be attributed to its relative large carbon content. In contrast, MHPC-0.2 showed the lowest capacity values among the MHPC composites tested, possibly because of its poor electrical conductivity, which is related to its relatively high content of  $\text{MoS}_2$ . However, in the rate capability test, the MHPC-0.2 composite had higher capacity values than MHPC-0.05, and it can be assumed that the initial charge/discharge process at a low current density improved the electrochemical performance of the MHPC-0.2 composite (**Figure 2.17b**).

**Figure 2.18** shows the EIS data of MHPC-0.1 and bare  $\text{MoS}_2$  electrodes before cycling and after 50 cycling at  $100 \text{ mA g}^{-1}$ , which is closely related to the stability of electrodes. The Nyquist plots exhibit semicircles in the medium frequency region, which is assigned to the charge-transfer resistance ( $R_{ct}$ ) and a line inclined to the real axis in the low frequency region, which corresponds to the ion diffusion process within the electrodes. The semicircle diameters for MHPC-0.1 electrode are significantly smaller than those of bare  $\text{MoS}_2$  electrode before and after cycling, indicating enhanced lithium and electron ion transport of MHPC-0.1 electrode.

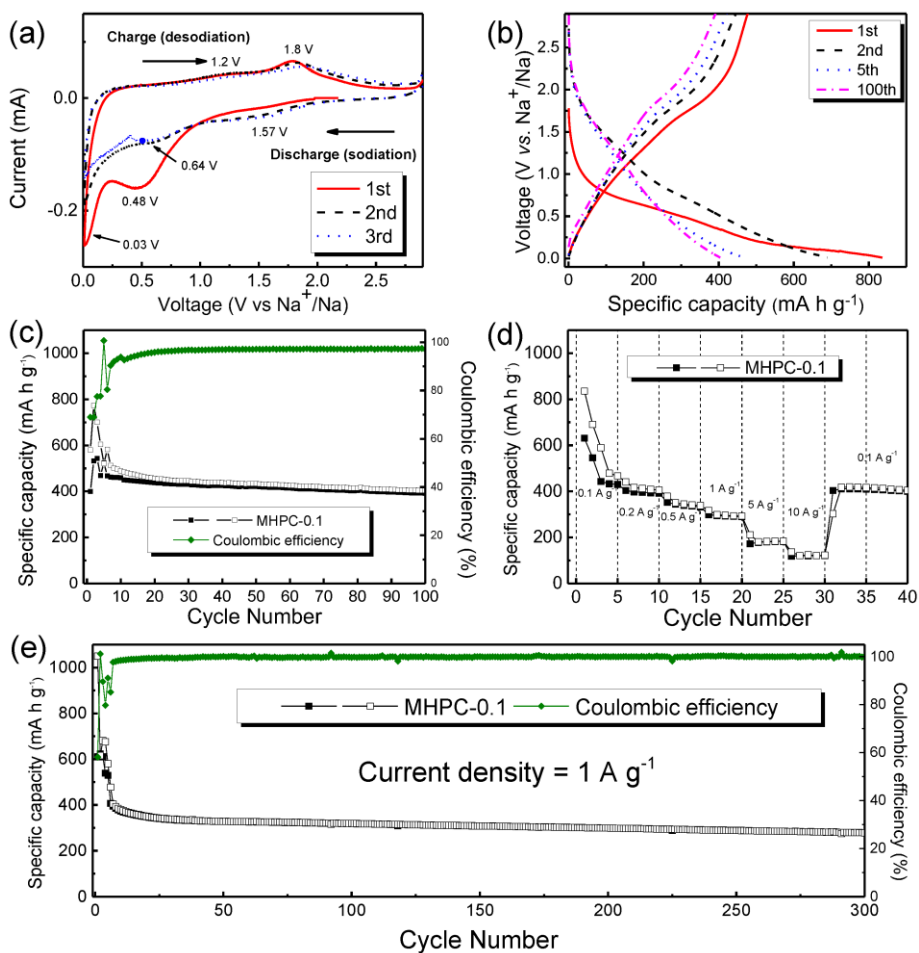


**Figure 2.19.** Electrochemical performance of MHPC-0.1 used in SIBs. (a) CVs at a scanning rate of 0.2 mV s<sup>-1</sup>. (b) Galvanostatic discharge/charge profiles at 0.1 A g<sup>-1</sup>. (c) Cycling and (d) rate capability performance of the electrodes. (e) Long-term cycling performance at a current density of 1 A g<sup>-1</sup>.

**Table 2.3.** Comparison of the electrochemical performance of some related composite materials for SIBs in the literature.

Sample	Specific discharge capacity	Current density	Voltage windows	Reference
<b>MHPC</b>	<b>293 mA h g<sup>-1</sup></b>	<b>1 A g<sup>-1</sup></b>	<b>0.01-2.9 V</b>	<b>Our work</b>
MoS <sub>2</sub> /graphene paper	173 mA h g <sup>-1</sup>	0.2 A g <sup>-1</sup>	0.1-2.25 V	[54]
MoS <sub>2</sub> /graphene synthesized via microwave	214 mA h g <sup>-1</sup>	1 A g <sup>-1</sup>	0.005-2.5 V	[55]
Liquid exfoliated MoS <sub>2</sub>	120 mA h g <sup>-1</sup>	0.8 A g <sup>-1</sup>	0.4-2.5 V	[26]
MoS <sub>2</sub> /CNT	328 mA h g <sup>-1</sup>	0.5 A g <sup>-1</sup>	0.001-2.5 V	[24]
MoS <sub>2</sub> /graphene	352 mA h g <sup>-1</sup>	0.64 A g <sup>-1</sup>	0.01-3.0 V	[56]

Furthermore, the Na-storage properties of the samples were determined using conditions similar to those used for the LIBs (**Figure 2.19**). In the CV of the first cycle, the MHPC-0.1 composite showed two reduction peaks at approximately 0.48 and 0.03 V and corresponding oxidation peaks at approximately 1.2 and 1.8 V. In the second cycle, we observe new reduction peaks at approximately 0.64 and 1.57 V; here, the peak located at 1.57 V can be attributed to Na<sup>+</sup> intercalation into the MoS<sub>2</sub> layer, whereas that at 0.64 V can be ascribed to the conversion reaction [53, 54] This mechanism is also confirmed by the charge/discharge profiles of the MHPC-0.1 composite. **Figure 2.19c** demonstrates the cycling performance of the MHPC-0.1 composite over 100 cycles at 0.1 A g<sup>-1</sup>. Although an unstable charge/discharge process occurred during the initial 5 cycles, the capacity values quickly stabilized within 10 cycles; this behavior is attributed to the poor electrochemical reaction kinetics of the Na ion compared to those of the Li ion.

The MHPC-0.1 composite delivered a high reversible discharge capacity of 404 mA h g<sup>-1</sup> after 100 cycles, which is approximately 85 % of the reversible capacity of the 10<sup>th</sup> cycle, and a Coulombic efficiency exceeding 96 % was estimated. Furthermore, MHPC-0.1 displayed excellent reversible capacities of 467, 406, 338, 293, 183, and 122 mA h

$\text{g}^{-1}$  at current densities of 0.1, 0.2, 0.5, 1.0, 5.0, and 10.0  $\text{A g}^{-1}$ , respectively. As in LIBs, the capacity of the MHPC-0.1 electrode rapidly returned to higher values when the current density was decreased to 0.1  $\text{A g}^{-1}$ , suggesting that the MHPC electrodes are also very suitable for high-rate SIBs. Accordingly, a long-term cycling test including 300 cycles at a current density of 1  $\text{A g}^{-1}$  was performed and revealed stable capacity values without rapid capacity fading (the discharge capacity was 280  $\text{mA h g}^{-1}$  at the 300<sup>th</sup> cycle).

Clearly, these MHPC composites' outstanding cycling stabilities and rate capabilities for both Li and Na storage are associated with their unique nanostructure, which provides the following advantages: 1) The conductive carbon nanosheets that tightly anchor the  $\text{MoS}_2$  nanosheets ensure the stable and fast transport of both ions and electrons, especially during high-rate cycling, thereby inhibiting the stacking of  $\text{MoS}_2$  nanosheets and significantly enhancing the rate cycling stability and capacity. Moreover, sandwiching the  $\text{MoS}_2$  nanosheets between carbon nanosheets minimizes their intrinsic volume expansion and stacking problems during the charge/discharge process. 2) The hierarchical carbon nanosheet architecture, which has a high surface area and interconnected networks, contributes substantially to the efficient and

fast 3D transport of ions and electrons deep into the electrode. 3) The 2D characters of the carbon and MoS<sub>2</sub> nanosheets provide short diffusion distances, facilitating efficient ion and electron transport and enhancing the rate performance and Coulombic efficiency.

## 2.4. Conclusion

In summary, we developed a facile and scalable solventless strategy for the synthesis of MHPC nanosheets as high-performance anode materials for LIBs and SIBs. OA, which has positively charged amine end groups, was introduced to serve as both a surfactant to inhibit the stacking of MoS<sub>2</sub> nanosheets and a carbon source to enhance the electrode's electrical conductivity. In addition, an inverse opal structured SiO<sub>2</sub> template was used to direct the growth of both the carbon and MoS<sub>2</sub> nanosheets, resulting in the formation of a hierarchical porous structure with interconnected networks. These unique features enhance the structural stability of the overall electrode and enable high rates of fast ion and electron transport deep into the electrode to access the active sites there. Consequently, this hierarchical porous architecture shows significantly improved capacity and excellent long-term cycling performance when used as an anode material for LIBs and SIBs, even at high rates. Indeed, the materials tested here delivered reversible capacities as large as 732 and 280 mA h g<sup>-1</sup> after 300 cycles at 1 A g<sup>-1</sup> in LIBs and SIBs, respectively. All of the results indicate that this MHPC composite has tremendous potential for applications in other fields,

including in catalysis, supercapacitors, and electronic devices. Furthermore, this solventless synthesis protocol can be readily extended to the construction of other metal-based materials incorporated in hierarchical porous carbon nanosheets for various applications.

## 2.5. References

- [1] J. B. Goodenough and K. S. Park, *J. Am. Chem. Soc.*, **2013**, 135, 1167.
- [2] V. Etacheri, R. Marom, R. Elazari, G. Salitra and D. Aurbach, *Energy Environ. Sci.*, **2011**, 4, 3243.
- [3] N. Yabuuchi, K. Kubota, M. Dahbi and S. Komaba, *Chem. Rev.*, **2014**, 114, 11636.
- [4] K. Kubota and S. Komaba, *J. Electrochem. Soc.*, **2015**, 162, A2538.
- [5] J. Y. Li, Y. Hou, X. F. Gao, D. S. Guan, Y. Y. Xie, J. H. Chen and C. Yuan, *Nano Energy*, **2015**, 16, 10.
- [6] X. L. Wang, G. Li, M. H. Seo, F. M. Hassan, M. A. Hoque and Z. W. Chen, *Adv. Energy Mater.*, **2015**, 5.
- [7] X. F. Wang, X. Shen, Z. X. Wang, R. C. Yu and L. Q. Chen, *ACS Nano*, **2014**, 8, 11394.
- [8] Y. X. Wang, K. H. Seng, S. L. Chou, J. Z. Wang, Z. P. Guo, D. Wexler, H. K. Liu and S. X. Dou, *Chem. Commun.*, **2014**, 50, 10730.
- [9] J. Z. Wang, L. Lu, M. Lotya, J. N. Coleman, S. L. Chou, H. K. Liu, A. I. Minett and J. Chen, *Adv. Energy Mater.*, **2013**, 3, 798.

- [10] F. Y. Xiong, Z. Y. Cai, L. B. Qu, P. F. Zhang, Z. F. Yuan, O. K. Asare, W. W. Xu, C. Lin and L. Q. Mai, *ACS Appl. Mater. Interfaces*, **2015**, 7, 12625.
- [11] S. H. Choi, Y. N. Ko, J. K. Lee and Y. C. Kang, *Adv. Funct. Mater.*, **2015**, 25, 1780.
- [12] Y. J. Gong, S. B. Yang, L. Zhan, L. L. Ma, R. Vajtai and P. M. Ajayan, *Adv. Funct. Mater.*, **2014**, 24, 125.
- [13] C. N. R. Rao, A. K. Sood, K. S. Subrahmanyam and A. Govindaraj, *Angew. Chem. Int. Ed.*, **2009**, 48, 7752.
- [14] K. Chang, D. S. Geng, X. F. Li, J. L. Yang, Y. J. Tang, M. Cai, R. Y. Li and X. L. Sun, *Adv. Energy Mater.*, **2013**, 3, 839.
- [15] X. Huang, Z. Y. Zeng and H. Zhang, *Chem. Soc. Rev.*, **2013**, 42, 1934.
- [16] C. L. Tan and H. Zhang, *Chem. Soc. Rev.*, **2015**, 44, 2713.
- [17] S. K. Park, S. H. Yu, S. Woo, J. Ha, J. Shin, Y. E. Sung and Y. Piao, *Crystengcomm*, **2012**, 14, 8323.
- [18] M. W. Xu, F. L. Yi, Y. B. Niu, J. L. Xie, J. K. Hou, S. G. Liu, W. H. Hu, Y. T. Li and C. M. Li, *J. Mater. Chem. A*, **2015**, 3, 9932.
- [19] X. X. Zuo, K. Chang, J. Zhao, Z. Z. Xie, H. W. Tang, B. Li and Z. R. Chang, *J. Mater. Chem. A*, **2016**, 4, 51.

- [20] S. P. Zhang, B. V. R. Chowdari, Z. Y. Wen, J. Jin and J. H. Yang, *ACS Nano*, **2015**, 9, 12464.
- [21] H. Hwang, H. Kim and J. Cho, *Nano Lett.*, **2011**, 11, 4826.
- [22] H. Li, W. J. Li, L. Ma, W. X. Chen and J. M. Wang, *J. Alloy Compd.*, **2009**, 471, 442.
- [23] S. K. Park, S. H. Yu, S. Woo, B. Quan, D. C. Lee, M. K. Kim, Y. E. Sung and Y. Piao, *Dalton Trans.*, **2013**, 42, 2399.
- [24] S. Zhang, X. B. Yu, H. L. Yu, Y. J. Chen, P. Gao, C. Y. Li and C. L. Zhu, *ACS Appl. Mater. Interfaces*, **2014**, 6, 21880.
- [25] C. B. Zhu, X. K. Mu, P. A. van Aken, Y. Yu and J. Maier, *Angew. Chem. Int. Ed.*, **2014**, 53, 2152.
- [26] G. S. Bang, K. W. Nam, J. Y. Kim, J. Shin, J. W. Choi and S. Y. Choi, *ACS Appl. Mater. Interfaces*, **2014**, 6, 7084.
- [27] H. Jiang, D. Y. Ren, H. F. Wang, Y. J. Hu, S. J. Guo, H. Y. Yuan, P. J. Hu, L. Zhang and C. Z. Li, *Adv. Mater.*, **2015**, 27, 3687.
- [28] G. C. Huang, T. Chen, W. X. Chen, Z. Wang, K. Chang, L. Ma, F. H. Huang, D. Y. Chen and J. Y. Lee, *Small*, **2013**, 9, 3693.
- [29] G. Liu, Y. Y. Feng, Y. Li, M. M. Qin, H. R. An, W. P. Hu and W. Feng, *Part. Part. Syst. Char.*, **2015**, 32, 489.
- [30] X. H. Cao, Y. M. Shi, W. H. Shi, X. H. Rui, Q. Y. Yan, J. Kong and

- H. Zhang, *Small*, **2013**, 9, 3433.
- [31] K. M. McCreary, A. T. Hanbicki, J. T. Robinson, E. Cobas, J. C. Culbertson, A. L. Friedman, G. G. Jernigan and B. T. Jonker, *Adv. Funct. Mater.*, **2014**, 24, 6449.
- [32] C. Altavilla, M. Sarno and P. Ciambelli, *Chem. Mater.*, **2011**, 23, 3879.
- [33] Z. Hu, L. X. Wang, K. Zhang, J. B. Wang, F. Y. Cheng, Z. L. Tao and J. Chen, *Angew. Chem. Int. Ed.*, **2014**, 53, 12794.
- [34] B. J. Guo, K. Yu, H. L. Song, H. L. Li, Y. H. Tan, H. Fu, C. Li, X. Lei and Z. Q. Zhu, *Nanoscale*, **2016**, 8, 420.
- [35] F. M. Wang, J. S. Li, F. Wang, T. A. Shifa, Z. Z. Cheng, Z. X. Wang, K. Xu, X. Y. Zhan, Q. S. Wang, Y. Huang, C. Jiang and J. He, *Adv. Funct. Mater.*, **2015**, 25, 6077.
- [36] X. M. Geng, W. Wu, N. Li, W. W. Sun, J. Armstrong, A. Al-hilo, M. Brozak, J. B. Cui and T. P. Chen, *Adv. Funct. Mater.*, **2014**, 24, 6123.
- [37] X. B. Fan, P. T. Xu, D. K. Zhou, Y. F. Sun, Y. G. C. Li, M. A. T. Nguyen, M. Terrones and T. E. Mallouk, *Nano Lett.*, **2015**, 15, 5956.
- [38] Y. F. Li, Y. L. Liang, F. C. R. Hernandez, H. D. Yoo, Q. Y. An and

- Y. Yao, *Nano Energy*, **2015**, 15, 453.
- [39] L. Ma, J. B. Ye, W. X. Chen, J. M. Wang, R. Liu and J. Y. Lee, *ChemElectroChem*, **2015**, 2, 538.
- [40] J. W. Zhou, J. Qin, X. Zhang, C. S. Shi, E. Z. Liu, J. J. Li, N. Q. Zhao and C. N. He, *ACS Nano*, **2015**, 9, 3837.
- [41] C. B. Zhu, X. K. Mu, P. A. van Aken, J. Maier and Y. Yu, *Adv. Energy Mater.*, **2015**, 5.
- [42] K. Chang, W. X. Chen, L. Ma, H. Li, H. Li, F. H. Huang, Z. D. Xu, Q. B. Zhang and J. Y. Lee, *J. Mater. Chem.*, **2011**, 21, 6251.
- [43] K. Chang and W. X. Chen, *J. Mater. Chem.*, **2011**, 21, 17175.
- [44] L. R. Hu, Y. M. Ren, H. X. Yang and Q. Xu, *ACS Appl. Mater. Interfaces*, **2014**, 6, 14644.
- [45] H. Liu, D. W. Su, R. F. Zhou, B. Sun, G. X. Wang and S. Z. Qiao, *Adv. Energy Mater.*, **2012**, 2, 970.
- [46] Y. M. Sun, X. L. Hu, J. C. Yu, Q. Li, W. Luo, L. X. Yuan, W. X. Zhang and Y. H. Huang, *Energy Environ. Sci.*, **2011**, 4, 2870.
- [47] Y. M. Sun, X. L. Hu, W. Luo and Y. H. Huang, *ACS Nano*, **2011**, 5, 7100.
- [48] Y. M. Shi, Y. Wang, J. I. Wong, A. Y. S. Tan, C. L. Hsu, L. J. Li, Y. C. Lu and H. Y. Yang, *Sci. Rep.*, **2013**, 3.

- [49] S. K. Das, R. Mallavajula, N. Jayaprakash and L. A. Archer, *J. Mater. Chem.*, **2012**, 22, 12988.
- [50] S. K. Park, C. Y. Seong and Y. Piao, *Electrochim. Acta*, **2015**, 176, 1182.
- [51] S. K. Park, S. Woo, S. Lee, C. Y. Seong and Y. Piao, *RSC Adv.*, **2015**, 5, 52687.
- [52] X. Xu, Z. Y. Fan, X. Y. Yu, S. J. Ding, D. M. Yu and X. W. Lou, *Adv. Energy Mater.*, **2014**, 4, 1400902.
- [53] J. Park, J. S. Kim, J. W. Park, T. H. Nam, K. W. Kim, J. H. Ahn, G. Wang and H. J. Ahn, *Electrochim. Acta*, **2013**, 92, 427.
- [54] L. David, R. Bhandavat and G. Singh, *ACS Nano*, **2014**, 8, 1759.
- [55] W. Qin, T. Q. Chen, L. K. Pan, L. Y. Niu, B. W. Hu, D. S. Li, J. L. Li and Z. Sun, *Electrochim. Acta*, **2015**, 153, 55.
- [56] X. Q. Xie, Z. M. Ao, D. W. Su, J. Q. Zhang and G. X. Wang, *Adv. Funct. Mater.*, **2015**, 25, 1393.

# **Chapter 3. Uniform Carbon Nanocapsule/Graphene Nanosheet Hybrids as Cathode Reservoirs for Lithium-Sulfur Batteries**

## **3.1. Introduction**

Among the known next-generation battery systems, rechargeable lithium-sulfur (Li-S) batteries have earned distinction due to their high specific energy density ( $2600 \text{ W h kg}^{-1}$ ), environmental friendliness, and the natural abundance of sulfur [1-3]. Despite these considerable advantages, there are two major drawbacks of using sulfur: its electronic insulating nature and the rapid capacity fading caused by the high solubility of the intermediate products  $\text{Li}_2\text{S}_x$  ( $2 < x \leq 8$ ) in organic electrolyte solutions [4-8]. In addition, large volume expansion of the sulfur particles during cycling can result in structural collapse of the electrode [9, 10]. These issues greatly restrict the practical applications of Li-S batteries. A reasonable strategy to overcome these problems is to utilize

conductive carbon materials as effective hosts for sulfur loading. Such carbon materials include carbon nanotubes [11-13], graphene [14-16], hollow carbon spheres [9, 17, 18], and porous carbon [19-21] that can improve the electrical conductivity of the active materials and minimize the dissolution of lithium polysulfide into the electrolyte.

Among these carbon materials, graphene has been intensively studied as a matrix for the electrode of Li-S batteries due to its high specific surface area, excellent electrical conductivity, and good mechanical strength [22-25]. However, the ability of graphene as a host material to effectively confine the intermediate products in the cathodes during cycling is limited due to its open structure. Thus, polysulfides can still easily diffuse out of the cathodes, which leads to gradual capacity decay [26, 27].

As a partial solution, considerable effort has been made to incorporate other carbon materials that can confine sulfur into the graphene structure, such as carbon nanocapsules [28, 29], mesoporous carbon [30, 31], and conducting polymers [32, 33]. Specifically, the combination of carbon nanocapsules (CNCs) with graphene has been considered as an interesting host because this

composite may offer improved electrical conductivity as well as confine the sulfur or polysulfides under the carbon shell [28, 29]. Liu *et al.* synthesized three-dimensional (3D) nanostructure of graphene-hollow carbon spheres with a diameter of 180 nm as the sulfur host via a hydrothermal self-assembly method. The as-prepared cathode delivers high capacity and excellent rate performance [28]. However, preparation of CNC/graphene composites currently requires complicated and time-consuming processes, resulting in a low-yield and higher cost. Furthermore, the synthesis of small ( $< 50$  nm) and uniformly sized carbon nanocapsule-based composites with short ion/electron transfer distances and stable active sites in the structure is still challenging.

Herein, we propose a facile strategy for synthesis of monodisperse carbon nanocapsule anchored on graphene nanosheet (MCNC/G) composites as effective host materials to confine sulfur for Li-S batteries (**Figure 3.1**). Impregnation of elemental melted sulfur into the unique pore structure of MCNC/G imparts significantly improved electrochemical performance to the MCNC/G-sulfur (MCNC/G-S) composite compared to that of bare graphene nanosheets.

## **3.2. Experimental Section**

### **3.2.1. Chemicals**

Iron(III) acetylacetonate ( $\text{Fe}(\text{acac})_3$ ) and oleic acid was purchased from Aldrich Chemical Co. Sulfur powder was purchased from SAMCHUN Chemical Co.

### **3.2.2. Characterization methods**

X-ray diffraction (XRD) patterns were obtained using a diffractometer (D8-advances) with a  $\text{Cu K}\alpha$  radiation source ( $\lambda=0.154$  nm) from 20 to 70° at a scan rate of 2°  $\text{min}^{-1}$ . The structure and morphology of the composites was investigated by field-emission scanning electron microscopy (FE-SEM, Hitachi S-4800) and high-resolution transmission electron microscopy (TEM, JEOL JEM-2010) equipped with an energy-dispersive X-ray (EDX) spectrometer. Thermal gravimetric analysis (TGA) was performed using a thermal analyzer (TGA/DSC 1, Mettler Toledo) at a heating rate of 10 °C  $\text{min}^{-1}$  under an  $\text{N}_2$  atmosphere. The Brunauer-Emmett-Teller (BET) specific surface area and pore size distribution of the composites were measured by  $\text{N}_2$  adsorption/desorption using an adsorption analyzer (BELSORP-mini II).

### **3.2.3. Preparation of graphene**

Graphene oxide (GO) was synthesized from commercial graphite powder (Aldrich, < 20 micron) by a modified Hummers method [Ref]. Graphene was prepared by a thermal expansion of the GO under vacuum condition. In a typical process, the GO powder was put into a two-neck round-bottom flask and then it was connected to a high vacuum pump. After creating a vacuum state, the flask was rapidly heated by a heating mantle. At about 190 °C, a dramatic expansion of GO can be observed. To reduce the GO completely, the black powder was kept at 300 °C for 3 h.

### **3.2.4. Preparation of carbon coated monodisperse iron oxide/graphene (IO@C/G) composite**

In a typical synthesis, 0.7g of Fe(acac)<sub>3</sub> was solventlessly mixed with 1.7 ml of OA. These red-colored iron–oleate precursors were then mixed well with 0.13 g of as-prepared graphene powder in mortar with a pestle. The mixture was heated to 600 °C with the heating rate of 10 °C min<sup>-1</sup> under an Ar atmosphere and then kept at that temperature for 3 h.

### **3.2.5. Preparation of monodisperse carbon nanocapsule/G (MCNC/G) composite**

To obtain MCNC/G composite, monodisperse iron oxide nanoparticles in IO@C/G composite were etched with 3 M hydrochloric acid (HCl) for 5 hrs. After washing with DI water and EtOH, the obtained MCNC/G powder was thermally treated at 800 °C for 3h to improve the conductivity of carbon.

### **3.2.6 Preparation of sulfur-loaded MCNC/G (MCNC/G-S) composite**

The sulfur loading into MCNC/G composite were implemented by the general melting-diffusion method. In a typical process, the as-prepared MCNC/G powder was ground with sulfur (SAMCHUN, 60 wt % of total mass). The mixture was then transferred to alumina boat and heated to 155 °C in a tube furnace for 18 hrs under Ar atmosphere.

### **3.2.7. Electrode preparation**

The electrodes consisted of MCNC/G-S as an active material, conducting agent (Acetylene black), and polymer binder (Polyvinylidene flouroide, PVdF) in a ratio of 7:2:1 (wt%), it was homogenized well using a ball-milling (Mini-Mill PULVERISETTE 23, FRITSCH) at 40 instruction per second for 30 min. Then, the homogeneous slurry was casted on pure

aluminum foil by using doctor blade with the thickness of 100  $\mu\text{m}$ . The electrodes were dried in the vacuum oven at 60  $^{\circ}\text{C}$  during the overnight, and were punched for diameter of 11 mm. The mass loading of active material is averagely between 0.6 and 0.8  $\text{mg cm}^{-2}$ .

### **3.2.8 Electrochemical characterization**

Electrochemical performances were conducted by using a CR2016-type coin cell. The cells were fabricated in Ar-filled glove box ( $\text{O}_2$  and  $\text{H}_2\text{O}$  contents below 0.1 ppm). Commercial polymer separator (Celgard 2400) and 1.0 M bis(trifluoromethane)sulfonimide lithium salt (LiTFSI) and 0.3 M  $\text{LiNO}_3$  in a 1:1 by volume mixture of 1,3-dioxolane (DOL) and dimethoxymethane (DME) as the electrolyte was used. Lithium metal foil was used as an anode electrode and this cell was measured for a half-cell. All electrochemical measurements were carried out at a room temperature of 25  $^{\circ}\text{C}$ . For Galvanostatic charge/discharge measurement (WBCS3000s cycler, WonATech, Korea) was used in a voltage window of 1.7 and 2.8 V vs.  $\text{Li/Li}^+$ .

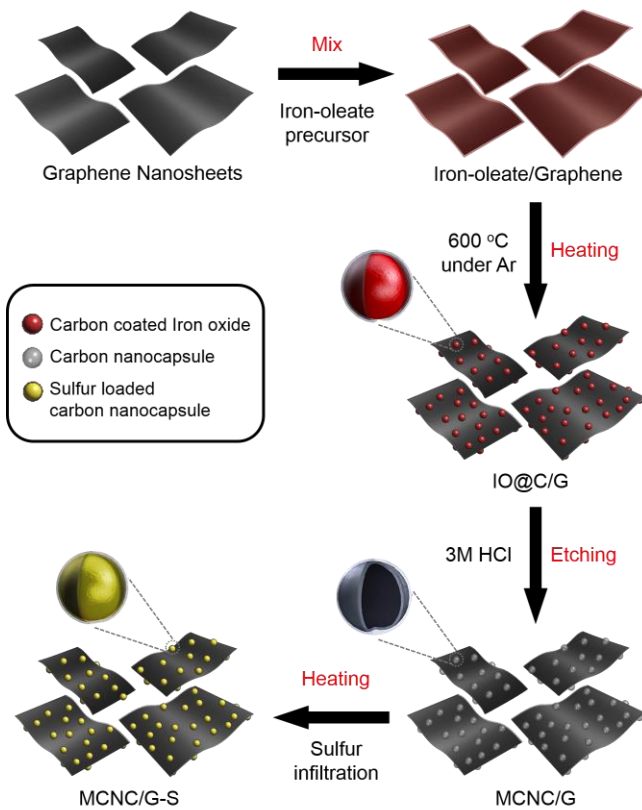


**Figure 3.1.** Schematic illustration of preparation of the MCNC/G and MCNC/G-S composites.

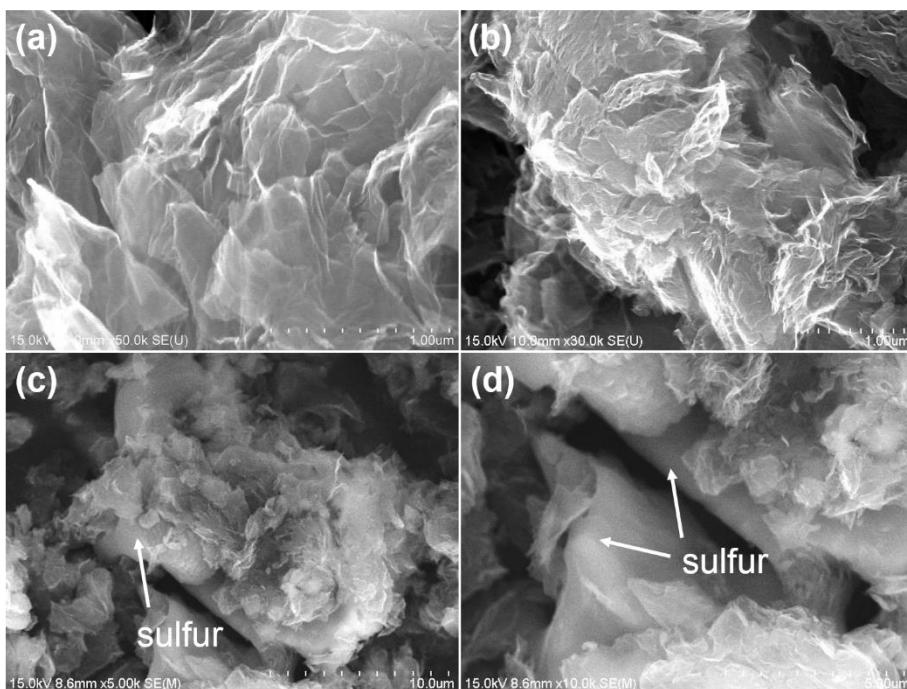


**Figure 3.2.** SEM images of (a, b) bare graphene nanosheets and (c, d) G-S composite.

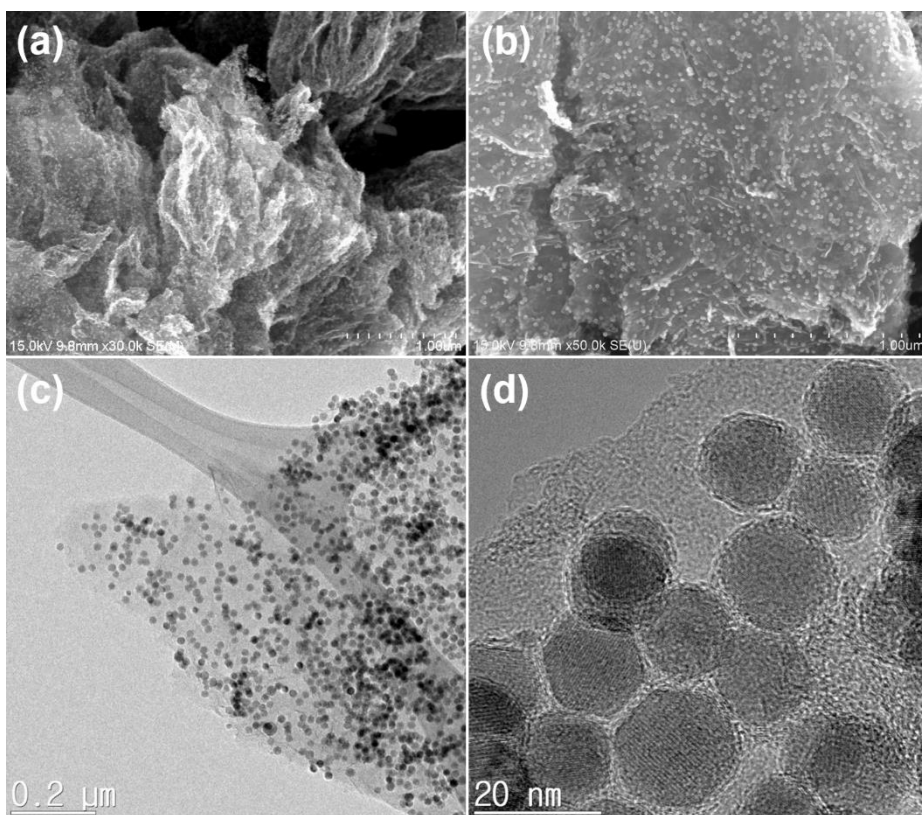


**Figure 3.3.** (a, b) SEM images and (c, d) TEM images of IO@C/G composites.



**Figure 3.4.** Large scale synthesis of MCNC/G composites (using 0.14 g of graphene).

### 3.3. Results and Discussion

In the typical process, the graphene nanosheets were first prepared via vacuum-assisted thermal reduction of graphene oxide (**Figure 3.2a and b**). Then The graphene nanosheets were combined with the viscous iron-oleate precursor prepared by simply mixing oleic acid and iron acetylacetonate, followed by heating at 600 °C for 3 hrs under Ar. During this process, monodisperse carbon-coated iron oxide nanoparticles were formed on the graphene nanosheets via thermal decomposition of the iron-oleate precursor (IO@C/G, **Figure 3.3**) [34]. Finally, the IO@C/G composite was subjected to acid etching to obtain the MCNC/G. The obtained MCNC/G composite was infiltrated with sulfur using the melt-infusion method to obtain the MCNC/G-S composite. Because this facile strategy was implemented under solvent-free conditions, it is very economical, easily controllable, and suitable for scalable production (**Figure 3.4**).

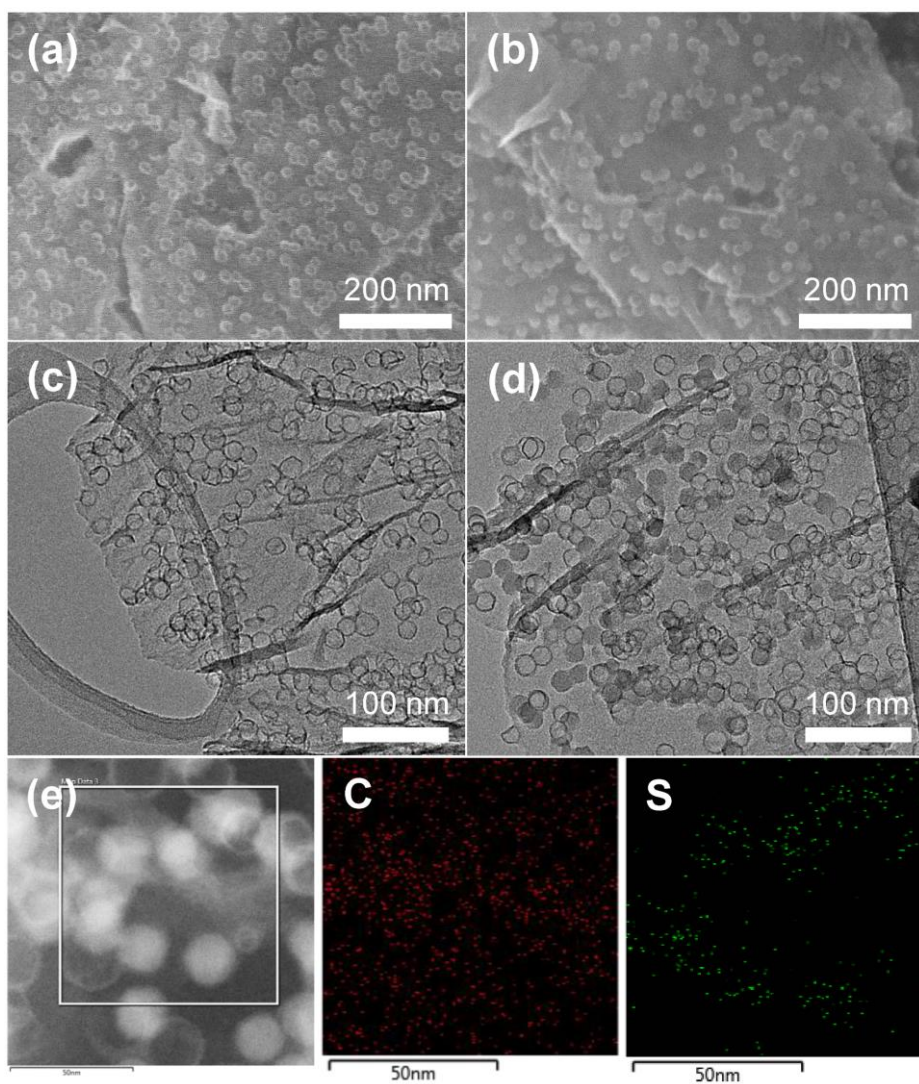


**Figure 3.5.** SEM images of (a) MCNC/G and (b) MCNC/G-S. TEM images of (c) MCNC/G and (d) MCNC/G-S. (e) Dark field image and the corresponding C and S element mapping of MCNC/G-S.

The structures and morphologies of the MCNC/G and MCNC/G-S composites were characterized by scanning and transmission electron microscopy (SEM and TEM, **Figure 3.5**). As shown in Fig. 1a and c, CNCs with a uniform diameter of about 20 nm and shell thickness of 2 nm were densely deposited on the surface of the graphene nanosheets. Even though the MCNC/G composite was subjected to high temperature annealing, no CNC aggregates were detected, indicating that these composites have a very stable structure. Interestingly, after sulfur infusion, the void space inside the CNCs was filled with sulfur species of the same size as the CNCs (**Figure 3.5b and d**) and some sulfur element was deposited on the surface of graphene. This result provides clear evidence that the elemental melted sulfur was well infiltrated into the CNCs due to the capillarity interaction and excellent wettability with carbon [28]. In contrast, the SEM images of the bare graphene nanosheet/sulfur (G-S) composites show some agglomerated sulfur particles of several micrometer (**Figure 3.2c and d**). These morphological differences reveal that the unique structure of the MCNC/G composites successfully inhibits aggregation of sulfur during the melting process. The partially empty voids in the TEM

image of the MCNC/G-S composite are attributed to sulfur sublimed by the electron beam heating effect under the ultra-high vacuum. The dark field image and the corresponding carbon and sulfur mapping of MCNS/G-S provide further evidence that sulfur was uniformly confined within the CNCs with a small fraction on the surface of the graphene sheets.

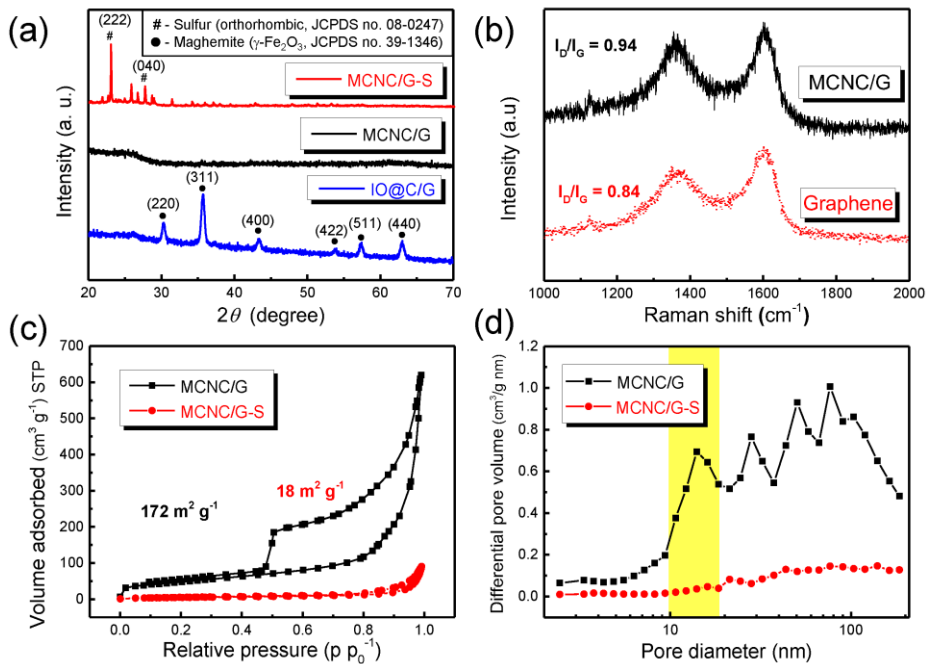


**Figure 3.6.** (a) XRD patterns of IO@C/G, MCNC/G, and MCNC/G-S. (b) Raman spectra of MCNC/G and bare graphene; (c) nitrogen adsorption-desorption isotherms, and (d) pore-size distributions of MCNC/G and MCNC/G-S.

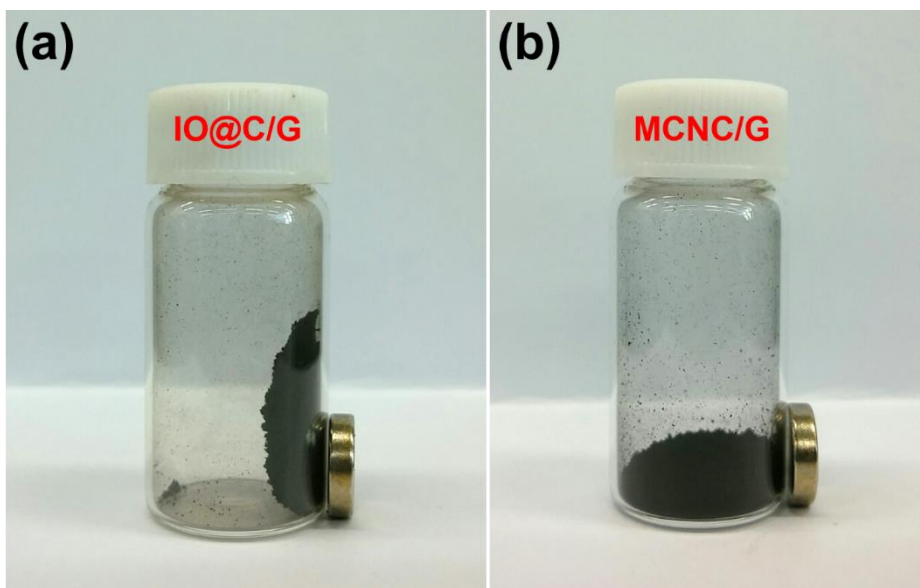


**Figure 3.7.** Pictures in (a, b) show that powder of MCNC/G was not attracted by a magnet after acid etching of IO@C/G.

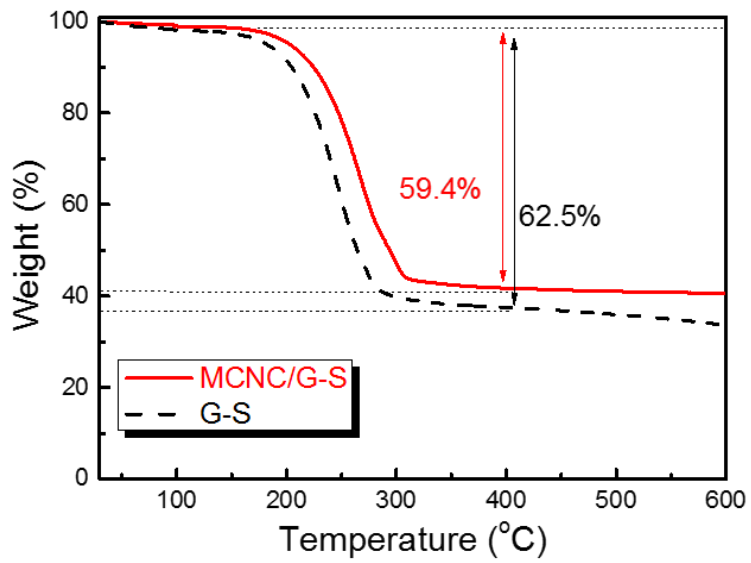


**Figure 3.8.** TGA curves of MCNC/G-S and G-S

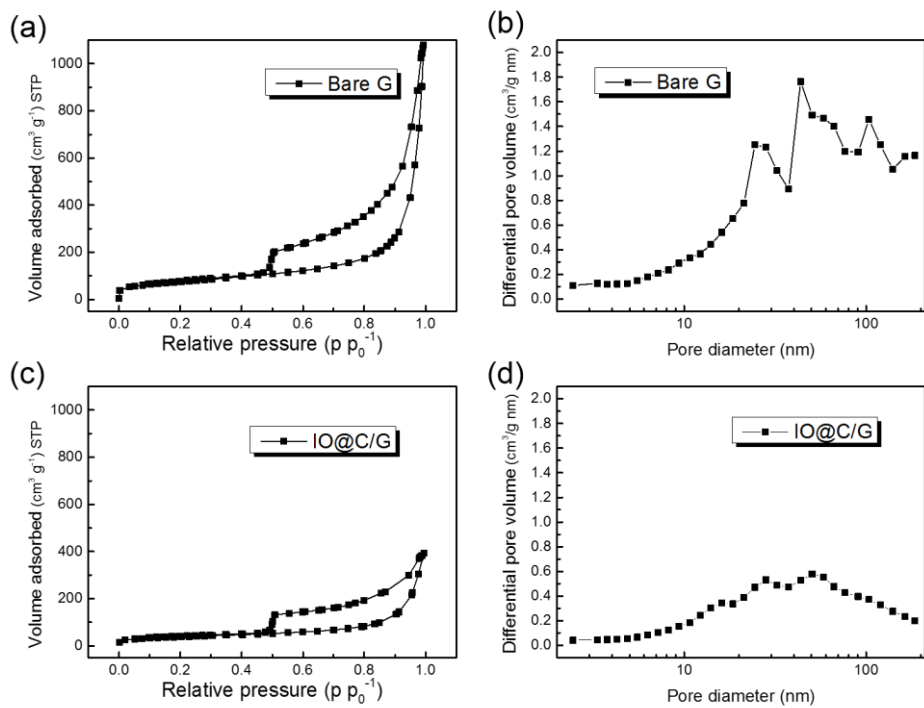


**Figure 3.9.** (a, c) The N<sub>2</sub>-sorption isotherms and (b, d) the pore size distribution curves of bare graphene nanosheets and IO@C/G, respectively.

The X-ray diffraction (XRD) patterns of the samples are shown in **Figure 3.6a**. After the etching process, no peaks attributed to the maghemite phase ( $\gamma\text{-Fe}_2\text{O}_3$ , JCPDS No. 39-1346) were detected in the XRD pattern of MCNC/G, suggesting that the iron oxide nanoparticles were completely removed. Further, the MCNC/G powder was not attracted by a magnet, unlike the IO@C/G composite (**Figure 3.7**). The XRD pattern of the MCNC/G-S composite is the same as that of pure elemental sulfur (orthorhombic, JCPDS No. 08-0247), indicating that the process of sulfur infiltration into the MCNC/G composite does not induce any crystal structure changes. Thermogravimetric analysis (TGA; **Figure 3.8**) indicated that the sulfur content in the MCNC/G-S composite was about 60 wt%.

Raman scattering is substantially sensitive to the electronic structure of materials and an effective technique for characterizing crystallinity of carbon [35, 36]. In **Figure 3.6b**, Raman spectra display obvious two broad peaks located at ca. 1360 and 1600  $\text{cm}^{-1}$  which are related to D and G bands of graphitic materials with defects [37]. The D band is assigned to the vibration of C atoms with dangling bonds of the graphite with defects whereas the G

band is attributed to the vibration of  $sp^2$ -bonded C atoms (C=C, typical graphite bonds) [38, 39]. It is noteworthy that the G band of both materials are shifted to higher wavenumber compared with that of bare graphite crystals ( $1580\text{ cm}^{-1}$ ), suggesting a structural imperfection of them [40]. The relative intensity ratios ( $I_D/I_G$ ) of the two peaks are related to the graphitization degree. The intensity ratios of D and G bands of MCNC/G and bare graphene are 0.94 and 0.84, respectively, indicating that both samples have partially disordered graphitic crystalline structure, but there are more defects in MCNC/G. These results could be due to the influence of relatively low pyrolysis temperature and acid treatment. The details of the differences in the pore structure and the Brunauer–Emmett–Teller (BET) specific surface area of the products were evaluated from the  $N_2$  adsorption-desorption isotherms and pore-size distributions (**Figure 3.6c and d and Figure 3.9**). As shown in **Figure 3.9**, the specific surface area and pore volume of the bare graphene sheets ( $265\text{ m}^2\text{ g}^{-1}$  and  $1.5\text{ cm}^3\text{ g}^{-1}$ ) declined significantly to  $137\text{ m}^2\text{ g}^{-1}$  and  $0.57\text{ cm}^3\text{ g}^{-1}$ , respectively, after deposition of the iron oxide nanoparticles due to the intrinsic low surface area of iron oxide and additional carbon coating on the

surface of graphene caused by the iron-oleate precursor. However, after removal of the iron oxide nanoparticles, the MCNC/G composite gave rise to a typical type IV isotherm with hysteresis, indicative of mesopores [41]. Further, the specific surface area ( $172.4 \text{ m}^2 \text{ g}^{-1}$ ) and pore volume ( $0.96 \text{ cm}^3 \text{ g}^{-1}$ ) were higher than those of IO@C/G composite due to the void spaces inside the CNCs formed by etching of the iron oxide nanoparticles.

The pore size distribution curves (**Figure 3.6d**) indicate a multimodal pore size distribution for the MCNC/G composite. The pore size distribution of MCNC/G is generally similar that of bare graphene (**Figure 3.9b**), except for the appearance of a peak centered at about 15 nm (yellow colored region), which may be attributed to the monodisperse CNCs. After infusion of sulfur into the MCNC/G composite, the surface area and pore volume declined significantly, providing clear evidence that sulfur occupies the available pores of the MCNC/G composite, which contains void spaces in the CNCS [42, 43].

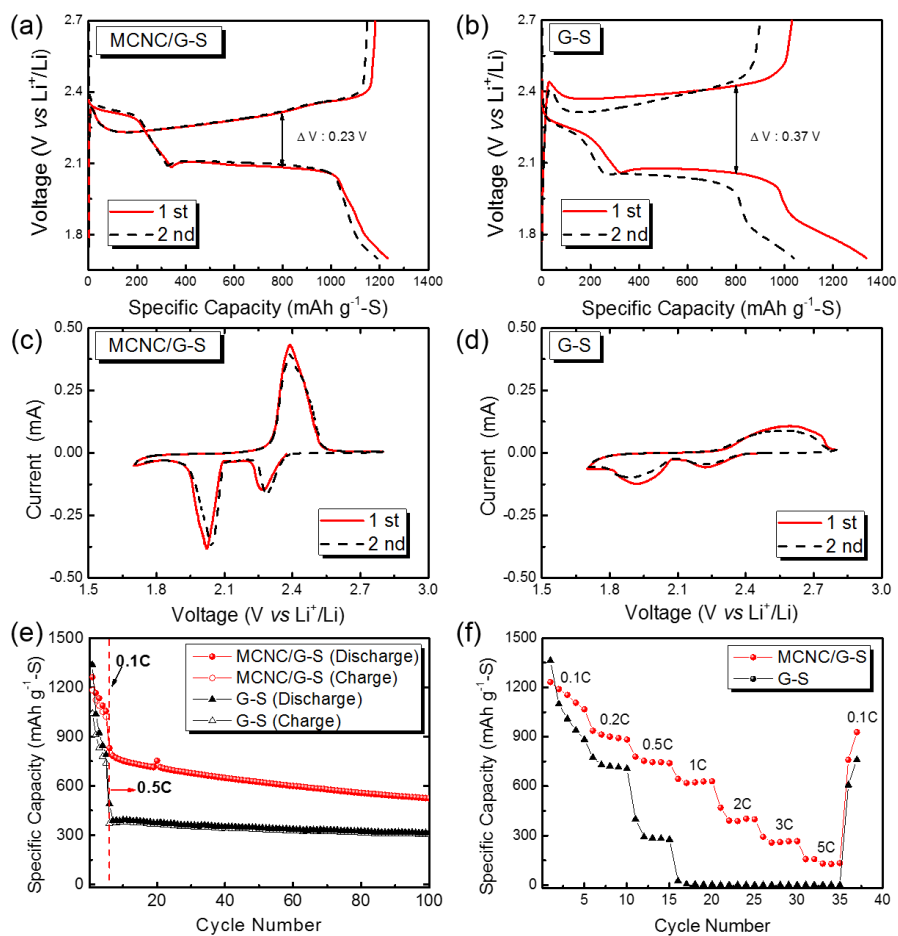


**Figure 3.10.** (a and b) Galvanostatic discharge/charge profiles of the MCNC/G-S and G-S composite at 0.1 C. (c and d) Cyclic voltammograms of the MCNC/G-S and G-S composite at a scanning rate of 0.1 mV s<sup>-1</sup>. (e) Cycling and (f) rate capability performance of the electrodes of the MCNC/G-S and G-S composite, respectively.

**Figure 3.10a and b** show typical charge-discharge profiles of the MCNC/G-S and G-S composites containing about 60 wt.% sulfur at a current density of 0.1 C. All discharge curves of MCNC/G-S and G-S show the typical two-plateau profile of Li-S batteries, with peaks around 2.3 and 2.1 V, respectively. These two plateaus are related to the formation of soluble long-chain polysulfides ( $\text{Li}_2\text{S}_8$ ,  $\text{Li}_2\text{S}_6$ ,  $\text{Li}_2\text{S}_4$ , and  $\text{Li}_2\text{S}_3$ ) at 2.3 V and the precipitation of insoluble short-chain polysulfides ( $\text{Li}_2\text{S}_2$  and  $\text{Li}_2\text{S}$ ) at 2.1 V due to the dissolution of sulfur during electrochemical cycling [1, 2]. Compared with the profiles of G-S, the capacity difference between the 1st and 2nd cycle is smaller in the case of MCNC/G-S, suggesting good reversibility and stability. Furthermore, the overpotentials ( $\Delta V$ ) determined from the profiles of the two samples indicate a difference in the electrode polarization (MCNC/G-S: 0.24 V and G-S: 0.39 V). The overpotential in the 1st cycle is caused by the dissolution of  $\text{Li}_2\text{S}$  into the electrolyte, which is closely related to the  $\text{Li}_2\text{S}$  particle size effect [44]. Smaller  $\text{Li}_2\text{S}$  particles lead to a considerably larger surface area of the polysulfide, which enhances the chemical reaction between  $\text{S}_8$  and  $\text{Li}_2\text{S}$ . Because the MCNC/G-S composite has small and uniform pores, it

can confine sulfur in the pores more effectively than the G-S composite, resulting in reduction of the overpotential with the former. The overpotential of the MCNC/G-S electrode in the 2nd cycle is similar to that in the 1st cycle, whereas the second cycle overpotential is larger than that of the 1st cycle in the case of G-S because the G-S structure cannot mitigate the dissolution of  $\text{Li}_2\text{S}$  with a large particle size.

The results presented above are consistent with the cyclic voltammograms (CV) acquired at a scanning rate of  $0.1 \text{ mV s}^{-1}$  (**Figure 3.10c and d**). **Figure 3.10c** shows the CV curve of the MCNC/G-S cathode in the 1st and 2nd cycles. Two reduction peaks were observed during the cathodic scan. The two apparent reduction peaks positioned around 2.3 and 2.0 V correspond to the two reduction processes of elemental S [45, 46]. These results correspond with the positions of the two plateaus in the discharge profiles in **Figure 3.10a**. In contrast with the apparent redox peaks at around 2.1 and 2.3 V, the CV curves of G-S show well-defined peaks with weak intensity under the same conditions. In the 1st cycle, the electrode fabricated with the G-S composite undergoes severe dissolution of polysulfides because the open structure of G-

S cannot confine the intermediate products of elemental S, resulting in an irreversible reaction and loss of the active materials and an inability to withstand the high C-rate.

The cycling performance of the MCNC/G-S and G-S composites is shown in **Figure 3.10e** (based on the mass of S,  $1\text{ C} = 1675\text{ mAh g}^{-1}$ ). After the initial 5 cycles at 0.1 C-rate, the MCNC/G-S composite delivered a high specific capacity of  $524.7\text{ mA h g}^{-1}$  after 100 cycles at 0.5 C-rate. In contrast, the capacity of G-S dropped significantly under the same conditions, even though the initial specific capacity ( $1337\text{ mA h g}^{-1}$ ) was higher than that of MCNC/G-S ( $1262\text{ mA h g}^{-1}$ ). In the rate capability test (**Figure 3.10f**), the MCNC/G-S composite exhibited an initial specific discharge capacity of  $1233.2\text{ mA h g}^{-1}$  at 0.1 C-rate and capacity values of  $779.9$  and  $644.4\text{ mA h g}^{-1}$  at 0.5 and 1 C-rate, respectively. The excellent rate-stability gave rise to specific discharge capacities of  $391.2$ ,  $265.9$ , and  $150\text{ mA h g}^{-1}$  even at higher rates of 2, 3, and 5 C, respectively, although the higher rate gave rise to capacity fading due to irreversible loss of the active material owing to the dissolution of polysulfide with increasing current. After a rate of 5 C, a discharge capacity of  $928.7\text{ mA h g}^{-1}$  was again obtained when

the rate was again reduced to 0.1 C. These rate performances are substantially better than those of the G-S composites. This can be attributed to the monodisperse carbon nanocapsules in the MCNC/G composite, which lead to small volume expansion and physical confinement of sulfur due to the void spaces inside the CNCs.

### 3.4. Conclusion

In summary, a MCNC/G composite with high electrochemical performance was prepared by a facile strategy for application to Li-S batteries. The strategy involves mixing of iron-oleate and graphene, heat treatment, and finally, acid etching of the iron oxide nanoparticles. The composites comprised highly uniform, hollow structured CNCs with a diameter of about 20 nm that were densely deposited on the surface of the graphene nanosheets. After heat-treatment, elemental sulfur was impregnated into the uniform void spaces of the CNCs and partially deposited on the graphene nanosheets. In this rational design, the void spaces inside the CNCs effectively confined the sulfur and polysulfides, leading to mitigation of the shuttle effect and improvement of the electrical conductivity of the sulfur cathode. Owing to the unique structure of the composites, the MCNC/G-S electrode exhibits excellent electrochemical performance compared to the bare G-S electrode. Typically, at 2 and 3 C-rates, the MCNC/G-S electrodes deliver discharge capacities of 391.2 and 265.9 mA h g<sup>-1</sup>. We believe that the MCNC/G composites will be useful in electrodes for other energy storage devices and applications.

### 3.5. References

- [1] A. Manthiram, Y. Z. Fu, S. H. Chung, C. X. Zu and Y. S. Su, *Chem. Rev.*, **2014**, 114, 11751.
- [2] A. Manthiram, Y. Z. Fu and Y. S. Su, *Acc. Chem. Res.*, **2013**, 46, 1125.
- [3] G. Y. Xu, B. Ding, J. Pan, P. Nie, L. F. Shen and X. G. Zhang, *J. Mater. Chem. A*, **2014**, 2, 12662.
- [4] N. Jayaprakash, J. Shen, S. S. Moganty, A. Corona and L. A. Archer, *Angew. Chem. Int. Ed.*, **2011**, 50, 5904.
- [5] N. Brun, K. Sakaushi, L. H. Yu, L. Giebeler, J. Eckert and M. M. Titirici, *Phys. Chem. Chem. Phys.*, **2013**, 15, 6080.
- [6] Z. Li, J. T. Zhang and X. W. Lou, *Angew. Chem. Int. Ed.*, **2015**, 54, 12886.
- [7] Z. Li, J. T. Zhang, Y. M. Chen, J. Li and X. W. Lou, *Nat. Commun.*, **2015**, 6, 8850.
- [8] Z. J. Sun, M. Xiao, S. J. Wang, D. M. Han, S. Q. Song, G. H. Chen and Y. Z. Meng, *J. Mater. Chem. A*, **2014**, 2, 15938.
- [9] C. F. Zhang, H. B. Wu, C. Z. Yuan, Z. P. Guo and X. W. Lou, *Angew. Chem. Int. Ed.*, **2012**, 51, 9592.
- [10] Y. Yang, G. Y. Zheng and Y. Cui, *Chem. Soc. Rev.*, **2013**, 42, 3018.

- [11] X. B. Cheng, J. Q. Huang, Q. Zhang, H. J. Peng, M. Q. Zhao and F. Wei, *Nano Energy*, **2014**, 4, 65.
- [12] C. H. Wang, H. W. Chen, W. L. Dong, J. Ge, W. Lu, X. D. Wu, L. Guo and L. W. Chen, *Chem. Commun.*, **2014**, 50, 1202.
- [13] K. K. Jin, X. F. Zhou, L. Z. Zhang, X. Xin, G. H. Wan and Z. P. Liu, *J. Phys. Chem. C*, **2013**, 117, 21112.
- [14] G. M. Zhou, E. Paek, G. S. Hwang and A. Manthiram, *Adv. Energy Mater.*, **2016**, 6, 1501355.
- [15] C. Tang, B. Q. Li, Q. Zhang, L. Zhu, H. F. Wang, J. L. Shi and F. Wei, *Adv. Funct. Mater.*, **2016**, 26, 577.
- [16] J. W. Kim, J. D. Ocon, H. S. Kim and J. Lee, *Chemsuschem*, **2015**, 8, 2883.
- [17] X. F. Li, M. F. Chi, S. M. Mahurin, R. Liu, Y. J. Chuang, S. Dai and Z. W. Pan, *Carbon*, **2016**, 101, 57.
- [18] Q. Sun, B. He, X. Q. Zhang and A. H. Lu, *ACS Nano*, **2015**, 9, 8504.
- [19] K. Xi, S. Cao, X. Y. Peng, C. Ducati, R. V. Kumar and A. K. Cheetham, *Chem. Commun.*, **2013**, 49, 2192.
- [20] S. Z. Niu, W. Lv, G. M. Zhou, Y. B. He, B. H. Li, Q. H. Yang and F. Y. Kang, *Chem. Commun.*, **2015**, 51, 17720.

- [21] M. M. Rao, W. S. Li and E. J. Cairns, *Electrochem. Commun.*, **2012**, 17, 1.
- [22] J. R. He, Y. F. Chen, P. J. Li, F. Fu, Z. G. Wang and W. L. Zhang, *J. Mater. Chem. A*, **2015**, 3, 18605.
- [23] L. Sun, W. B. Kong, Y. Jiang, H. C. Wu, K. L. Jiang, J. P. Wang and S. S. Fan, *J. Mater. Chem. A*, **2015**, 3, 5305.
- [24] L. W. Ji, M. M. Rao, H. M. Zheng, L. Zhang, Y. C. Li, W. H. Duan, J. H. Guo, E. J. Cairns and Y. G. Zhang, *J. Am. Chem. Soc.*, **2011**, 133, 18522.
- [25] G. M. Zhou, S. F. Pei, L. Li, D. W. Wang, S. G. Wang, K. Huang, L. C. Yin, F. Li and H. M. Cheng, *Adv. Mater.*, **2014**, 26, 625.
- [26] J. Z. Wang, L. Lu, M. Choucair, J. A. Stride, X. Xu and H. K. Liu, *J. Power Sources*, **2011**, 196, 7030.
- [27] G. M. Zhou, L. C. Yin, D. W. Wang, L. Li, S. F. Pei, I. R. Gentle, F. Li and H. M. Cheng, *ACS Nano*, **2013**, 7, 5367.
- [28] S. K. Liu, K. Xie, Z. X. Chen, Y. J. Li, X. B. Hong, J. Xu, L. J. Zhou, J. F. Yuan and C. M. Zheng, *J. Mater. Chem. A*, **2015**, 3, 11395.
- [29] G. M. Zhou, Y. B. Zhao and A. Manthiram, *Adv. Energy Mater.*, **2015**, 5, 1402263.

- [30] Y. F. Dong, S. H. Liu, Z. Y. Wang, Y. Liu, Z. B. Zhao and J. S. Qiu, *Nanoscale*, **2015**, 7, 7569.
- [31] X. Y. Zhao, J. P. Tu, Y. Lu, J. B. Cai, Y. J. Zhang, X. L. Wang and C. D. Gu, *Electrochim. Acta*, **2013**, 113, 256.
- [32] X. W. Wang, Z. A. Zhang, X. L. Yan, Y. H. Qu, Y. Q. Lai and J. Li, *Electrochim. Acta*, **2015**, 155, 54.
- [33] Y. C. Qiu, W. F. Li, G. Z. Li, Y. Hou, L. S. Zhou, H. F. Li, M. N. Liu, F. M. Ye, X. W. Yang and Y. G. Zhang, *Nano. Res.*, **2014**, 7, 1355.
- [34] B. Jang, O. B. Chae, S. K. Park, J. Ha, S. M. Oh, H. B. Na and Y. Piao, *J. Mater. Chem. A*, **2013**, 1, 15442.
- [35] A. C. Ferrari, J. C. Meyer, V. Scardaci, C. Casiraghi, M. Lazzeri, F. Mauri, S. Piscanec, D. Jiang, K. S. Novoselov, S. Roth and A. K. Geim, *Phys. Rev. Lett.*, **2006**, 97, 187401.
- [36] K. N. Kudin, B. Ozbas, H. C. Schniepp, R. K. Prud'homme, I. A. Aksay and R. Car, *Nano Lett.*, **2008**, 8, 36.
- [37] G. K. Ramesha and S. Sampath, *J. Phys. Chem. C*, **2009**, 113, 7985.
- [38] Z. J. Fan, J. Yan, T. Wei, G. Q. Ning, L. J. Zhi, J. C. Liu, D. X. Cao, G. L. Wang and F. Wei, *ACS Nano*, **2011**, 5, 2787.

- [39] Y. W. Zhu, S. Murali, W. W. Cai, X. S. Li, J. W. Suk, J. R. Potts and R. S. Ruoff, *Adv. Mater.*, **2010**, 22, 3906.
- [40] F. B. Su, X. S. Zhao, Y. Wang, J. H. Zeng, Z. C. Zhou and J. Y. Lee, *J Phys Chem B*, **2005**, 109, 20200.
- [41] S. K. Park, S. Woo, S. Lee, C. Y. Seong and Y. Piao, *RSC Adv.*, **2015**, 5, 52687.
- [42] K. Zhang, Q. Zhao, Z. L. Tao and J. Chen, *Nano. Res.*, **2013**, 6, 38.
- [43] Y. Zhao, W. L. Wu, J. X. Li, Z. C. Xu and L. H. Guan, *Adv. Mater.*, **2014**, 26, 5113.
- [44] Y. Gorlin, M. U. M. Patel, A. Freiberg, Q. He, M. Piana, M. Tromp and H. A. Gasteiger, *J. Electrochem. Soc.*, **2016**, 163, A930.
- [45] S. Rehman, S. J. Guo and Y. L. Hou, *Adv. Mater.*, **2016**, 28, 3167.
- [46] K. Zhang, F. R. Qin, Y. Q. Lai, J. Li, X. K. Lei, M. R. Wang, H. Lu and J. Fang, *ACS Appl. Mater. Interfaces*, **2016**, 8, 6072.

# **Chapter 4. Synthesis of Honeycomb-like Two-dimensional Mesoporous Carbon and Its Application in Lithium-Sulfur Batteries**

## **4.1. Introduction**

With the increasing need for inexpensive and efficient energy storage devices, rechargeable lithium-sulfur (Li-S) batteries become one of the most promising candidates for the next generation battery systems because of their high theoretical energy density ( $2600 \text{ Wh kg}^{-1}$ ), high theoretical specific capacity ( $1675 \text{ mA h g}^{-1}$ ), environmental friendliness and economic cost [1-3]. In spite of these considerable advantages, the utilization of sulfur as cathode bring serious problems that hinder their commercialization. First, sulfur and its intermediate products  $\text{Li}_2\text{S}_x$  during cycling ( $x=1-8$ ) show poor electronic and ionic conductivity, which results in poor active material utilization [4, 5]. Second, the intermediate products  $\text{Li}_2\text{S}_x$  (mainly  $2 < x \leq 8$ ) can be easily dissolved into the organic electrolyte solution, causing a rapid capacity fade and the

so-called “shuttle effect” that further aggravates the electrochemical performances by forming the electrochemically inactive layer on the anode ( $\text{Li}_2\text{S}_2$  or  $\text{Li}_2\text{S}$ ) [6, 7]. In addition, the huge volume expansion of sulfur could cause serious structural collapse of the electrode, which further decrease the cycling stability of cell [8, 9].

A reasonable solution to overcome these problems is that combining sulfur with carbon materials such as graphene [10-13], carbon nanotubes [14-16], carbon coating [17, 18], and porous carbon [19-21], which could improve the electrical conductivity of cathode and alleviate the dissolution of polysulfides into the electrolyte solution. Especially, in comparison with other carbon materials, porous carbon materials can buffer the volume change of sulfur and absorb polysulfides due to the presence of pores, resulting in improved cycle stability and Columbic efficiency [22-25]. Zhang group synthesized a mesoporous carbon foam with a high specific surface area that exhibits the improved electrochemical performance due to its porous structure [26]. Among the various porous carbon materials, ordered mesoporous carbon with high surface area and large pore volume has been

considered as promising host for sulfur loading [27-30]. Its ordered mesochannel shorten the distance of ion diffusion and also, high conductivity is in favor of fast electron transport during cycling. Nazar group firstly demonstrated that a cathode based on nanostructured sulfur/highly ordered mesoporous carbon (CMK-3) materials can exhibit stable and reversible capacities [31], which has opened up new possibilities for Li-S batteries. Sun group developed ordered mesoporous carbon/sulfur composites with hierarchical structure which delivers a superior reversible capacity and high rate capability [30]. Most of the ordered mesoporous carbon materials studied, such as cubic or hexagonal structures, are three-dimensional (3D) assemblies with interconnected mesostructured frameworks. In contrast, a well-defined two-dimensional (2D) mesoporous carbon material with ordered structures and uniform pore size has been rarely reported to date.

2D nanostructured carbon materials such as graphene and carbon sheets are being newly explored for energy storage systems owing to their large surface-to-volume ratios and continuous pathways for electron transport [32-35]. Moreover, some studies have shown the introducing pores into 2D carbon materials, that provides short

distance for charge transfer, pore channel configuration with a large specific surface area, and better contact between electrolyte and active materials than bare 2D carbon materials [36-38]. For example, Kang group prepared nitrogen-doped hierarchical porous carbon nanosheets via direct pyrolysis. The as-prepared sample shows high discharge capacity and Coulombic efficiency when used a cathode host for Li-S [38]. Ruoff group synthesized a porous graphene with extremely high surface area via chemical activation (KOH), which shows the improved specific capacitance value [39]. However, the reported 2D porous carbon materials exhibit irregular and wide pore size distribution and the orderings of the mesostructures were mostly poor, leading to heterogeneous contact between sulfur and carbon conductors, followed by partially unstable electrochemical reaction [40]. In addition, time-consuming and low-yield synthetic methods resulted from complicated process limit the mass production and cost-down. Therefore, it is required to develop facile synthetic methods of 2D carbon materials with ordered mesostructure for effective cathode host of Li-S batteries.

Herein, we report the successful synthesis of honeycomb-like ordered mesoporous carbon nanosheets (OMCNS) by an etching of self-assembled iron oxide nanocubes/carbon hybrid nanosheets as a new sulfur host for Li-S batteries. While the synthetic process is simple and uncomplicated, as-obtained nanosheets have close-packed uniform cubic mesopores of ~20 nm side length. The sulfur element is incorporated into the empty mesopores by simple melting infusion process (OMCNS-S). The uniform cubic mesopores offer enough space for the volume expansion of sulfur inside and trap the polysulfides during charging-discharging process. Furthermore, the OMCNS structure provides a short diffusion distance of ion and fast electron transport through its carbon framework, thus allowing for improved electrochemical performances.

## **4.2. Experimental Section**

### **4.2.1. Chemicals**

$\text{FeCl}_3 \cdot 6\text{H}_2\text{O}$  and  $\text{Na}_2\text{SO}_4$  were purchased from Sigma-Aldrich. Sodium oleate and sulfur powder were purchased from TCI and Samchun, respectively. All reagents were used without further purification.

### **4.2.2. Characterization methods**

X-ray diffraction (XRD) patterns were measured using a D8-advances diffractometer with a  $\text{Cu K}\alpha$  radiation source from  $20$  to  $70^\circ$  at a scan rate of  $2^\circ \text{ min}^{-1}$ . The crystalline structure and morphology of the samples was investigated by transmission electron microscopy (TEM, JEOL JEM-2010) equipped with an energy-dispersive X-ray (EDX) spectrometer and field-emission scanning electron microscopy (FE-SEM, Hitachi S-4800). Thermal gravimetric analysis (TGA) was performed using the TGA/DSC 1 (Mettler Toledo) thermal analyzer at a heating rate of  $10^\circ \text{ C min}^{-1}$  under an  $\text{N}_2$  atmosphere. To confirm the specific surface area and pore size distribution of the samples, the Brunauer-Emmett-Teller (BET) were measured by  $\text{N}_2$  adsorption/desorption using the BELSORP-mini II adsorption analyzer. Raman spectra were obtained by a Raman spectrometer (HORIBA Scientific-T64000) equipped with a  $514.5 \text{ nm}$  Argon laser.

### **4.2.3. Preparation of ordered mesoporous carbon nanosheets (OMCNS)**

Iron-oleate precursor was prepared following a previously reported method [28, 29]. For the preparation of OMCNS, 2.5 g of iron-oleate was mixed with 40 g of  $\text{Na}_2\text{SO}_4$  and the mixture was heated at 600 °C under Ar atmosphere for 3 h. After heating, carbon sheets embedded with iron oxide nanoparticles were washed with water for 3 h to remove  $\text{Na}_2\text{SO}_4$  and the iron oxide nanoparticles were etched with HCl. The black colored powder was obtained by filtration and thermally treated at 800 °C for 3 h to improve the conductivity of carbon.

### **4.2.4 Preparation of OMCNS-S composites**

The sulfur loading into OMCNS powder was implemented by the common melting-diffusion method [30, 31] In a typical process, the as-prepared OMCNS powder was ground with sulfur (70 wt % of total mass). The mixture was then transferred to alumina boat and heated to 155 °C in a tube furnace for 18 hrs under Ar atmosphere.

### **4.2.5 Electrode preparation**

The electrode of OMCNS-S was made up an active material, conducting agent (Acetylene black), and polymer binder (Polyvinylidene flouroide, PVdF) by a weight ratio of 7:2:1 (wt%), it was surely homogenized by

using a ball-milling (Mini-Mill PULVERISETTE 23, FRITSCH) at 40 instruction per second during 30 min. The homogeneous slurry was casted on commercial aluminum foil by using a doctor blade (the thickness of 100  $\mu\text{m}$ ). The manufactured electrodes were dried in a vacuum oven at 60 $^{\circ}\text{C}$  during the overnight, and were punched for a diameter (11 mm). The mass loading of OMCNS-S active material is averagely 1.1-1.3  $\text{mg cm}^{-2}$ .

#### **4.2.6 Electrochemical characterization**

Electrochemical performances were performed by using a coin cell (CR2016-type). All cells were manufactured in aGn-filled glove box (both  $\text{O}_2$  and  $\text{H}_2\text{O}$  amount below 0.1 ppm). Polymer separator (Celgard 2400) was used and an electrolyte consists of 1.0 M bis(trifluoromethane)sulfonimide lithium salt (LiTFSI) and 0.3 M  $\text{LiNO}_3$  in 1:1 mixture (volume %) of 1,3-dioxolane (DOL) and dimethoxymethane (DME). A lithium metal foil as an anode electrode was used and all cell tests were measured for a half-cell. All electrochemical evaluations were carried out at a room temperature. Galvanostatic measurement (WBCS3000s cycler, WonATech, Korea) was used in a potential window of 1.7-2.8 V vs.  $\text{Li}^+/\text{Li}$ .

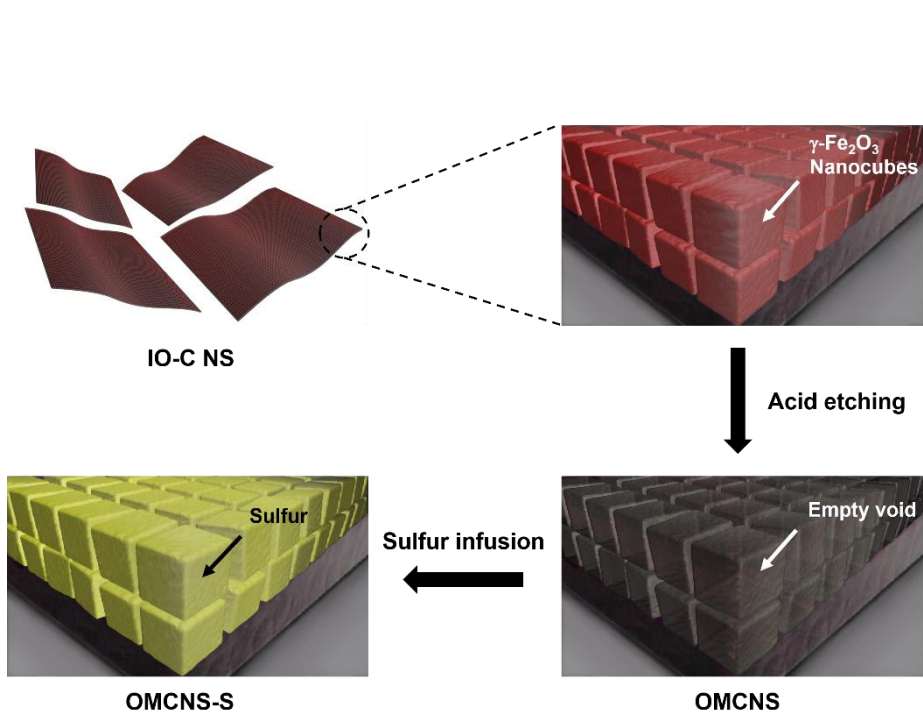


**Figure 4.1.** Schematic illustration of preparation of the OMCNS and OMCNS-S composites.

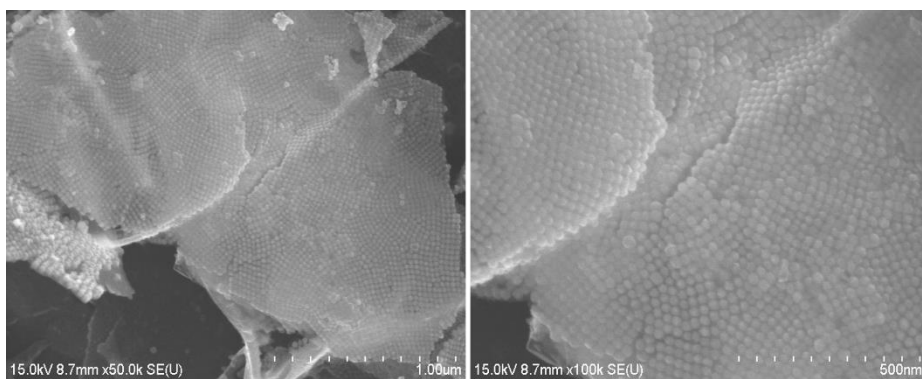


**Figure 4.2.** SEM images of IO-C NS.



**Figure 4.3.** Large scale synthesis of OMCNS.

### 4.3. Results and Discussion

The synthesis of OMCNS is carried out by a modification of the previous report from our group (**Figure 4.1**) [43]. First, carbon nanosheets embedded with iron oxide ( $\gamma\text{-Fe}_2\text{O}_3$ ) nanocubes are synthesized via heating a mixture of iron-oleate precursor and sodium sulfate ( $\text{Na}_2\text{SO}_4$ ) fine powder at 600 °C for 3 h under Ar atmosphere. During this process, both the formation of  $\gamma\text{-Fe}_2\text{O}_3$  nanocubes and their self-assembly occur at the surface of the sodium sulfate powder (**Figure 4.2**). At the same time, alkyl ligands of oleate that binding the surface of the nanocubes are carbonized into the nanosheets. The obtained black colored powder was washed by DI water and further acid etched to remove sodium sulfate powder and the iron oxide nanocubes, respectively, leaving the ordered mesoporous carbon nanosheets. The above thermal processing is accomplished using solid-phase state without any solvents, which enables this in situ synthetic approach inexpensive and suitable for the mass production of OMCNS (**Figure 4.3**).

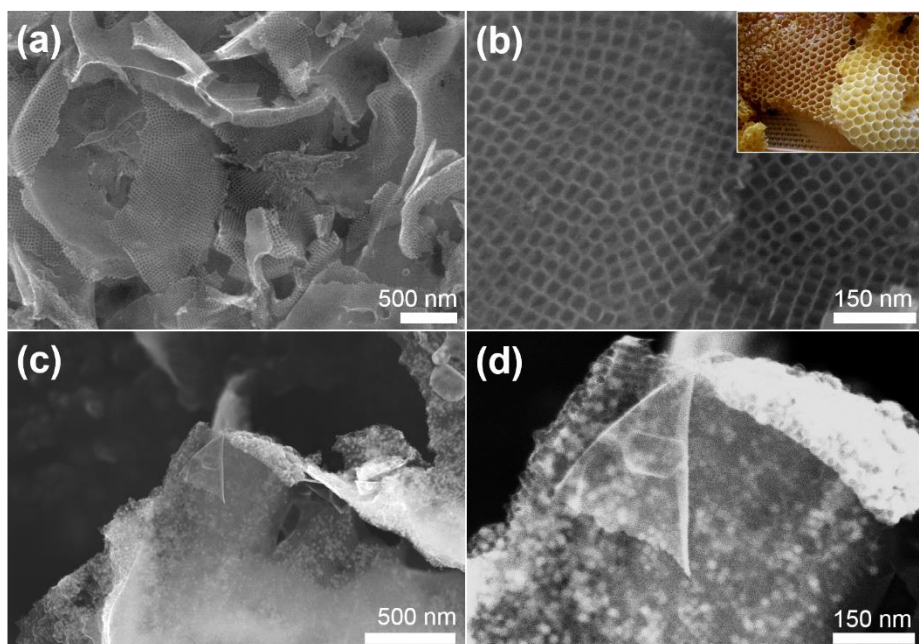


**Figure 4.4.** SEM images of (a, b) OMCNS (inset: a photo image of honeycomb) and (c, d) OMCNS-S composites.

The morphology and structure of OMCNS were investigated by FE-SEM (**Figure 4.4**). A large number of OMCNSs with their sizes of several micrometers and thickness of several nanometers can be observed (**Figure 4.4a**). The OMCNS consists of uniform cubic mesopores of  $\sim 20$  nm side length and the gap between pores is about 4 nm (**Figure 4.4b**). Actually, this structure resembles the honeycomb consisting of ordered array of hexagonal pores partitioned by honeycomb walls (**the inset of Figure 4.4b**), which implies structural stability and large pore volume. After sulfur infusion, the pores inside OMCNS were filled with sulfur species of the same shape as the cubic mesopores (**Figure 4.4c and d**). These images provide obvious evidence that the elemental melted sulfur species was well infusion into the pores of OMCNS due to the good wettability and capillarity interaction with carbon [44]. In contrast, the SEM images of G-S display some agglomerated sulfur microparticles (**Figure 4.5c and d**), suggesting that the unique structure of OMCNS successfully hinder the rapid growth of sulfur crystals during the melting process.

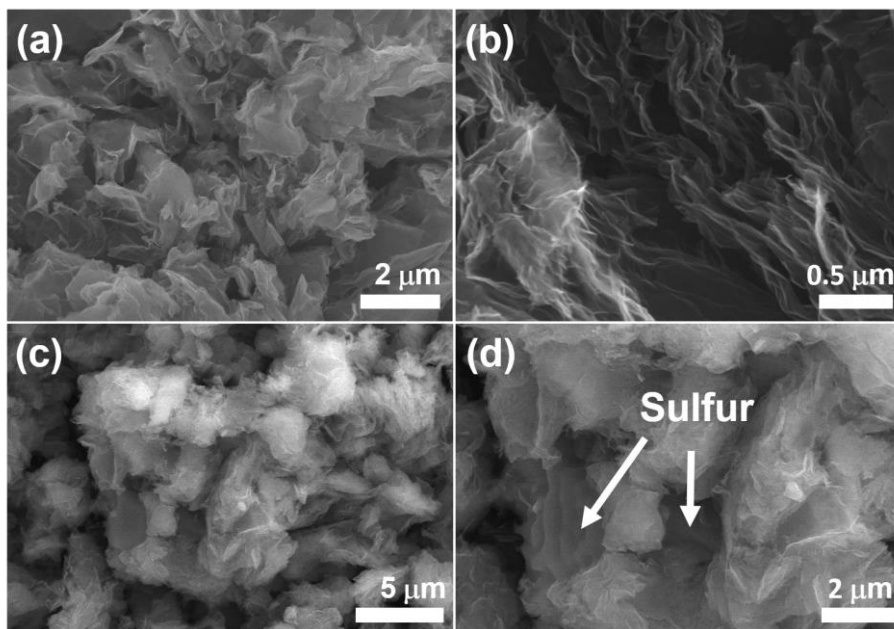


**Figure 4.5.** SEM images of (a, b) bare graphene nanosheets and (c, d) G-S composite (sulfur content: 70 wt%)

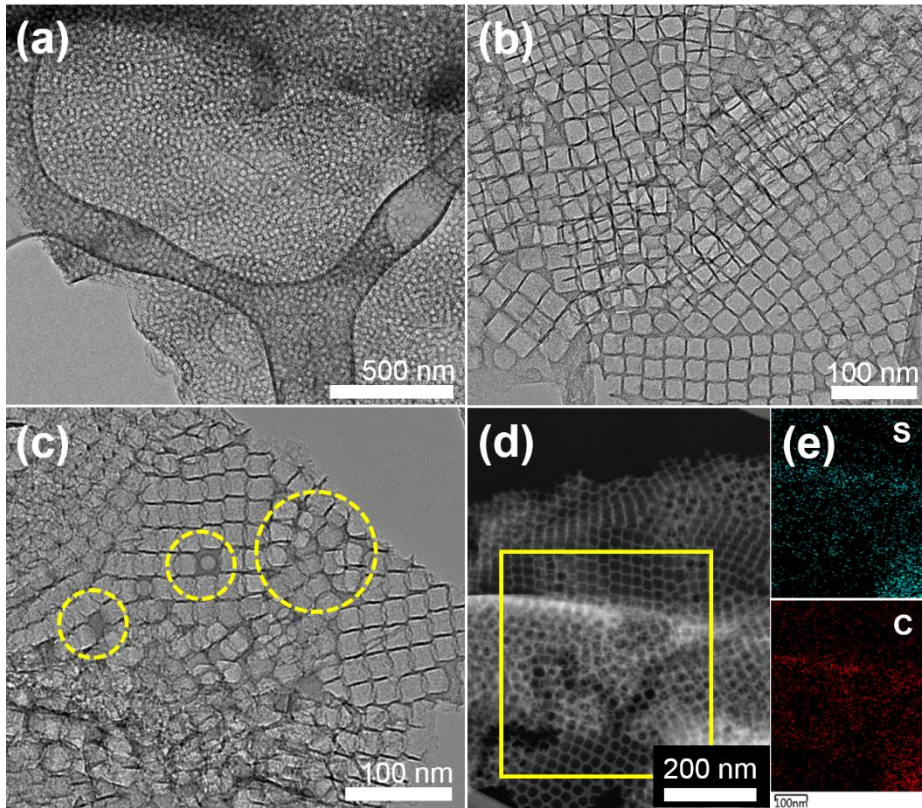


**Figure 4.6.** TEM images of (a, b) OMCNS and (c) OMCNS-S. (d , e) A dark field image and the corresponding S and C element mapping of OMCNS-S composite.

To investigate the detailed pore structure and sulfur distribution in the samples, TEM and the corresponding elemental mapping were carried out in the selected region (**Figure 4.6**). The mesopores form ordered arrangement over the whole area of the carbon nanosheets that is as large as several square micrometers (**Figure 4.6a and b**). This result is in agreement with the SEM data. In a TEM image of OMCNS-S, some of the mesopores are filled with some dark species and some are filled with nothing, the dark species are believed to be sulfur (yellow circles, **Figure 4.6c**) [6, 45, 46]. Due to the electron beam under the ultra-high vacuum, almost sulfur may sublime off, resulting in mesopores with nothing left inside. The dark field TEM image and the corresponding elemental mapping of carbon and sulfur give visible evidence that sulfur was uniformly distributed on the surface of nanosheets and inside mesopores (**Figure 4.6e**).

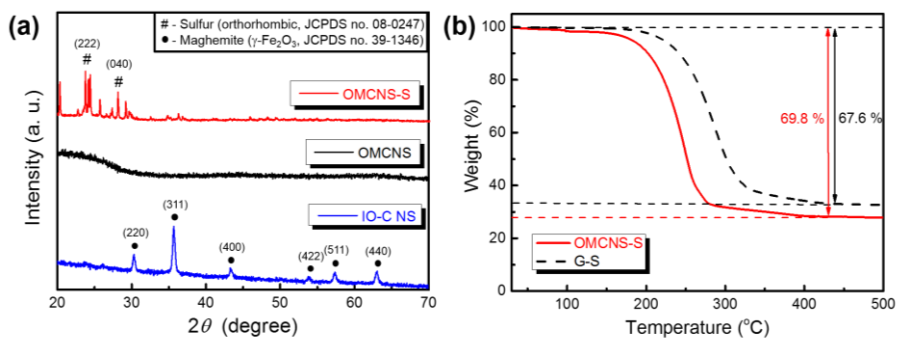


**Figure 4.7.** (a) The XRD pattern of the IO-C NS, OMCNS and OMCNS-S. (b) A TGA curve of the OMCNS-S and G-S.

X-ray diffraction (XRD) analysis are performed to figure out the crystal structure and phase purities of IO-C NS, OMCNS, and OMCNS-S composite as shown in **Figure 4.7a**. Firstly, all diffraction peaks of the IO-C NS are attributed to the maghemite phase ( $\gamma$ -Fe<sub>2</sub>O<sub>3</sub>, JCPDS No. 39-1346) without any impurity peaks. After etching process for IO-C NS, no peaks corresponded to maghemite phase were observed in the XRD pattern of OMCNS, implying that the iron oxide nanocubes inside IO-C NS were completely removed. The XRD pattern of OMCNS-S composite is in accord with reference peaks of elemental sulfur (orthorhombic, JCPDS No. 08-0247), resulting that the process of sulfur infusion into the OMCNS does not induce any structural changes as well as impurities. TGA was conducted in N<sub>2</sub> atmosphere to determine the sulfur content in OMCNS-S composite. As shown in **Figure 4.7b**, the sulfur content of OMCNS-S is 70 wt%, which the mass loss of elemental sulfur from vaporization is entirely finished after 300°C.

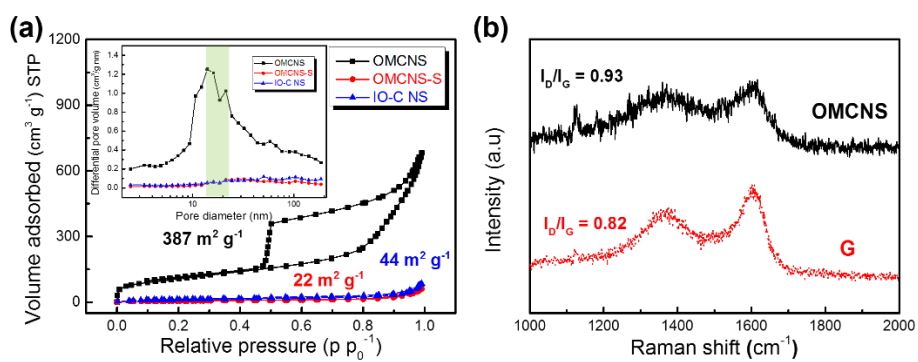


**Figure 4.8** (a) Nitrogen adsorption-desorption isotherms of the OMCNS, OMCNS-S and IO-C NS composites (inset: pore-size distributions) and (b) Raman spectra of OMCNS and bare graphene.

$N_2$  adsorption-desorption measurement was carried out to further investigate the details of the differences in the pore structure and calculate the specific surface area of samples (**Figure 4.8**). As shown in Fig. 5a, the  $N_2$  adsorption-desorption isotherm of OMCNS exhibits a typical type IV isotherm with hysteresis, indicating presence of mesopores in OMCNS [47]. After acid etching of IO-C NS ( $44.4 \text{ m}^2 \text{ g}^{-1}$  and  $0.13 \text{ cm}^3 \text{ g}^{-1}$ ), the obtained OMCNS exhibits high specific surface area and pore volume ( $386.7 \text{ m}^2 \text{ g}^{-1}$  and  $1.05 \text{ cm}^3 \text{ g}^{-1}$ ), which is due to the void spaces inside OMCNS formed by removal of iron oxide nanocubes. From the pore size distribution curves, it could be clearly observed that the pore sizes are distributed narrowly and located at about 15 and 20 nm, suggesting the existence of uniform mesopores in OMCNS, which is consistent with the pore size observed from SEM and TEM images (**Figure 4.8a inset**). After sulfur infiltration into OMCNS, the surface area and pore volume decreased significantly, indicating that the available pores of the OMCNS are filled with sulfur species.

Raman scattering is significantly sensitive to the electronic structure and effective tool for characterizing crystallinity of carbon. In **Figure 4.8b**, Raman spectra show obvious two peaks located at

*ca.* 1360 and 1600  $\text{cm}^{-1}$  which correspond to D and G bands of disordered graphitic materials. The D band is attributed to the vibration of carbon atoms with dangling bonds of the disordered graphite while the G band is associated with the vibration of  $\text{sp}^2$ -bonded carbon atoms ( $\text{C}=\text{C}$ , typical graphite bonds) [48]. It is worth noting that the G band peaks of both samples are shifted to higher wavelength number as compared with that of graphite crystals ( $1580 \text{ cm}^{-1}$ ), indicating a structural imperfection of the both samples [49]. The relative intensities ( $I_{\text{D}}/I_{\text{G}}$ ) of the two peaks indicate the graphitization degree. The intensity ratios of D and G bands of OMCNS and bare graphene are 0.93 and 0.82, respectively, implying that both samples have graphitic crystalline structure with some disorders, but there are more defects in OMCNS. These results may be due to the influence of relatively low pyrolysis temperature and acid treatment.

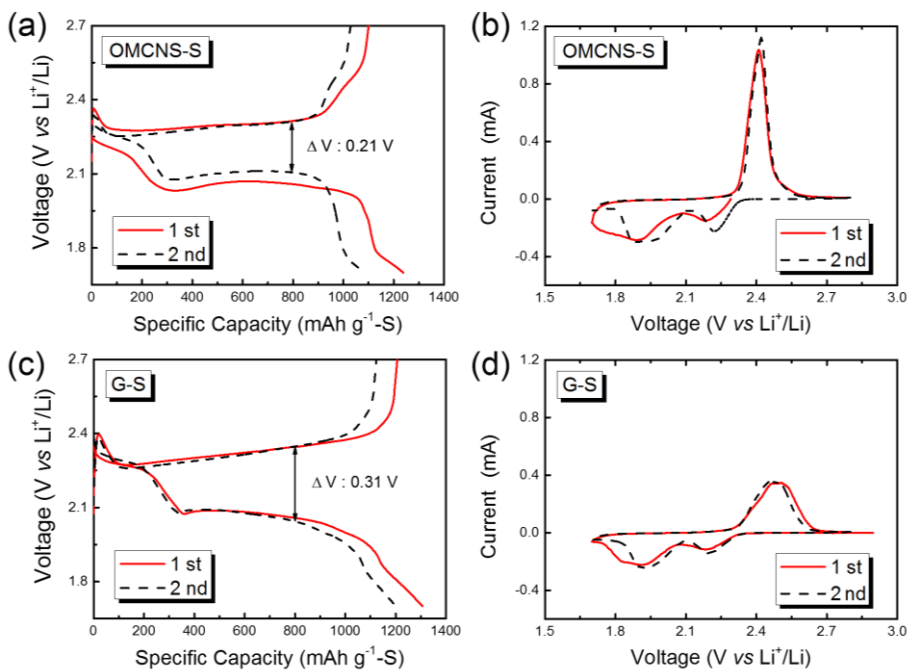


**Figure 4.9.** (a, c) Charge-discharge curves of OMCNS-S and G-S composites, obtained using a current density of 0.1C. (b, d) Cyclic voltammetry (CV) profiles of OMCNS-S and G-S composites obtained at a scanning rate of  $0.05 \text{ mV s}^{-1}$ .

**Figure 4.9a and c** show the charge/discharge profiles of OMCNS-S and G-S composites, respectively. The two electrodes are cycling with a cut-off voltage window of 1.7–2.8 V at 0.1 C. In the discharge curves, two plateaus are observed at about 2.3 and 2.05 V during a shuttle reaction in which the one at 2.3 V is corresponded to the formation polysulfides with high chain of sulfur ( $\text{Li}_2\text{S}_x$ ,  $x= 6-8$ ) from  $\text{S}_8$ , resulting from the reduction reaction of sulfur with  $\text{Li}^+$  during discharge process. The other at 2.05 V is related to the formation of lower order polysulfides  $\text{Li}_2\text{S}_x$  ( $2 < x \leq 6$ ). During the following charge process, only one plateau was obtained at approximately 2.3 V, corresponding the reversible oxidation of soluble polysulfides [15, 20, 29] to  $\text{S}_8$ . The gap between the charge and discharge curves (overpotential) of the OMCNS-S electrode was narrower than that of the G-S electrode, suggesting the improved electrical performance of OMCNS-S. Although the graphene has high specific surface area and superior electrical conductivity that are favorable for the accessibility for  $\text{Li}^+$  and electrons, its open structure limits the suppression of the polysulfides dissolution into organic electrolyte during the shuttle

reaction. Thus, the G-S electrode exhibited electrical contact loss, resulting in larger hysteresis during electrochemical cycling.

The cyclic voltammetry (CV) profiles of the OMCNS-S and G-S composites are shown in **Figure 4.9b and d**. CV tests of OMCNS-S and G-S composites are performed in the voltage range of 1.7–2.8 V with a scan rate of  $0.05 \text{ mV s}^{-1}$ . During the first scan, two reduction peaks at about 2.30 V and 2.05 V and one anodic peak at 2.38 V were observed, which are in accord well with the charge-discharge profiles. In the 2<sup>nd</sup> scan, anodic shifts of reduction peaks are found, indicating a lowered polarization of the electrode material.

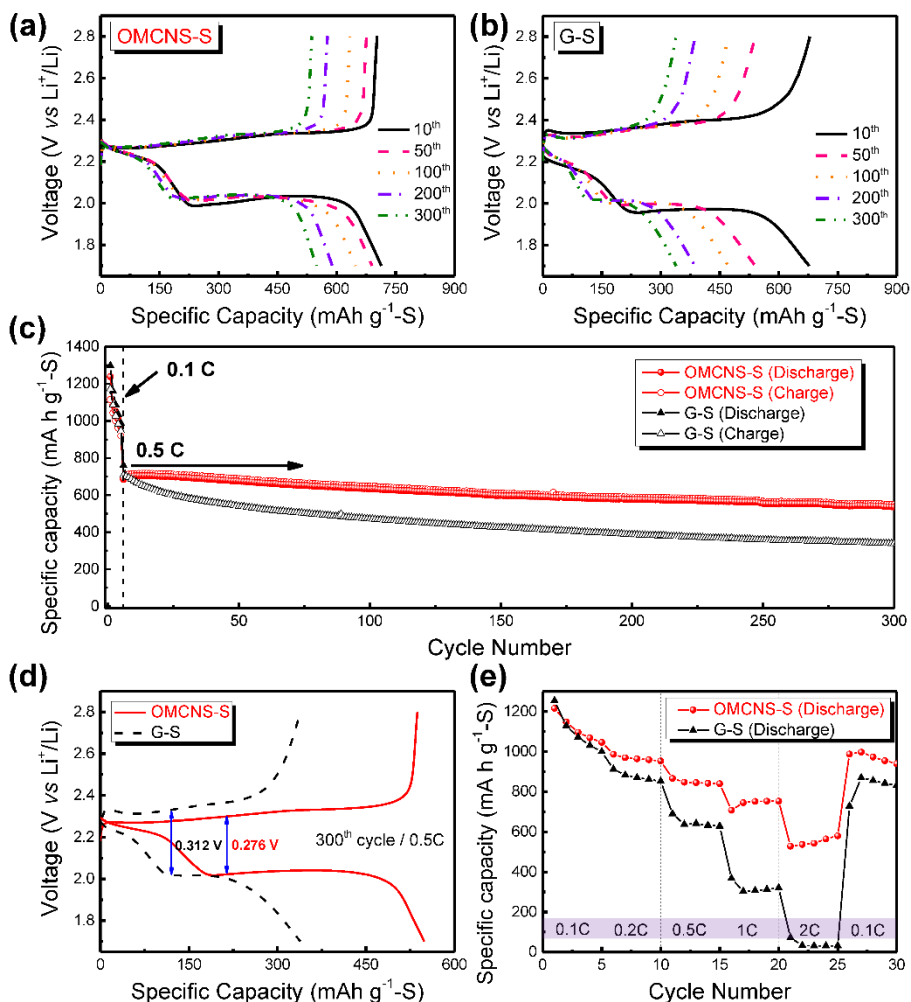


**Figure 4.10** Galvanostatic charge-discharge curves of (a) OMCNS-S and (b) G-S electrodes at 10<sup>th</sup>, 50<sup>th</sup>, 100<sup>th</sup>, 200<sup>th</sup>, and 300<sup>th</sup> cycles at a current density of 0.5C (c) Cycle performance at current densities of 0.1C and 0.5C. (d) Charge-discharge curves in 300<sup>th</sup> cycle at a current density of 0.5C, and (e) Rate capability at various current densities (0.1C, 0.2C, 0.5C, 1C, and 2C) of OMCNS-S and G-S composites.

**Figure 4.10a and b** show the cycled charge-discharge profiles of the OMCNS-S and G-S electrodes at a current density of 0.5C. As shown in **Figure 4.10a**, the charge-discharge curves of OMCNS-S electrode present clear two cathodic and one anodic plateaus at 10<sup>th</sup>, 50<sup>th</sup>, 100<sup>th</sup>, 200<sup>th</sup>, and 300<sup>th</sup> cycles. The OMCNS-S electrode delivers the specific discharge capacity of 713.9 mA h g<sup>-1</sup> at 10<sup>th</sup> cycles and exhibits a stable capacity retention about 80 % of the capacity of 10<sup>th</sup> cycles even after 300 cycles. In contrast, the G-S electrode without pore structure undergo a rapid capacity decay during 300 cycles under same conditions (**Figure 4.10b**). The corresponding cycling performance is shown in **Figure 4.10c**. Before cycle test at 0.5 C, the cells were first cycled at 0.1 C for 10 cycles to activate the redox reaction. During the initial 10 cycles (0.1 C), two electrodes have a similar decreasing tendency, however, when the current density increased to 0.5 C, the G-S electrode shows a rapid capacity decay compared to the OMCNS-S electrode. The difference between capacity values of two electrodes is continuous increasing to 300 cycles, finally, the OMCNS-S and G-S electrodes delivers the specific discharge capacities of 548.6 and 339 mA h g<sup>-1</sup>, respectively. After 300 cycles,

the charge/discharge profiles of both cells were obtained as shown in **Figure 4.10d**. The OMCNS-S cell has the over-potential of 0.276 V at 300<sup>th</sup> cycle which is higher than that of 1<sup>st</sup> cycle (0.21 V, as shown in **Figure 4.9a**). The result is due to the increased internal resistance caused by the dissolution of lithium polysulfides during cycling. The over-potential of G-S cell after 300 cycles is higher than that of OMCNS-S cell (0.312 V), which is attributed to high dissolution rate of polysulfides of G-S with open structures.

To investigate the rate capabilities of OMCNS-S and G-S electrodes, we carried out electrochemical testing at various current densities (**Figure 4.10e**, 0.1 to 2 C). To prevent the irreversible reaction resulting from the reduction of  $\text{LiNO}_3$ , the cell was measuring over a voltage window of 1.7 to 2.8 V [50]. The OMCNS-S electrode exhibited an initial specific discharge capacity of 1216 mA h g<sup>-1</sup> at 0.1 C-rate and capacity values of 840 and 753 mA h g<sup>-1</sup> at 0.5 and 1 C-rate, respectively. Even at the high current density of 2 C, the OMCNS-S electrode delivered a specific capacity of 580 mA h g<sup>-1</sup>, whereas that of G-S electrode was under 10 mA h g<sup>-1</sup>. It is noteworthy that the discharge capacity of the OMCNS-S electrode rose to over 1000 mA h g<sup>-1</sup> when the current

density decreased to 0.1 C, revealing that the electrochemical performance of the OMCNS-S composites is not deteriorated by high current density. The high capacity and excellent rate capability of OMCNS-S can be attributed to the great electrical conductivity, high surface area, and unique mesoporous structure, indicating that it could efficiently prevent dissolution of polysulfides compare to the bare graphene.

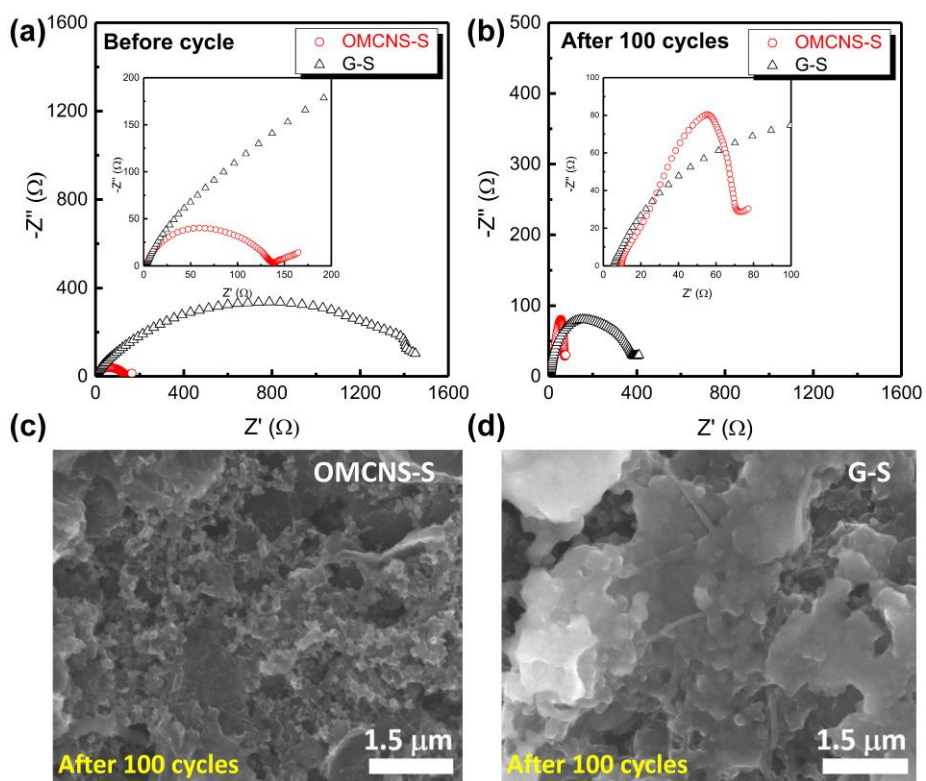


**Figure 4.11** Electrochemical impedance spectra of OMCNS-S and G-S electrodes (a) before cycling and (b) after 100 cycling. SEM images of (c) OMCNS-S and (d) G-S electrodes after 100 cycles at 0.5 C.

As shown in **Figure 4.11a and b**, the stability of the OMCNS-S and G-S electrodes is also evidenced by the electrochemical impedance spectroscopy (EIS) data before and after 100 cycles at 0.5 C-rate. The Nyquist plots show depressed semicircles in the medium frequency range, which corresponded to the charge-transfer resistance ( $R_{ct}$ ) of the cells generated at the interface between the electrolyte and electrode and formation of lithium polysulfides ( $Li_2S_2$  and  $Li_2S$ ) [51]. The OMCNS-S electrode had a considerably lower  $R_{ct}$  before cycling compared to G-S electrode. After 100 cycles, the EIS results of two electrodes had a similar tendency with lower  $R_{ct}$  of OMCNS-S electrode compared with G-S sample, indicating that polysulfides were well confined in the cathode and dissolution of polysulfides into electrolyte was successfully avoided owing to a unique mesoporous structure of OMCNS. **Figure 4.11c and d** shows SEM images of OMCNS-S and G-S electrodes after 100 cycles. In the SEM image of OMCNS-S electrode, it is observed that the OMCNS-S electrode still maintain a porous structure to penetrate the electrolyte while the G-S electrode loses its a unique structure due to a severe dissolution of lithium polysulfides, which is corresponds to EIS results in **Figure 4.11b**. The continuous accumulation of lithium polysulfides on electrodes have a bad influence on the cycle stability and

rate capability.

The outstanding overall electrochemical performance of a OMCNS-S cathode could be attributed to the following factors. First, the OMCNS host can confine and encapsulate the sulfur and polysulfides inside its numerous mesopores with ordered structure by a physical interaction. A well-uniform pores with diameter of 15-20 nm in OMCNS provide mesopore traps for sulfur elements during melting process that have easily access  $\text{Li}^+$  ions from the electrolyte and electrons from the Al current collectors. Second, the OMCNS exhibits an excellent electrical conductivity that is sufficient for fast electron transport within the electrode. Third, the 2D nanostructure of OMCNS is favorable for high-performance energy storage systems owing to excellent mechanical strength, large surface-to-volume ratios and short pathways for a rapid electron and ion transport.

#### **4.4. Conclusion**

To better suppress the rapid capacity decay during cycling and improve the electrical conductivity of cathode for Li-S batteries, it is required to develop simple synthetic methods of carbon materials with a novel nanostructure for effective cathode host. In this work, we report the successfully synthesis of ordered mesoporous carbon nanosheets by an etching of self-assembled iron oxide/carbon hybrid nanosheets as an advanced sulfur host for Li-S batteries. The obtained 2D nanosheets have close-packed uniform cubic mesopores of ~20 nm side length, resembling honeycomb structure. We loaded OMCNS with sulfur element simple melting infusion process and evaluate the performance of the resulting OMCNS-sulfur composites as cathode material. The improved electrochemical properties could be attributed to the fact that the uniform cubic mesopores offer enough space for the volume expansion of sulfur inside and trap the polysulfides during charging-discharging process. Therefore, this unique structured carbon nanosheets can be promising candidate for other energy storage applications.

#### 4.5. References

- [1] S. S. Zhang, *J. Power Sources*, **2013**, 231, 153.
- [2] A. Manthiram, Y. Z. Fu and Y. S. Su, *Acc. Chem. Res.*, **2013**, 46, 1125.
- [3] S. Evers and L. F. Nazar, *Acc. Chem. Res.*, **2013**, 46, 1135.
- [4] Y. X. Yin, S. Xin, Y. G. Guo and L. J. Wan, *Angew. Chem. Int. Ed.*, **2013**, 52, 13186.
- [5] D. Bresser, S. Passerini and B. Scrosati, *Chem. Commun.*, **2013**, 49, 10545.
- [6] W. D. Zhou, Y. C. Yu, H. Chen, F. J. DiSalvo and H. D. Abruna, *J. Am. Chem. Soc.*, **2013**, 135, 16736.
- [7] Y. Z. Fu and A. Manthiram, *J. Phys. Chem. C*, **2012**, 116, 8910.
- [8] Z. W. Seh, W. Y. Li, J. J. Cha, G. Y. Zheng, Y. Yang, M. T. McDowell, P. C. Hsu and Y. Cui, *Nat. Commun.*, **2013**, 4.
- [9] G. Y. Xu, B. Ding, L. F. Shen, P. Nie, J. P. Han and X. G. Zhang, *J. Mater. Chem. A*, **2013**, 1, 4490.
- [10] G. J. Hu, C. Xu, Z. H. Sun, S. G. Wang, H. M. Cheng, F. Li and W. C. Ren, *Adv. Mater.*, **2016**, 28, 1603.
- [11] A. Vizintin, M. Lozinsek, R. K. Chellappan, D. Foix, A. Krainc, G. Mali, G. Drazic, B. Genorio, R. Dedryvere and R. Dominke, *Chem.*

- Mater.*, **2015**, 27, 7070.
- [12] D. H. Wang, D. Xie, T. Yang, Y. Zhong, X. L. Wang, X. H. Xia, C. D. Gu and J. P. Tu, *J. Power Sources*, **2016**, 313, 233.
- [13] J. X. Song, Z. X. Yu, M. L. Gordin and D. H. Wang, *Nano Lett.*, **2016**, 16, 864.
- [14] Y. C. Jeong, K. Lee, T. Kim, J. H. Kim, J. Park, Y. S. Cho, S. J. Yang and C. R. Park, *J. Mater. Chem. A*, **2016**, 4, 819.
- [15] L. N. Wang, Y. Zhao, M. L. Thomas and H. R. Byon, *Adv. Funct. Mater.*, **2014**, 24, 2248.
- [16] F. X. Wu, A. Magasinski and G. Yushin, *J. Mater. Chem. A*, **2014**, 2, 6064.
- [17] L. Chen, Y. Z. Liu, F. Zhang, C. H. Liu and L. L. Shaw, *ACS Appl. Mater. Interfaces*, **2015**, 7, 25748.
- [18] Y. J. Choi, Y. D. Chung, C. Y. Baek, K. W. Kim, H. J. Ahn and J. H. Ahn, *J. Power Sources*, **2008**, 184, 548.
- [19] B. He, W. C. Li, C. Yang, S. Q. Wang and A. H. Lu, *ACS Nano*, **2016**, 10, 1633.
- [20] K. Yang, Q. M. Gao, Y. L. Tan, W. Q. Tian, W. W. Qian, L. H. Zhu and C. X. Yang, *Chem.-Eur. J.*, **2016**, 22, 3239.
- [21] Z. Geng, Q. F. Xiao, D. B. Wang, G. H. Yi, Z. G. Xu, B. Li and C.

- M. Zhang, *Electrochim. Acta*, **2016**, 202, 131.
- [22] D. X. Wang, A. P. Fu, H. L. Li, Y. Q. Wang, P. Z. Guo, J. Q. Liu and X. S. Zhao, *J. Power Sources*, **2015**, 285, 469.
- [23] X. Li, Q. Sun, J. Liu, B. W. Xiao, R. Y. Li and X. L. Sun, *J. Power Sources*, **2016**, 302, 174.
- [24] G. Li, J. H. Sun, W. P. Hou, S. D. Jiang, Y. Huang and J. X. Geng, *Nat. Commun.*, **2016**, 7.
- [25] R. Sahore, L. P. Estevez, A. Ramanujapuram, F. J. DiSalvo and E. P. Giannelis, *J. Power Sources*, **2015**, 297, 188.
- [26] X. Y. Tao, X. R. Chen, Y. Xia, H. Huang, Y. P. Gan, R. Wu, F. Chen and W. K. Zhang, *J. Mater. Chem. A*, **2013**, 1, 3295.
- [27] N. Moreno, A. Caballero, L. Hernan, J. Morales and J. Canales-Vazquez, *Phys. Chem. Chem. Phys.*, **2014**, 16, 17332.
- [28] M. S. Kim, J. Jeong, W. I. Cho and W. Kim, *Nanotechnology*, **2016**, 27.
- [29] H. Q. Wang, C. F. Zhang, Z. X. Chen, H. K. Liu and Z. P. Guo, *Carbon*, **2015**, 81, 782.
- [30] S. R. Chen, Y. P. Zhai, G. L. Xu, Y. X. Jiang, D. Y. Zhao, J. T. Li, L. Huang and S. G. Sun, *Electrochim. Acta*, **2011**, 56, 9549.
- [31] X. L. Ji, K. T. Lee and L. F. Nazar, *Nat. Mater.*, **2009**, 8, 500.

- [32] A. Ghosh, S. Shukla, G. S. Khosla, B. Lochab and S. Mitra, *Sci. Rep.*, **2016**, 6.
- [33] S. Baek, S. H. Yu, S. K. Park, A. Pucci, C. Marichy, D. C. Lee, Y. E. Sung, Y. Piao and N. Pinna, *RSC Adv.*, **2011**, 1, 1687.
- [34] S. K. Park, S. H. Yu, N. Pinna, S. Woo, B. Jang, Y. H. Chung, Y. H. Cho, Y. E. Sung and Y. Piao, *J. Mater. Chem.*, **2012**, 22, 2520.
- [35] M. F. Huang, X. P. Jiang, H. Zhang, H. S. Yin, X. X. Li and X. Ju, *J. Power Sources*, **2014**, 272, 1.
- [36] J. Q. Shan, Y. X. Liu, Y. Z. Su, P. Liu, X. D. Zhuang, D. Q. Wu, F. Zhang and X. L. Feng, *J. Mater. Chem. A*, **2016**, 4, 314.
- [37] Y. Y. Li, Z. S. Li, Q. W. Zhang and P. K. Shen, *J. Mater. Chem. A*, **2014**, 2, 4528.
- [38] X. L. Yu, J. F. Zhao, R. T. Lv, Q. H. Liang, C. Z. Zhan, Y. Bai, Z. H. Huang, W. C. Shen and F. Y. Kang, *J. Mater. Chem. A*, **2015**, 3, 18400.
- [39] Y. W. Zhu, S. Murali, M. D. Stoller, K. J. Ganesh, W. W. Cai, P. J. Ferreira, A. Pirkle, R. M. Wallace, K. A. Cychosz, M. Thommes, D. Su, E. A. Stach and R. S. Ruoff, *Science*, **2011**, 332, 1537.
- [40] J. Schuster, G. He, B. Mandlmeier, T. Yim, K. T. Lee, T. Bein and L. F. Nazar, *Angew. Chem. Int. Ed.*, **2012**, 51, 3591.

- [41] Z. Li, J. T. Zhang and X. W. Lou, *Angew. Chem. Int. Ed.*, **2015**, 54, 12886.
- [42] J. X. Song, M. L. Gordin, T. Xu, S. R. Chen, Z. X. Yu, H. Sohn, J. Lu, Y. Ren, Y. H. Duan and D. H. Wang, *Angew. Chem. Int. Ed.*, **2015**, 54, 4325.
- [43] B. Jang, M. Park, O. B. Chae, S. Park, Y. Kim, S. M. Oh, Y. Piao and T. Hyeon, *J. Am. Chem. Soc.*, **2012**, 134, 15010.
- [44] S. K. Liu, K. Xie, Z. X. Chen, Y. J. Li, X. B. Hong, J. Xu, L. J. Zhou, J. F. Yuan and C. M. Zheng, *J. Mater. Chem. A*, **2015**, 3, 11395.
- [45] K. Tang, R. J. White, X. K. Mu, M. M. Titirici, P. A. van Aken and J. Maier, *Chemsuschem*, **2012**, 5, 400.
- [46] W. D. Zhou, H. Chen, Y. C. Yu, D. L. Wang, Z. M. Cui, F. J. DiSalvo and H. D. Abruna, *ACS Nano*, **2013**, 7, 8801.
- [47] S. K. Park, S. Woo, S. Lee, C. Y. Seong and Y. Piao, *RSC Adv.*, **2015**, 5, 52687.
- [48] Z. J. Fan, J. Yan, T. Wei, G. Q. Ning, L. J. Zhi, J. C. Liu, D. X. Cao, G. L. Wang and F. Wei, *ACS Nano*, **2011**, 5, 2787.
- [49] F. B. Su, X. S. Zhao, Y. Wang, J. H. Zeng, Z. C. Zhou and J. Y. Lee, *J Phys Chem B*, **2005**, 109, 20200.

[50] S. S. Zhang, *J. Electrochem. Soc.*, **2012**, 159, A920.

[51] J. Lee and W. Choi, *J. Electrochem. Soc.*, **2015**, 162, A935.

## Chapter 5. Conclusion

The aim of this dissertation was to develop various kinds of synthetic methods for hybrid nanostructures based on 2D carbon nanomaterials which are used in rechargeable batteries. Due to their remarkable electronic, mechanical, and electrochemical properties, the carbon-based 2D nanomaterials were selected as electrodes. Further, these nanostructures have been considered promising building blocks for construction of advanced electrodes with high energy density and stability.

In my dissertation, I aim to describe 2D carbon-based nanocomposites, particularly centering on their preparation strategies and applications in rechargeable batteries (*i. e.* Li and Na ion batteries and lithium-sulfur batteries). Firstly, solventless and scalable strategy is developed for the synthesis of few-layer MoS<sub>2</sub> incorporated into hierarchical porous carbon (MHPC) nanosheet composites as anode materials for both Li- and Na-ion battery. An inexpensive oleylamine is introduced to not only serve as a surfactant and hinder the stacking of MoS<sub>2</sub> nanosheets but also to provide a conductive carbon, allowing large scale production. In addition, a SiO<sub>2</sub> template is adopted to direct the growth of both carbon

and MoS<sub>2</sub> nanosheets, resulting in the formation of hierarchical porous structures with interconnected networks. Due to these unique features, the as-obtained MHPC shows substantial reversible capacity and very long cycling performance when used as an anode material for LIBs and SIBs, even at high current density. Indeed, this material delivers reversible capacities of 732 and 280 mA h g<sup>-1</sup> after 300 cycles at 1 A g<sup>-1</sup> in LIBs and SIBs, respectively. In addition, its Coulombic efficiency reached ~98 % after the 3<sup>rd</sup> cycle and exceeded 99 % after 100 cycles, indicating that efficient Li<sup>+</sup> insertion and extraction occur in the MHPC composites. The results suggest that these MHPC composites also have tremendous potential for applications in other fields.

Secondly, monodisperse carbon nanocapsule ensemble-on-graphene nanosheet composites (MCNC/G) were prepared by a facile strategy, which involves mixing of iron-oleate and graphene, heat treatment, and finally, acid etching of iron oxide nanoparticles. The composites comprised highly uniform, hollow structured carbon nanocapsules with a diameter of about 20 nm that were densely deposited on the surface of the graphene nanosheets (the specific surface area = 172.4 m<sup>2</sup> g<sup>-1</sup> and pore volume = 0.96 cm<sup>3</sup> g<sup>-1</sup>). In lithium-sulfur (Li-S) battery test, the MCNC/G-sulfur (MCNC/G-S) composite delivered a high specific

capacity of 524.7 mA h g<sup>-1</sup> after 100 cycles at 0.5 C-rate. In contrast, the capacity of graphene-sulfur (G-S) dropped significantly under the same conditions, even though the initial specific capacity (1337 mA h g<sup>-1</sup>) was higher than that of MCNC/G-S (1262 mA h g<sup>-1</sup>).

Finally, we report the successful synthesis of honeycomb-like 2D mesoporous carbon nanosheet (OMCNS) by an etching of self-assembled iron oxide/carbon hybrid nanosheets as an advanced sulfur host for Li-S batteries. The obtained 2D nanosheets have close-packed uniform cubic mesopores of ~ 20 nm side length, resembling honeycomb structure (the specific surface area = 386.7 m<sup>2</sup> g<sup>-1</sup> and pore volume = 1.05 cm<sup>3</sup> g<sup>-1</sup>). We loaded OMCNS with sulfur element simple melting infusion process (70 wt%) and evaluate the performance of the resulting OMCNS-sulfur composites as cathode material. the OMCNS-S electrode exhibits a reasonable cycling performance compared with G-S electrode, and it could maintain the specific capacity of 1237.7 mA h g<sup>-1</sup> at 1<sup>st</sup> cycle (0.1 C). After the galvanostatic rates were changed to 0.5 C, a specific capacity of 694.1 mA h g<sup>-1</sup> is obtained with the capacity retention of 548.6 mA h g<sup>-1</sup> at 0.5 C after 300 cycles. On the contrary, the G-S composite shows the fast capacity fading owing compared to OMCNS-S composite.

Such these 2D carbon-based nanocomposites enables the achievement of electrode materials with high capacity and long cyclability for high-performance rechargeable batteries. The results suggest that these nanocomposites also have tremendous potential for applications in other fields.

# Bibliography

## 1. International Publications

1) Seunghwan Baek, Seung-Ho Yu, **Seung-Keun Park**, Andrea Pucci, Catherine Marichy, Dong-Chan Lee, Yung-Eun Sung, Yuanzhe Piao and Nicola Pinna\*, “A one-pot microwave-assisted non-aqueous sol–gel approach to metal oxide/graphene nanocomposites for Li-ion batteries”, *RSC Advances*. **2011**, 1, 1687-1690.

2) **Seung-Keun Park**,<sup>+</sup> Seung-Ho Yu,<sup>+</sup> Nicola Pinna, Seunghee Woo, Byungchul Jang, Young-Hoon Chung, Yong-Hun Cho, Yung-Eun Sung,<sup>\*</sup> and Yuanzhe Piao\*, “A facile hydrazine-assisted hydrothermal method for the deposition of monodisperse SnO<sub>2</sub> nanoparticles onto graphene for lithium ion batteries”, *Journal of Materials Chemistry*, **2012**, 22, 2520-2525. (<sup>+</sup>**Co-first author**)

3) **Seung-Keun Park**,<sup>+</sup> Seung-Ho Yu,<sup>+</sup> Seunghee Woo, Jeonghyun Ha, Junyoung Shin, Yung-Eun Sung<sup>\*</sup> and Yuanzhe Piao\*, “A facile and green strategy for the synthesis of MoS<sub>2</sub> nanospheres with excellent

Li-ion storage properties”, *CrystEngComm*, **2012**, 14, 8323-8325.

(**+Co-first author**)

4) Seunghee Woo, Jaeyoung Lee, **Seung-Keun Park**, Hasuck Kim, Taek Dong Chung\*, Yuanzhe Piao\*, Enhanced electrocatalysis of PtRu onto graphene separated by Vulcan carbon spacer, *Journal of Power Sources*, **2013**, 222, 261-266.

5) **Seung-Keun Park**,<sup>+</sup> Seung-Ho Yu,<sup>+</sup> Seung-Hee Woo, Bo Quan, Dong-Chan Lee, Min Kun Kim, Yung-Eun Sung\* and Yuanzhe Piao\*, “A simple L-cysteine-assisted method for the growth of MoS<sub>2</sub> nanosheets on carbon nanotubes for high-performance lithium ion batteries”, *Dalton Transactions*, **2013**, 42, 2399-2405. (**+Co-first author**)

6) Seung-Ho Yu, Donato E. Conte, Seunghwan Baek, Dong-Chan Lee, **Seung-Keun Park**, Kyung Jae Lee, Yuanzhe Piao, Yung-Eun Sung\*, and Nicola Pinna\*, “Structure-properties relationship in iron oxide-reduced graphene oxide nanostructures for Li-ion batteries”, *Advanced Functional Materials*, **2013**, 23, 4293-4305.

- 7) Jeonghyun Ha, **Seung-Keun Park**, Seung-Ho Yu, Aihua Jin, Byungchul Jang, Sungyool Bong, In Kim, Yung-Eun Sung\* and Yuanzhe Piao\*, “A chemically activated graphene-encapsulated LiFePO<sub>4</sub> composite for high-performance lithium ion batteries”, *Nanoscale*, **2013**, 5, 8647-8655.
- 8) Byungchul Jang, Oh B. Chae, **Seung-Keun Park**, Jeonghyun Ha, Seung Mo.Oh, Hyon Bin Na,\* and Yuanzhe Piao\*, “Solventless synthesis of iron-oxide/graphene nanocomposite and their application as anode in high-rate Li-ion batteries”, *Journal of Materials Chemistry A*, **2013**, 1, 15442-15446.
- 9) Dong Young Chung, **Seung-Keun Park**, Young-Hoon Chung, Seung-Ho Yu, Dong-Hee Lim, Namgee Jung, Hyung Chul Ham, Hee-Young Park, Yuanzhe Piao, Sung Jong Yoo\* and Yung-Eun Sung\*, “Edge-exposed MoS<sub>2</sub> nano-assembled structures as efficient electrocatalysts for hydrogen evolution reaction”, *Nanoscale*, **2014**, 6, 2131-2136.

- 10) **Seung-Keun Park**, Aihua Jin, Seung-Ho Yu, Jeonghyun Ha, Byungchul Jang, Sungyool Bong, Seunghee Woo, Yung-Eun Sung\* and Yuanzhe Piao\*, “In situ hydrothermal synthesis of Mn<sub>3</sub>O<sub>4</sub> nanoparticles on nitrogen-doped graphene as high-performance anode materials for lithium ion batteries”, *Electrochimica Acta*, **2014**, 120, 452-459.
- 11) Byungchul Jang, Sungyool Bong, Seunghee Woo, **Seung-Keun Park**, Jeonghyun Ha, Eunjin Choi, and Yuanzhe Piao\*, Facile synthesis of one-dimensional iron-oxide/carbon hybrid nanostructures as electrocatalysts for oxygen reduction reaction in alkaline media, *Journal of Nanoscience and Nanotechnology*, **2014**, 14, 8852-8857.
- 12) Seunghee Woo, Jaeyoung Lee, **Seung-Keun Park**, Hasuck Kim, Taek Dong Chung\* and Yuanzhe Piao\*, “Electrochemical codeposition of Pt/graphene catalyst for improved methanol oxidation”, *Current Applied Physics*, **2015**, 15, 219-225.

- 13) Wang Zhang, Bo Quan, Chaedong Lee, **Seung-Keun Park**, Xinghe Li, Eunjin Choi, Guowang Diao\* and Yuanzhe Piao\*, “One-step facile solvothermal synthesis of copper ferrite-graphene composite as a high-performance supercapacitor material”, *ACS Applied Materials & Interfaces*, **2015**, 7, 2404-2414.
- 14) **Seung-Keun Park**, Seunghee Woo, Sohee Lee, Chae-Yong Seong and Yuanzhe Piao\*, “Design and tailoring of three-dimensional graphene–vulcan carbon–Bi<sub>2</sub>S<sub>3</sub> ternary nanostructures for high performance lithium-ion-battery anodes”, *RSC Advances*, **2015**, 5, 52687-52694.
- 15) Sohee Lee, Sungyool Bong, Jeonghyun Ha, Minjeong Kwak, **Seung-Keun Park** and Yuanzhe Piao\*, Electrochemical deposition of bismuth on activated graphene-nafion composite for anodic stripping voltammetric determination of trace heavy metals, *Sensors and Actuators B: Chemical*, **2015**, 215, 62-69.
- 16) **Seung-Keun Park**, Chae-Yong Seong and Yuanzhe Piao\*, A simple dip-coating approach for preparation of three-dimensional

multilayered graphene-metal oxides hybrid nanostructures as high performance lithium-ion battery electrodes, *Electrochimica Acta*, **2015**, 176, 1182–1190.

17) **Seung-Keun Park**,<sup>+</sup> Chae-Yong Seong,<sup>+</sup> Suyeon Yoo and Yuanzhe Piao\* Porous Mn<sub>3</sub>O<sub>4</sub> nanorod/reduced graphene oxide hybrid paper as a flexible and binder-free anode material for lithium ion battery, *Energy*, **2016**, 99, 266-273. (+Co-first author)

18) Sohee Lee, **Seung-Keun Park**, Eunjin Choi and Yuanzhe Piao\*, Voltammetric determination of trace heavy metals using an electrochemically deposited graphene/bismuth nanocomposite film-modified glassy carbon electrode, *Journal of Electroanalytical Chemistry*, **2016**, 766, 120-127.

19) **Seung-Keun Park**, Jeongyeon Lee, Sungyool Bong, Byungchul Jang, Kwang-dong Seong and Yuanzhe Piao\*, A Scalable Synthesis of Few-layer MoS<sub>2</sub> Incorporated into Hierarchical Porous Carbon Nanosheets for High-performance Lithium and Sodium Ion Battery Anodes, *ACS Applied Materials & Interfaces*, Under revision

- 20) **Seung-Keun Park**<sup>+</sup>, Dong Young Chung<sup>+</sup>, Dongjin Ko, Yung-Eun Sung\* and Yuanzhe Piao\*, Three-dimensional Carbon Foam/Graphene@MoS<sub>2</sub> Hybrid Nanostructures as Effective Electrocatalysts for Hydrogen Evolution Reaction, *Journal of Materials Chemistry A*, Under revision (**+Co-first author**)
- 21) Jeongyeon Lee<sup>+</sup>, **Seung-Keun Park**<sup>+</sup>, and Yuanzhe Piao\*, N-doped Carbon Foam/Graphene@Sulfur as Cathode for Lithium-Sulfur Batteries, (**+Co-first author**), Submitted
- 22) **Seung-Keun Park**<sup>+</sup>, Jeongyeon Lee<sup>+</sup> and Yuanzhe Piao\*, Sulfur-loaded Monodisperse Carbon Nanocapsules on Graphene Nanosheets as a Cathode for Lithium-Sulfur Batteries, (**+Co-first author**), Submitted.
- 23) **Seung-Keun Park**<sup>+</sup>, Jeongyeon Lee<sup>+</sup>, Taejin Hwang and Yuanzhe Piao\*, Honeycomb-like Ordered Mesoporous Carbon Nanosheets and Their Application in Lithium-Sulfur Batteries, (**+Co-first author**), in prepared.

- 24) **Seung-Keun Park**,<sup>+</sup> Gi Dae Park<sup>+</sup>, Dongjin Ko, Yun Chan Kang\* and Yuanzhe Piao\*, Aerosol Synthesis of Molybdenum Diselenide-Reduced Graphene Oxide Composite with Empty Nanovoids and Enhanced Hydrogen Evolution Reaction Performances, (<sup>+</sup>**Co-first author**), Submitted.

## 2. Domestic Publication

- 1) 하정현(Jeonghyun Ha), 박승근 (**Seung-Keun Park**), 박원철 (Yuanzhe Piao)\*, 다공성 그래핀의 제조방법과 에너지 저장 소자에의 응용 (Introduction to the synthesis of porous graphene-based materials and their application in energy storage devices), E. Chem Magazine, 2013, 4, 29-37 (Review paper, published by The Korean Electrochemical Society).

## 3. International Conferences

- 1) **Seung-Keun Park**, Seung-Ho Yu, Yung-Eun Sung and Yuanzhe Piao\*, “A simple hydrazine-assisted method for the growth of

- monodisperse SnO<sub>2</sub> nanoparticles on graphene for lithium ion batteries”, 2013 MRS spring Meeting, San Francisco, CA, USA (April 1–5, 2013)
- 2) **Seung-Keun Park**, Byungchul Jang and Yuanzhe Piao\*, A simple synthesis of N-doped graphene-Mn<sub>3</sub>O<sub>4</sub> nanocomposites as high-performance anode materials for lithium ion batteries, Carbon 2014, Jeju Island, Republic of Korea (June 29–July 4, 2014).
- 3) **Seung-Keun Park** and Yuanzhe Piao\*, Nitrogen-doped graphene-wrapped Mn<sub>3</sub>O<sub>4</sub> nanoparticles as high-performance anode materials for lithium ion batteries, ECS 225<sup>th</sup> meeting, Orlando, FL, USA (May 11-15, 2014)
- 4) **Seung-Keun Park** and Yuanzhe Piao\*, “L-cysteine-assisted method for the preparation of cable-shaped MoS<sub>2</sub>/carbon nanotube composites for high performance lithium ion batteries”, International Symposium on New Frontiers in Nano-Bio-Energy Convergence Science and Technology (ISNBE) 2014, Suwon, Republic of Korea (Aug 12–13, 2014), Oral presentation.

- 5) **Seung-Keun Park** and Yuanzhe Piao\*, “A facile dip-coating approach for fabrication of alternative stacked graphene-metal oxides hybrid anode electrodes for high performance lithium ion battery”, New Frontiers in Nano-Bio Convergence Technology 2015, Suwon, Republic of Korea (Dec 17–18, 2015), Oral presentation.

#### 4. Domestic Conferences

- 1) **Seung-Keun Park**, Seunghee Woo, Yuanzhe Piao,  
“One-pot hydrothermal synthesis of graphene/SnO<sub>2</sub> nanocomposites as anode materials for lithium ion batteries”  
2011 The Korean Electrochemical Society Spring Meeting, The K-Hotel, Gyeongju, Koera, April 7-8, 2011.
- 2) **Seung-Keun Park**, Seung-Ho Yu, Seunghee Woo, Yung-Eun Sung,  
Yuanzhe Piao,  
“Amino acid-assisted a simple synthesis of coaxial CNTs/MoS<sub>2</sub> nanocables with highly reversible lithium storage”,  
2011 2011 The Korean Electrochemical Society Fall Meeting, KAIST, Daejeon, Korea, October 6-7, 2011.

- 3) **Seung-Keun Park**, Seung-Ho Yu, Seunghee Woo, Bo Quan, Kyung-Mo Yang, Yung-Eun Sung, Yuanzhe Piao,  
“A facile and green strategy for synthesis of MoS<sub>2</sub> nanospheres with excellent Li-ion storage properties”,  
2012 The Korean Electrochemical Society Spring Meeting,  
Kimdaejung Convention Center, Gwangju, Koera, April 12-13, 2012.
- 4) **Seung-Keun Park**, Seunghee Woo, Yuanzhe Piao,  
“A novel biomolecule-assisted method for the preparation of coaxial MoS<sub>2</sub>/carbon nanotube composites with high performance for lithium ion batteries”,  
2013 The Korean Chemical Society Spring Meeting (111th National Meeting), KINTEX, Goyang, Koera, April 17-19, 2013.
- 5) **Seung-Keun Park**, Yuanzhe Piao,  
“A facile L-cysteine-assisted method for the synthesis of 1D structured MoS<sub>2</sub>/carbon nanotube composites for high performance lithium ion batteries”,  
2013 Spring meeting of Korean Carbon Society, SNU, Seoul, Korea,  
May 9-10, 2013.

- 6) **Seung-Keun Park**, JiSeop Oh, Yuanzhe Piao,  
“A dip-coating method for fabrication of multilayered graphene- $\text{Mn}_3\text{O}_4$  hybrid nanostructures as high rate lithium-ion battery”,  
2015 The Korean Chemical Society Fall Meeting (116th National Meeting), EXCO, Daegu, October 14-16, 2015.
- 7) **Seung-Keun Park**, Yuanzhe Piao,  
“A facile dip-coating process for preparation of 3-dimensional graphene- $\text{Fe}_3\text{O}_4$  hybrid anode electrode for high-fast lithium-ion battery”,  
2015 The Korean Electrochemical Society Fall meeting, CECO, Changwon, Korea, October 29-31, 2015.
- 8) **Seung-Keun Park**, Yuanzhe Piao,  
“Sulfur-impregnated Uniform Carbon Nanocapsule/Graphene Nanocomposites as Cathode for Lithium-Sulfur Batteries”,  
2016 The Korean Electrochemical Society Spring Meeting, Kimdaejung Convention Center, Gwangju, Koera, April 7-9, 2016.

9) **Seung-Keun Park**, Yuanzhe Piao,

“A facile Solventless Synthesis of Hierarchical Porous Molybdenum Sulfide/Carbon Hybrids as High-performance Anodes for Lithium- and Sodium-ion Battery”,

2016 The Korean Chemical Society Spring Meeting (116th National Meeting), KINTEX, Goyang, Korea, April 20-22, 2016, Oral presentation.

## 국 문 초 록

효율적인 에너지 활용 문제는 21세기에 들어서 연구자들이 풀어야할 가장 큰 숙제 중에 하나이다. 이러한 에너지 문제를 해결하기 위한 하나의 방법으로서 고성능을 가진 이차전지개발은 필수적이다. 그러나 현재 이차전지에 사용되는 전극소재는 이론 용량 및 구조적 한계로 인해 사회의 다양한 요구를 충족시키지 못한다. 따라서 이를 해결하기 위해 높은 용량과 안정성을 가진 차세대 전극소재에 대한 개발이 요구된다.

2차원 탄소기반의 나노복합체들은 우수한 기계적, 전기적, 광학적특성을 보여줌으로서 연구자들의 높은 관심을 끌고 있다. 특히 다양한 구조적 특징과 높은 이론용량값으로 인해 에너지 저장장치 전극소재로서 큰 관심을 불러 일으키고 있다. 본 학위 논문에서는 2차원형태의 탄소를 기반으로 한 나노복합재료를 제조하고 이를 이차전지에 응용하는 연구에 대해 보고하였다. 먼저는 대량합성이 가능한 계층적 기공구조를 가진 황화몰리브덴/탄소 전극물질의 합성법을 제안하였고, 실제로 합성된 물질은 리튬 및 소듐전지의 음극으로서 높은 용량특성을 보였다 (300 사이클 후, 전류밀도  $1\text{ A g}^{-1}$ 에서 리튬전지:  $732\text{ mAh g}^{-1}$ , 소듐전지:  $280$

mA h g<sup>-1</sup>). 다음으로, 2차원 그래핀 층 위에 균일한 나노크기의 탄소캡슐이 올라가 있는 복합체를 합성하여 리튬-황 전지 양극재로서 가능성을 확인하였다. 이는 기존의 그래핀 대비 높은 안정성과 용량값을 보여줌을 확인할 수 있었다 (100 사이클 후, 전류밀도 0.5 C-rate에서 524.7 mA h g<sup>-1</sup>). 마지막으로 벌집모양의 기공구조를 가진 2차원 탄소시트를 합성한 후, 리튬-황전지의 양극의 호스트물질로서 활용하였다. 이는 쉽게 대량합성이 가능할뿐만 아니라 그래핀 대비 훨씬 뛰어난 전기화학적 특성을 보였다 (300 사이클 후, 전류밀도 0.5 C-rate에서 548.6 mA h g<sup>-1</sup>).

다양한 방법으로 합성된 2차원 탄소복합체는 전기화학적 특성평가를 통해 이차전지 전극소재로서의 가능성을 보여주었으며, 이는 이러한 물질 및 합성법이 앞으로 다양한 응용분야에 적용될 수 있다는 것을 보여주었다.

**주요어:** 2차원 물질, 탄소 복합체, 그래핀, 전이금속칼코젠화합물, 이차전지

**학 번:** 2010-23944